UNIVERSITÀ DI PADOVA FACOLTÀ DI INGEGNERIA

DIPARTIMENTO DI INGEGNERIA DELL'INFORMAZIONE

SCUOLA DI DOTTORATO IN INGEGNERIA DELL'INFORMAZIONE

INDIRIZZO IN SCIENZA E TECNOLOGIA DELL'INFORMAZIONE

XXIV Ciclo

The Underwater Acoustic Channel and its Impact on Adaptive Communications Schemes and Networking Protocols

Dottoranda

BEATRICE TOMASI

Supervisore:
Chiar.mo Prof. Michele Zorzi

Direttore della Scuola:
Chiar.mo Prof. Matteo Bertocco

Anno Accademico 2011/2012

Alla mia famiglia
Armando, Laura e Luca
per sostenermi sempre con amore
e per essere parte di me ovunque io sia.

A Nicolò
per completarmi.

To my family
Armando, Laura and Luca
for supporting me with love,
and for being part of myself anywhere I am.

To Nicolò
for completing myself.

Contents

Abstract **xv**

Sommario **xvii**

List of Acronyms **xix**

1 Introduction **1**

1.1 Overall Structure of the Thesis 2

1.2 Contributions of the Thesis 3

2 Description of Acoustic and Environmental Data **5**

2.1 Chapter Overview 5

2.2 Scenario 6

2.2.1 SPACE08 6

2.2.2 SubNet09 8

2.2.3 KAM11 10

2.3 Transmitted Signals and Post-processing 12

2.3.1 SPACE08 12

2.3.2 SubNet09 14

2.3.3 KAM11 14

2.4 Analogies and Differences 15

3 Statistical Characterization of the Underwater Acoustic Channel **19**

3.1 Chapter Overview 19

3.2 Motivations and Related Work 20
3.3 Overview on Models for the Underwater Acoustic Channel 22
3.3.1 Environmental Conditions and Channel Characteristics 22
3.3.2 Models for the Underwater Acoustic Channel 24
3.3.3 Example of a Path Loss Model 25
3.3.4 Noise in Underwater Channel 26
3.3.5 Signal to Noise Ratio at the Receiver 26
3.4 Channel Characterization from Experimental Data 28
3.4.1 Estimates of Channel Impulse Responses 28
3.4.2 Time Correlation Coefficient 31
3.4.3 Power Delay Profile 33
3.5 Average Channel Quality Metrics 35
3.5.1 Instantaneous and Average Signal to Noise Ratio 35
3.5.2 Channel Energy Time Series 40
3.6 Wide Sense Stationarity Validation 40
3.6.1 Stationarity Test 42
3.6.2 The Interval of Stationarity 44
3.7 Validation of a Hybrid Sparse Diffuse Channel Model for Underwater Acoustic Channels 45
3.7.1 Brief Model Overview 45
3.7.2 Power Delay Profile Modeling 47
3.7.3 Numerical Results 49

4 Adaptive Communications Schemes and Model Validation 57
4.1 Chapter Overview 57
4.2 Motivations and Related Work 57
4.3 Analysis of SNR and packet error rate 60
4.4 Markov models 64
4.4.1 2-state Markov model (MM1) 65
4.4.2 4-state Markov model with memory of two past events (MM2) 65
4.4.3 2-state hidden Markov model 66
4.4.4 Comparison among Markov Models and Channel Traces 67

4.5 Performance of the Hybrid ARQ technique 71
4.5.1 Channel Model 71
4.5.2 Reliable SNR regions 74
4.5.3 Models for HARQ Schemes 81
4.5.4 Type II (Incremental Redundancy) HARQ 84
4.5.5 Type I HARQ 86
4.5.6 Results 87
4.5.7 Training over a complete SNR trace 87
4.5.8 Model Validation 89
4.6 Adaptive Modulation 92
4.6.1 System Model and Performance Analysis 92
4.6.2 Instantaneous CSI 96
4.6.3 Outdated CSI 96
4.6.4 Analysis and Simulation Results 98

5 Predictability of the channel quality 109
5.1 Chapter Overview 109
5.2 Motivations and Related Work 109
5.3 Predictability over Intervals a few Seconds Long 111
5.3.1 The PSD of the Channel Energy 111
5.4 Predictability over Intervals a few Minutes Long 113
5.4.1 System Model 113
5.4.2 Communications Performance: Outage Probability and Throughput . 117
5.4.3 Predictability of the communications performance 117

6 Conclusions 123
6.1 Future Directions 125

List of Publications 127

Bibliography 128

Acknowledgments 137

List of Figures

2.1 A scheme of the testbed deployment off the coast of Martha's Vineyard Island. 6

2.2 Time series of the wind speed and direction. The solid line shows wind speed while the circles show wind direction. 7

2.3 Time series of the significant wave height. The significant wave height is defined as the average wave height of the one-third largest waves. 8

2.4 SubNet09 deployment. 9

2.5 Average and standard deviation of SSP during experiments on May 30, June 5 and September 2. 10

2.6 KAM11 deployment. 11

2.7 Sound Speed Profile collected on Julian date 176 off the coast of Kauai Island. 12

2.8 Temperature in the water column on Julian date 185 to 190, during KAM11. . 13

3.1 Power spectral density of noise in the underwater channel. 27

3.2 The quantity $(A(d, f)N(f))^{-1}$ drawn for some distances. 28

3.3 Piece-wise log-linear approximation of $B(d)$ and $f_0(d)$ as a function of distance. 29

3.4 Pseudocolor plot of the amplitude of the Channel Impulse Response (CIR) measured during SPACE08, at S5, which is $1000\,\mathrm{m}$ from the transmitter. . . . 30

3.5 Pseudocolor plot of measured channel impulse response amplitudes for the link between T1 and H4, during SubNet09, on June 5th. 31

3.6 Pseudocolor plot of measured channel impulse response amplitudes at receiver R1 at $3\,\mathrm{km}$ from the transmitter, on Julian date 187, at 8 am GMT, during KAM11. 32

3.7 Channel correlation coefficient ρ as a function of the time lapse τ, during SPACE08, at Julian date 295, noon (GMT). 33

3.8 Channel correlation coefficient ρ as a function of the time lapse τ in June. The considered links are from each transmitter T1, T2, T3 to hydrophone H4. . . . 34

3.9 Channel correlation coefficient ρ as a function of the time lapse τ, during KAM11, Julian date 187, 8 am, at receiver R1. 35

3.10 Time spread estimate τ as a function of time, during the Julian date 296 at receivers S3, S4, S5 and S6, in SPACE08. 36

3.11 Time spread estimate τ as a function of time, during the Julian date 187 at receiver R1 in KAM11. 37

3.12 Time series of Signal-to-Noise Ratio (SNR) in dB for transmissions between T1 and all hydrophones during an experiment in SubNet09. Moving averages are provided as a solid black line. 38

3.13 Julian date 187, at 4 am during KAM11. 38

3.14 Julian date 188, at 00 am during KAM11. 39

3.15 Channel energy of the link between the source and receiving stations S3 and S4 ($200\ \mathrm{m}$ Southeast and Southwest). 41

3.16 Channel energy of the link between the source and receiving stations S5 and S6 ($1000\ \mathrm{m}$ Southeast and Southwest). 41

3.17 Fitting error of the sample PDP, estimated from the data, to the exponential Power Delay Profile (PDP). The smaller the error, the better the fitting of the sample PDP to the exponential model. 48

3.18 A typical sample PDP for receivers S3 and S5, with the exponential PDP estimated by linear fitting, and the PDP estimate based on the EM algorithm [1]. 52

3.19 Mean square prediction error of the observed sequence for receiver S3, G-Thres estimator. 53

3.20 Mean square prediction error of the observed sequence for receiver S5, G-Thres estimator. 54

3.21 G-Thres estimator, estimated sparse and diffuse components for receiver S3. . 55

3.22 G-Thres estimator, estimated sparse and diffuse components for receiver S5. . 56

4.1 Log-scale scatterplot of PER as a function of SNR for varying transmitter and all receivers. Linear fits of the joint scatterplot of all transmitters as compared to the joint scatterplot of T1 and T2, as well as the scatterplot of T3, are also provided. 61
4.2 Time series of SNR for transmissions from T2 during experiment A. Moving averages over 50 samples are provided as a solid black line. 62
4.3 Sound speed profile [m/s] at different depths as a function of time during experiment A. 62
4.4 Time series of SNR for transmissions from T2 during experiment B. Moving averages over 50 samples are provided as a solid black line. 63
4.5 m-step error correlation. Link T2–H1, experiment A. 67
4.6 m-step error correlation. Link T2–H2, experiment A. 68
4.7 m-step error correlation. Link T2–H4, experiment A. 68
4.8 m-step error correlation. Link T2–H1, experiment B. 69
4.9 m-step error correlation. Link T2–H2, experiment B. 69
4.10 m-step error correlation. Link T2–H4, experiment B. 70
4.11 Probability of observing k consecutive errors. Link T2–H1, experiment A. . . 71
4.12 Probability of observing k consecutive errors. Link T2–H2, experiment A. . . 72
4.13 Probability of observing k consecutive errors. Link T2–H4, experiment A. . . 73
4.14 Probability of observing k consecutive errors. Link T2–H1, experiment B. . . . 74
4.15 Probability of observing k consecutive errors. Link T2–H2, experiment B. . . . 75
4.16 Probability of observing k consecutive errors. Link T2–H4, experiment B. . . . 76
4.17 Measured time series of the SNR over the links from all transmitters to hydrophone H1. A moving average taken over 25 samples is superimposed to the SNR time series as a solid black line. 77
4.18 Time series of the SNR over the links from all transmitters to hydrophone H2 throughout experiment A. A moving average of the time series taken over 25 samples is superimposed to the SNR scatterplot as a solid black line. 78
4.19 Empirical Probability Density Function (PDF) of the SNR and Gaussian fit over the T1–H1 link. 79
4.20 Empirical PDF of the SNR and Gaussian fit over the T2–H1 link. 80

4.21 Empirical PDF of the SNR and Gaussian fit over the T3–H1 link. 81
4.22 Reliable regions for the T1–H1 link. 82
4.23 Reliable regions for the T2–H1 link. 83
4.24 Reliable regions for the T3–H1 link. 84
4.25 Throughput Θ as a function of the average SNR for links T1–H1 and T3–H1. 88
4.26 Number of retransmissions per correctly received frame, N_{fr}, as a function of the average SNR for the links T1–H1 and T3–H1. 90
4.27 Probability of discarding a data frame, P_{fd}, as a function of the average SNR for links T1–H1 and T3–H1. 91
4.28 Model validation, mildly non-stationary case: model trained over the *third quarter*, simulations run over the *fourth quarter* of the SNR time series. Throughput, Θ. 91
4.29 Model validation, mildly non-stationary case: model trained over the *third quarter*, simulations run over the *fourth quarter* of the SNR time series. Average number of retransmissions, N_{fr}. 92
4.30 Model validation, mildly non-stationary case: model trained over the *third quarter*, simulations run over the *fourth quarter* of the SNR time series. Probability of frame dropping, P_{fd}. 92
4.31 Model validation, non-stationary case: model trained over the *first half*, simulations run over the *second half* of the SNR time series. Throughput, Θ. 93
4.32 Model validation, non-stationary case: model trained over the *first half*, simulations run over the *second half* of the SNR time series. Average number of retransmissions, N_{fr}. 93
4.33 Model validation, non-stationary case: model trained over the *first half*, simulations run over the *second half* of the SNR time series. Probability of frame dropping, P_{fd}. 94
4.34 Comparison between theoretic and simulated spectral efficiency vs. SNR over link T1–H1 in the instantaneous knowledge case. 99
4.35 Comparison between theoretic and simulated spectral efficiency vs. SNR over link T1–H2 in the instantaneous knowledge case. 100

4.36 Comparison between theoretic and simulated spectral efficiency vs. SNR over link T1–H4 in the instantaneous knowledge case. 101
4.37 Bit error outage probability as a function of the average SNR for link T1–H1 , $m = 3$. 102
4.38 Bit error outage probability as a function of the average SNR for link T1–H2, $m = 5$. 103
4.39 Bit error outage probability as a function of the average SNR for link T1–H4, $m = 2$. 104
4.40 Bit error outage probability as a function of the average SNR for link T1–H1. Analysis and simulation shown for both the instantaneous and the delayed channel knowledge case. Time window from 0:00 to 1:40. Estimated $m = 3$. . 104
4.41 Bit error outage probability as a function of the average SNR for link T1–H1. Analysis and simulation shown for both the instantaneous and the delayed channel knowledge case. Time window from 3:20 to 5:00. Estimated $m = 2$. . 105
4.42 Bit error outage probability as a function of the average SNR for link T1–H1. Analysis and simulation shown for both the instantaneous and the delayed channel knowledge case. Time window from 5:00 to 6:40. Estimated $m = 3$. . 105
4.43 Throughput as a function of the average SNR for both the instantaneous and the delayed channel knowledge case. For link T1–H1, estimated $m = 3$. 106
4.44 Throughput as a function of the average SNR for both the instantaneous and the delayed channel knowledge case. For link T1–H2, estimated $m = 2$. 106
4.45 Throughput as a function of the average SNR for both the instantaneous and the delayed channel knowledge case. For link T1–H4, estimated $m = 2$. 107

5.1 Pseudocolor plot of the estimated Power Spectral Density (PSD) (linear scale) of the channel energy at system S3, from October 18 to 27. The white periods correspond to a lack of measured data. 112
5.2 Pseudocolor plot of the estimated PSD (linear scale) of the channel energy at system S4, from October 18 to 27. The white periods correspond to a lack of measured data. 113
5.3 Pseudocolor plot of the channel impulse response at S4, during Julian date 298. 114
5.4 Time series of the wind driven surface wave energy. 114

5.5 System model. The SNR, $\gamma(t-1)$, is estimated after the equalizer and is fed back to the receiver. The symbol $r(t)$ represents the vector of the received symbols at different receiver elements. 115
5.6 Correlation coefficient between two consecutive SNRs, τ minutes apart in time. 119
5.7 Outage probability as a function of τ. 120
5.8 Throughput as a function of τ. 121

List of Tables

2.1 Spatial coordinates of the deployed devices in SPACE08. 7
2.2 Spatial coordinates of the deployed devices in SPACE08. 9
2.3 Spatial coordinates of the deployed devices in KAM11. 11
2.4 Spatial coordinates of the deployed devices in KAM11. 17

3.1 Measured time spread in ms for all links in June. 34

4.1 Coefficients of PER fitting lines. 61
4.2 Comparison of average correct packet reception probabilities 103

Abstract

Underwater acoustic signals have been studied since the late XIXth century, when they were used to search for and localize objects, typically submarines. Nowadays, acoustic signals are also used to communicate, i.e., to convey information wirelessly from one point to another over distances of the order of kilometers. Such technology is very useful for scientific research in different fields, such as biology, oceanography, and meteorology, to name a few. It also plays an important role in anti-submarine warfare, coastal surveillance, and oil spill relief operations.

Nevertheless, the underwater acoustic communications performance, measured so far, is poor under certain conditions. In this thesis, we identify those conditions, quantify their effects on the communications system and networks, and we investigate which techniques can be useful to improve communications and networking performance. In order to do so, we analyze acoustic and environmental data collected at different times and locations.

Specifically, we evaluate the communications performance and the channel characteristics, measured during those different experimental trials and we quantify the dynamics of the communications performance. In order to mitigate the effects of the time-varying observed conditions, we propose adaptive techniques, which we evaluate by both analysis and simulation. This analysis is based on Markov chains so as to validate their suitability as statistical models for representing the dynamics of the channel quality. Since the proposed adaptive techniques require feedback, they give rise to longer delays, higher energy consumption and overhead. For this reason, we analyze the possibility of predicting the channel quality, so as to reduce the amount of feedback.

As a consequence of these insights, we are now able to address the future directions of the research. In particular, we can identify the problems related to the employment of adaptive techniques and networking protocols requiring signals exchanges between the source

and the destination. In this way, we want to investigate new solutions which are more suitable for the underwater scenario, i.e., not requiring too much message exchanges. The results presented in this thesis also lead to useful guidelines for future experimental trials, in order to collect data more effectively supporting the development of underwater acoustic communications and networks.

Sommario

I segnali acustici sottomarini sono stati studiati fin dalla fine del XIX secolo, quando venivano impiegati per ricercare e localizzare oggetti, tipicamente sottomarini. Oggi, i segnali acustici vengono usati anche per comunicare, ossia per trasmettere informazioni tra due punti a kilometri di distanza l'uno dall'altro senza fili. Tale tecnologia permette di condurre importanti ricerche scientifiche in svariati ambiti come biologia, oceanografia e meteorologia. Inoltre, assume un ruolo importante nella sorveglianza delle coste e nelle operazioni di bonifica in piattaforme petrolifere.

Tuttavia, le prestazioni delle comunicazioni acustiche sottomarine, misurate finora, degradano quando si verificano alcune condizioni. In questa tesi, identifichiamo tali condizioni, ne quantifichiamo gli effetti sui sistemi di comunicazione e analizziamo le tecniche che possono migliorare le prestazioni delle comunicazioni e delle reti. A questo scopo, analizziamo dati acustici e ambientali che sono stati raccolti in diversi momenti e luoghi.

Nello specifico, valutiamo le prestazioni delle comunicazioni e le caratteristiche di canale misurate durante diversi esperimenti e quantifichiamo le dinamiche delle prestazioni di comunicazione. Allo scopo di mitigare gli effetti delle condizioni tempo varianti osservate, proponiamo tecniche adattive, che valutiamo sia con l'analisi sia con simulazioni. Tale analisi si basa sulle catene di Markov, che vangono così validate come modelli statistici adatti a rappresentare le dinamiche della qualità del canale. Siccome le tecniche adattive proposte richiedono scambio di messaggi, esse danno luogo a ritardi più elevati, consumo maggiore di energia e aumentato overhead. Per questo motivo analizziamo la possibilità di predire la qualità del canale, così da ridurre la quantità di messaggi da scambiare.

Come conseguenza dei questi studi, siamo ora capaci di identificare le direzioni future della ricerca in questo ambito. In particolare, possiamo identificare i problemi legati all'impiego di tecniche adattive e di protocolli di rete che richiedono scambi di messaggi

tra la sorgente e la destinazione. In tal modo, vogliamo approfondire lo studio di soluzioni più adatte allo scenario sottomarino acustico, ossia che non richiedano molto scambio di messaggi. I risultati presentati in questa tesi, aiutano a identificare alcune linee guida per i prossimi esperimenti in mare, allo scopo di collezionare dati, in grado di sostenere lo sviluppo di tecniche di comunicazione e di protocolli di rete per lo scenario acustico sottomarino.

List of Acronyms

ACK Acknowledgment

AM Adaptive Modulation

AMC Adaptive Modulation and Coding

AWGN Additive White Gaussian Noise

ARQ Automatic Repeat reQuest

ASE Achieved Spectral Efficiency

BEO Bit Error Outage

BER Bit Error Rate

BPSK Binary Phase-Shift Keying

CDF Cumulative Distribution Function

C.F. Characteristic Function

CIR Channel Impulse Response

CRC Cyclic Redundancy Check

CSI Channel State Information

CTD Conductivity Temperature and Density

DFE Decision Feedback Equalizer

EM Expectation-Maximization

FAM Fast Adaptive Modulation

FEC Forward Error Correction

FH-BFSK Frequency-Hopping Binary Frequency-Shift Keying

FSMC Finite-State Markov Chain

FSK Frequency-Shift Keying

GS Global Spectrum

HARQ Hybrid Automatic Repeat reQuest

HFM Hyperbolic Frequency Modulated

HMM Hidden Markov Model

HSD Hybrid Sparse Diffuse

ICI Inter Channel Interference

IID Independent and Identically Distributed

IR-HARQ Incremental Redundancy Hybrid Automatic Repeat reQuest

ISI Inter Symbol Interference

KAM11 Kuaui Acomms MURI

KLD Kullback-Leibler divergence

LDPC Low Density Parity Check

LFM Linear Frequency Modulated

LS Least Squares

MAC Medium Access Control

MAP Maximum A Posteriori

MIMO Multiple-Input Multiple-Output

ML Maximum Likelihood

MMSE Minimum Mean Square Error

M**-PSK** M-ary Phase-Shift Keying

M**-QAM** M-ary Quadrature Amplitude Modulation

MSE Mean Square Error

MVCO Martha's Vineyard Coastal Observatory

NACK Not Acknowledgment

NURC NATO Undersea Research Center

PDF Probability Density Function

PDP Power Delay Profile

PER Packet Error Rate

PHY Physical

PSAM Pilot Symbols Assisted Modulation

PSD Power Spectral Density

QoS Quality of Service

QPSK Quaternary Phase-Shift Keying

RLS Recursive Least Square

RV Random Variable

SE Spectral Efficiency

SER Symbol Error Rate

SINR Signal to Interference and Noise Ratio

SISO Single-Input Single-Output

SNR Signal-to-Noise Ratio

SPACE08 Surface Processes and Acoustic Communications Experiment

SSP Sound Speed Profile

SubNet09 Submarine Networks

UWB Ultra-WideBand

WHOI Woods Hole Oceanographic Institution

WSS Wide Sense Stationarity

Chapter 1

Introduction

Underwater acoustic communications make it possible to explore and constantly monitor the ocean, wirelessly and without jeopardizing human lives. Therefore, it represents one of the most important technologies for ocean-related sciences and military applications. Nevertheless, they are characterized by harsher and more complex propagation conditions than terrestrial radio communications, so as to make the optimal solutions developed for the latter not always suitable for underwater acoustic communication systems. In recent years, the scientific and military communities have also shown interest in the potentialities of a network of underwater sensor nodes, able to communicate with each other in order to convey the required information to a final user, safe onshore. For this reason, researchers have been investigating and designing communications algorithms and networking protocols, optimized for the underwater acoustic scenario. However, it is not always clear which assumptions can be made in order to better represent the underwater acoustic scenario.

As a starting point, the characteristics of underwater acoustic propagation which mostly affect the communications performance have to be identified. Among these features, we enumerate the propagation delay, the time-variability and the frequency-selectivity. Moreover, from the network point of view, the inter-packet variability of the communications performance has to be quantified, in order to have insight on the dynamics affecting the network protocol layers.

In this thesis, we evaluate those channel characteristics and dynamics of the communications performance, by analyzing three different experimental data sets, containing both environmental and acoustic data. After having quantified the effects of the environment on the

acoustic communications performance, we propose and evaluate two adaptive techniques, namely Hybrid Automatic Repeat reQuest (HARQ) and Adaptive Modulation (AM), which effectively mitigate the time-varying communications performance, as proved by both analysis and simulation. However, such techniques are characterized by message exchanges, though very short, which increase delivery delays, energy consumption and overhead, thus reducing the benefits of the proposed adaptive communications schemes. For this reason, we study the predictability of the channel conditions, which would make it possible to reduce the amount of feedback.

For the sake of clarity, we now present the structure of the thesis, so as to guide the reader through the presented results, from experimental data analysis to model validations and communications system evaluation.

1.1 Overall Structure of the Thesis

The rest of the thesis is subdivided into four chapters, each containing a specific topic and the corresponding results, so that each chapter can almost be read separately.

In Chapter 2, we describe the environmental and acoustic data analyzed and used through the thesis. This chapter can be useful for reference in the following and provides information about how we used the data and what is available for further analysis.

In Chapter 3, we present the estimates of the channel conditions during the evaluated data sets, and in particular we highlight and quantify the time fluctuations of the communications performance. This study is important for a deeper understanding and an accurate evaluation of the dynamics of channel conditions that can be experienced in the considered scenarios. The results can also give insight on the relationship between the environment and the observed fluctuations.

In Chapter 4, we evaluate two adaptive communications schemes, which counteract the time variability of the communications performance. We also validate analytical models, which were proposed in the literature for terrestrial wireless communications, and can be used to evaluate the proposed techniques via both analysis and simulation.

In Chapter 5, we study and characterize the predictability of the communications performance of the underwater channel, and we provide insight on the prediction interval. Such

time interval is very relevant for the design and performance evaluation of networking protocols and applications.

1.2 Contributions of the Thesis

We conclude by summarizing the main results that can be found in this thesis. First, we quantify and study the impacts of the channel time variability on communications performance. Furthermore, we analyze and model the performance of two techniques, that are known to be effective on time-varying channel and performance conditions, such as HARQ and AM. Finally, since these techniques require feedback, which may reduce capacity and increase energy consumption, we investigate the possibility of reducing the amount of feedback by using predictors.

In order to more efficiently use the channel, we analyze and provide solutions to the time-varying channel conditions by facing the problem from different perspectives. In fact, we adopt both an inductive approach, when we estimate the channel statistics and the communications performance from the data, and a deductive approach, when we propose and validate models to represent the system performance. These two approaches are complementary and both useful to reach the obtained insights, which in particular consist in proving that adaptive techniques are needed and effective in underwater acoustic links. We also show that the gains provided by the employment of adaptive techniques could be further increased by using predictors.

Chapter 2

Description of Acoustic and Environmental Data

2.1 Chapter Overview

Data analysis makes it possible to extrapolate information about the main characteristics of an observed process in order to investigate and understand the causes that generate the measured effect. Nevertheless, the relationship between the amount of available data and the amount of information that can be extracted from it is not always evident. For this reason, this Chapter aims at providing sufficient details on the analyzed data sets, so that in the future it is clear what type of information can still be inferred. Moreover, this Chapter contains all the references needed to understand the results provided in the following Chapters.

In this thesis, we consider the Surface Processes and Acoustic Communications Experiment (SPACE08), Submarine Networks (SubNet09), and Kuaui Acomms MURI (KAM11) sea trials. These experiments were conducted at different times and locations, and they made it possible to collect extensive acoustic and environmental data sets. Thanks to the human and financial efforts invested in those experimental campaigns, we could test, validate and infer models, which are the main topic of Chapters 3, 4, and 5.

First, we describe the scenarios by highlighting the characteristics that make them representative of a wider number of cases, so that we can extend the results to other similar situations. Second, we present the acoustic signals that were sent and recorded, by specify-

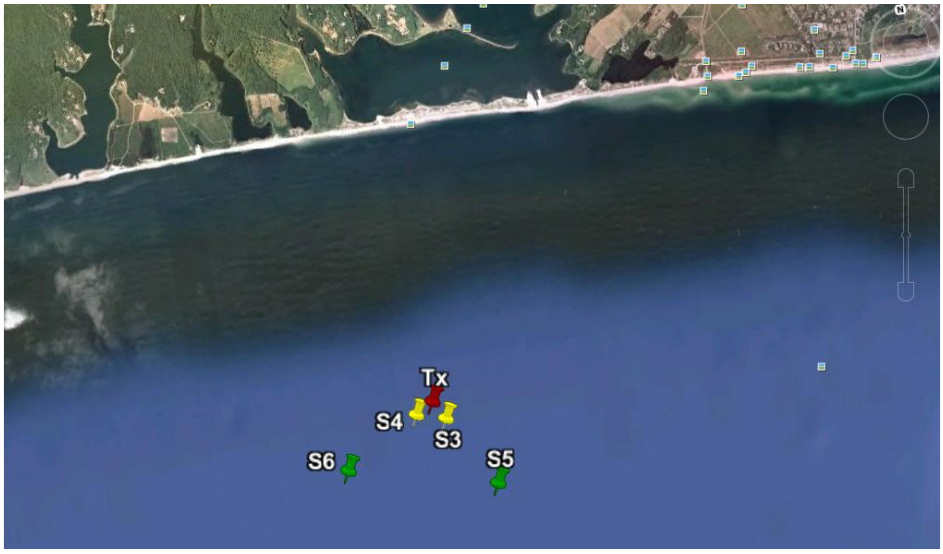

Figure 2.1. *A scheme of the testbed deployment off the coast of Martha's Vineyard Island.*

ing the employed center frequencies, bandwidths and modulation schemes. Finally, we list the differences and analogies among these data sets.

2.2 Scenario

2.2.1 SPACE08

The SPACE08 was conducted from October 18 to 27 in 2008. In the following, we refer to these days by using Julian dates from 292 to 301. The deployment was located at Martha's Vineyard Coastal Observatory (MVCO) and operated by Woods Hole Oceanographic Institution (WHOI). The scenario, considered in this thesis[1], consists of one transmitter and four fixed receiving stations, each of which is equipped with several hydrophones. Figure 2.1 shows the deployment: systems S3 and S4 are $200\,\mathrm{m}$ from the transmitter in the Southeast and Southwest directions, respectively, whereas S5 and S6 are $1000\,\mathrm{m}$ from the transmitter, again along the Southeast and Southwest directions. Table 2.1 provides the spatial coordinates of the deployment.

This configuration was specifically thought to obtain further insight on how the surface affects the acoustic propagation in a shallow water scenario. The water column was $15\,\mathrm{m}$

[1]The actual scenario consisted of three more receivers: a reference hydrophone at $1\,\mathrm{m}$ and other two receiving stations at $60\,\mathrm{m}$ from the transmitter.

Table 2.1. *Spatial coordinates of the deployed devices in SPACE08.*

Description	Label	Latitude	Longitude
Source	Tx	41 °19.492′ N	70 °34.021′ W
Vertical array, 24 hydrophones	S3	41 °19.492′ N	70 °34.021′ W
Vertical array, 24 hydrophones	S4	41 °19.437′ N	70 °34.145′ W
Vertical array, 12 hydrophones	S5	41 °19.018′ N	70 °33.663′ W
Vertical array, 12 hydrophones	S6	41 °19.207′ N	70 °34.673′ W

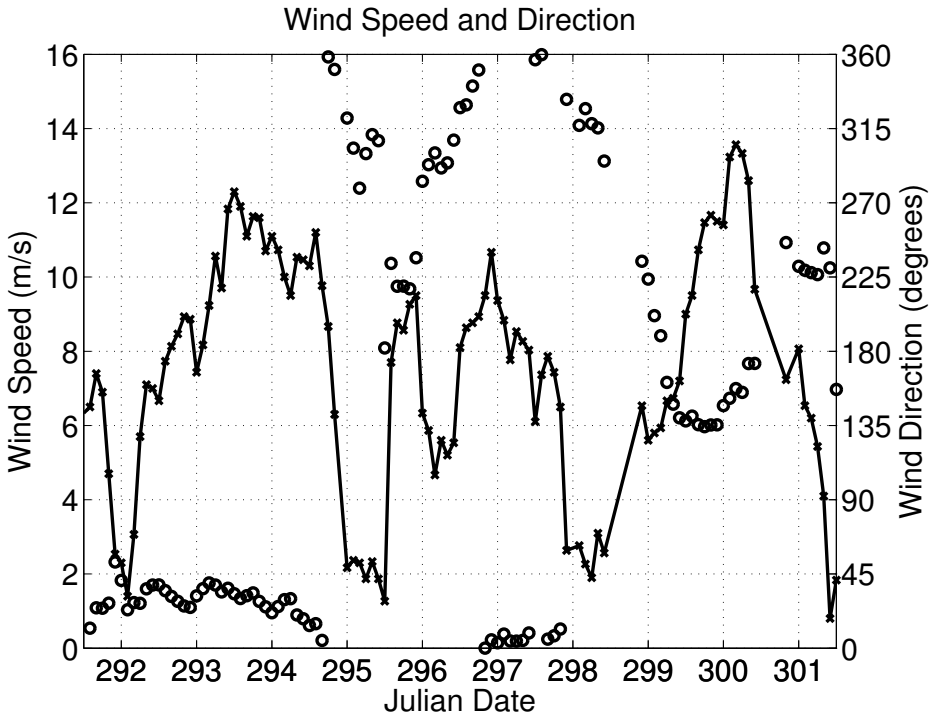

Figure 2.2. *Time series of the wind speed and direction. The solid line shows wind speed while the circles show wind direction.*

deep, the ocean floor of the area can be considered relatively flat and the temperature of the water column was constant. Therefore, the surface time-varying conditions were the most important parameter, affecting the acoustic propagation. Since the surface conditions depend on the wind, its speed and direction were measured throughout the experiment. The collected measurements are represented in Figs. 2.2 and 2.3. On Julian date 300 there was a storm and we can observe in Fig. 2.3 how the surface height increases in the correspondent day.

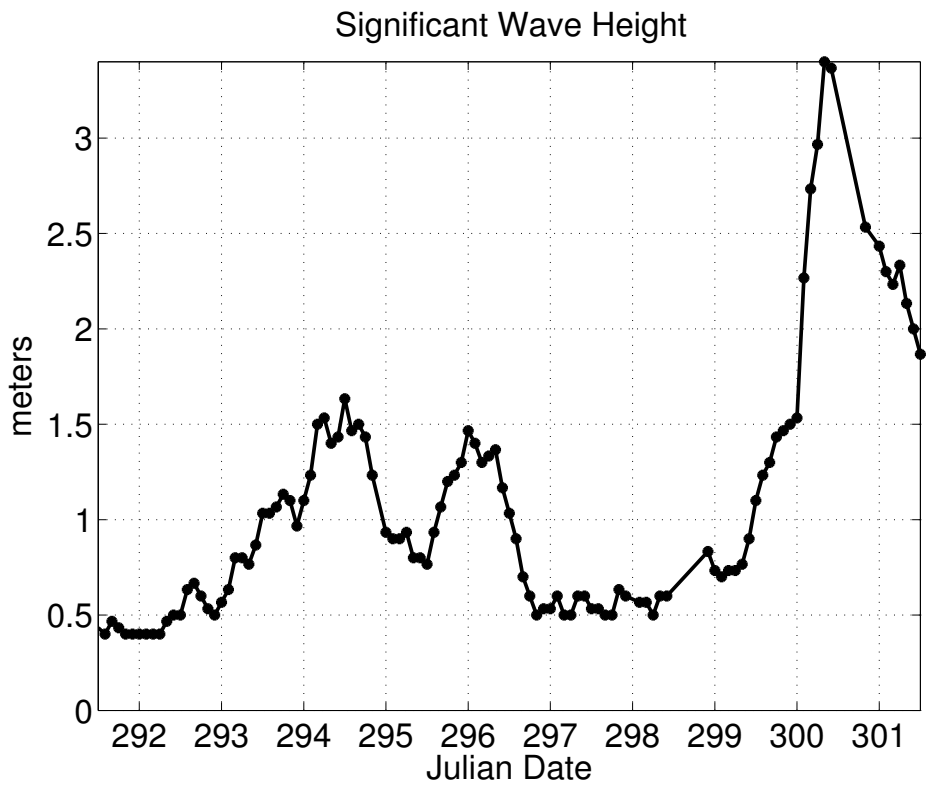

Figure 2.3. *Time series of the significant wave height. The significant wave height is defined as the average wave height of the one-third largest waves.*

2.2.2 SubNet09

The SubNet09 experimental trials were conducted during the summer of 2009, from the end of May to the beginning of September, off the eastern shore of the Pianosa Island, Italy. The experiment was operated by NATO Undersea Research Center (NURC). The testbed consists of one vertical array (VA), with four hydrophones spaced by $20\,\mathrm{m}$, and three acoustic transmitters (Teledyne-Low Frequency modems [2]) placed on a tripod on the sea floor. The deployment is shown in Fig. 2.4, where the transmitters, labeled as T1, T2 and T3, were placed at $1500\,\mathrm{m}$ from the VA, at a depth of $60\,\mathrm{m}$, $2200\,\mathrm{m}$ from the VA, at a depth of $70\,\mathrm{m}$, and $700\,\mathrm{m}$ from the VA at $80\,\mathrm{m}$ below the surface, respectively. The hydrophones of the VA were called H1, H2 and H4 and they were placed at $20\,\mathrm{m}$, $40\,\mathrm{m}$, and $80\,\mathrm{m}$, respectively. The hydrophone at $60\,\mathrm{m}$, H3, experienced malfunctioning during the first of the three months of sea trials and died right thereafter. Table 2.2 provides the spatial coordinates of the deployment.

This configuration was specifically set up to study the behavior of the acoustic channel

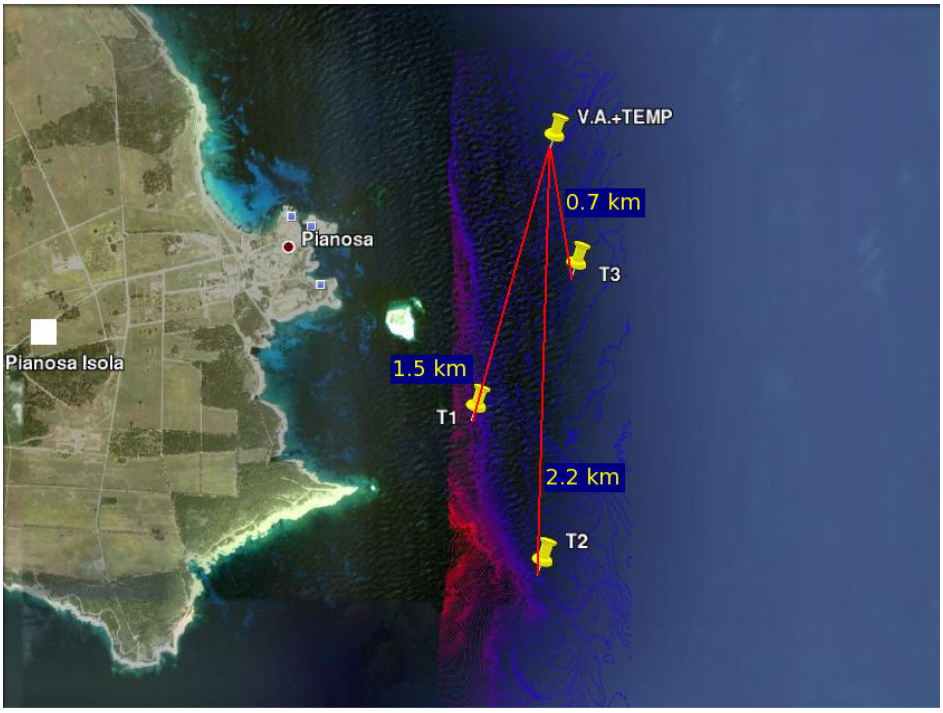

Figure 2.4. *SubNet09 deployment.*

Table 2.2. *Spatial coordinates of the deployed devices in SPACE08.*

Description	Label	Latitude	Longitude
Transmitter	T1	42 °34.4467′ N	10 °6.3887′ E
Transmitter	T2	42 °34.1850′ N	10 °6.5442′ E
Transmitter	T3	42 °35.962′ N	10 °7.255′ E
Vertical array, 4 hydrophones	VA	42 °35.3192′ N	10 °6.5735′ E

both when signals travel through the boundary between the mixed layer and the deeper layers, and when propagation takes place below the mixed layer. Oceanographic instrumentation, such as one Acoustic Doppler Current Profiler and one thermistor chain, was deployed close to the VA. The thermistor chain was designed for finer sampling in the mixed layer rather than in the lower layers, in order to better track temperature changes between 0 and $40\,\mathrm{m}$ of depth. The temperature samples gathered through the thermistors have been used to estimate the propagation speed of acoustic waves: previous studies on the physical features of the water in the Pianosa area showed that salinity is very stable over the whole summer season; therefore, frequent temperature measurements and a salinity measure taken once through a Conductivity Temperature and Density (CTD) sensor suf-

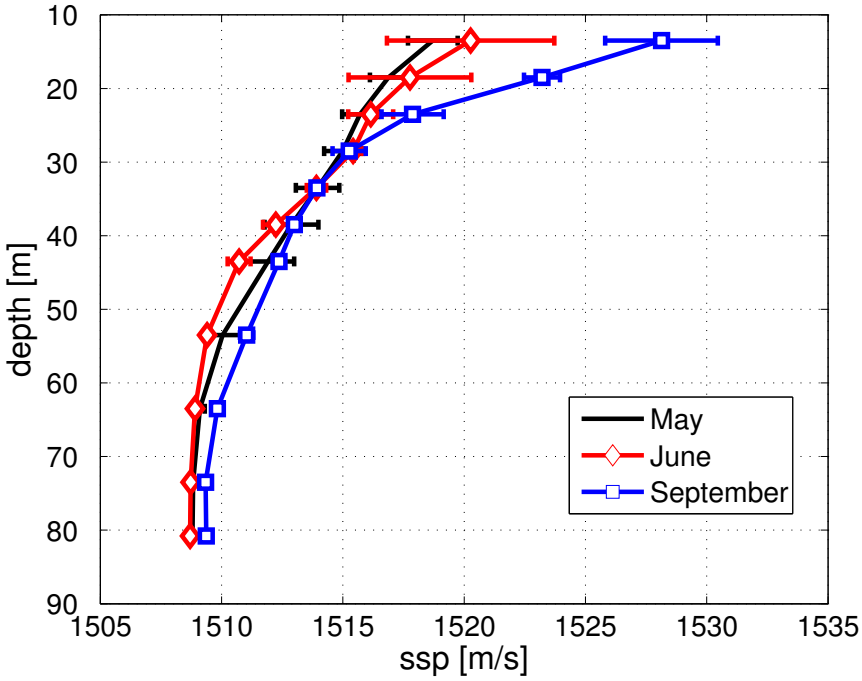

Figure 2.5. *Average and standard deviation of SSP during experiments on May 30, June 5 and September 2.*

fice to compute the Sound Speed Profile (SSP) through the Mackenzie formula, e.g., see [3]. In Fig. 2.5, we show the average value and the standard deviation of the measured sound speed at different depths in May, June and September. The figure allows us to conclude that channel conditions were quite stable over time throughout the whole season, and that the general behavior of the SSP was downward-refractive. As opposed to the stability of sound speed profiles, the roughness of the sea-surface greatly varied during the experiment period. The winds were typically calm, even though short periods with winds over $10\,\mathrm{m/s}$ were experienced. These winds generated local short-period waves that greatly affected sea surface roughness, ambient noise levels and sea surface reflections.

2.2.3 KAM11

The KAM11 data set has been collected in 2011, from June 25 to July 9, off the coast of Kauai Island, Hawaii. The analyzed scenario was stationary and consists of a source and two receivers, deployed at almost $40\,\mathrm{m}$ below the surface. The water column was $100\,\mathrm{m}$ deep. The receiving stations consisted of 24 element vertical and linear hydrophones array with

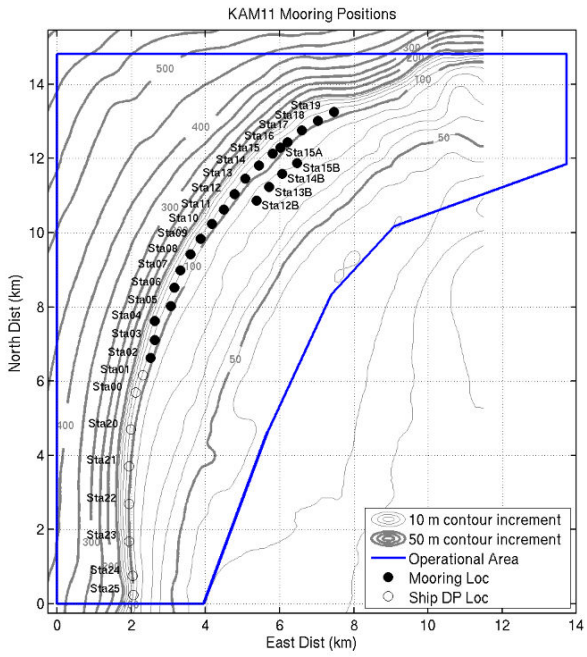

Figure 2.6. *KAM11 deployment.*

Table 2.3. *Spatial coordinates of the deployed devices in KAM11.*

Description	Label	Latitude	Longitude
Transmitter	STA03	22 °7.842′ N	−159 °48.4697′ W
Vertical array, 24 hydrophones	STA09 (R1)	22 °9.3117′ N	−159 °47.7507′ W
Vertical array, 24 hydrophones	STA17 (R2)	22 °10.3785′ N	−159 °46.8372′ W

5 cm spacing between hydrophones. Fig. 2.6 represents the whole deployment involved in the experiment, however the analyzed data concerns the links between station STA03, where the transmitter was placed, and stations STA09 and STA17, where the two receivers were located. We will call these receivers as R1 and R2. Table 2.3 provides the coordinates of the deployment.

CTD data were collected during the experiments. An example is represented in Fig. 2.7, in terms of SSP. This particular combination of up and down-refractive parts in the water column gives rise to different propagation paths, which are very sensitive even to a slight change of the SSP in time. From the data collected by a thermistor chain, it is possible to follow those time fluctuations and correlate them with the variations observed in the channel impulse responses. Thermistor chains were also deployed in the area. In particu-

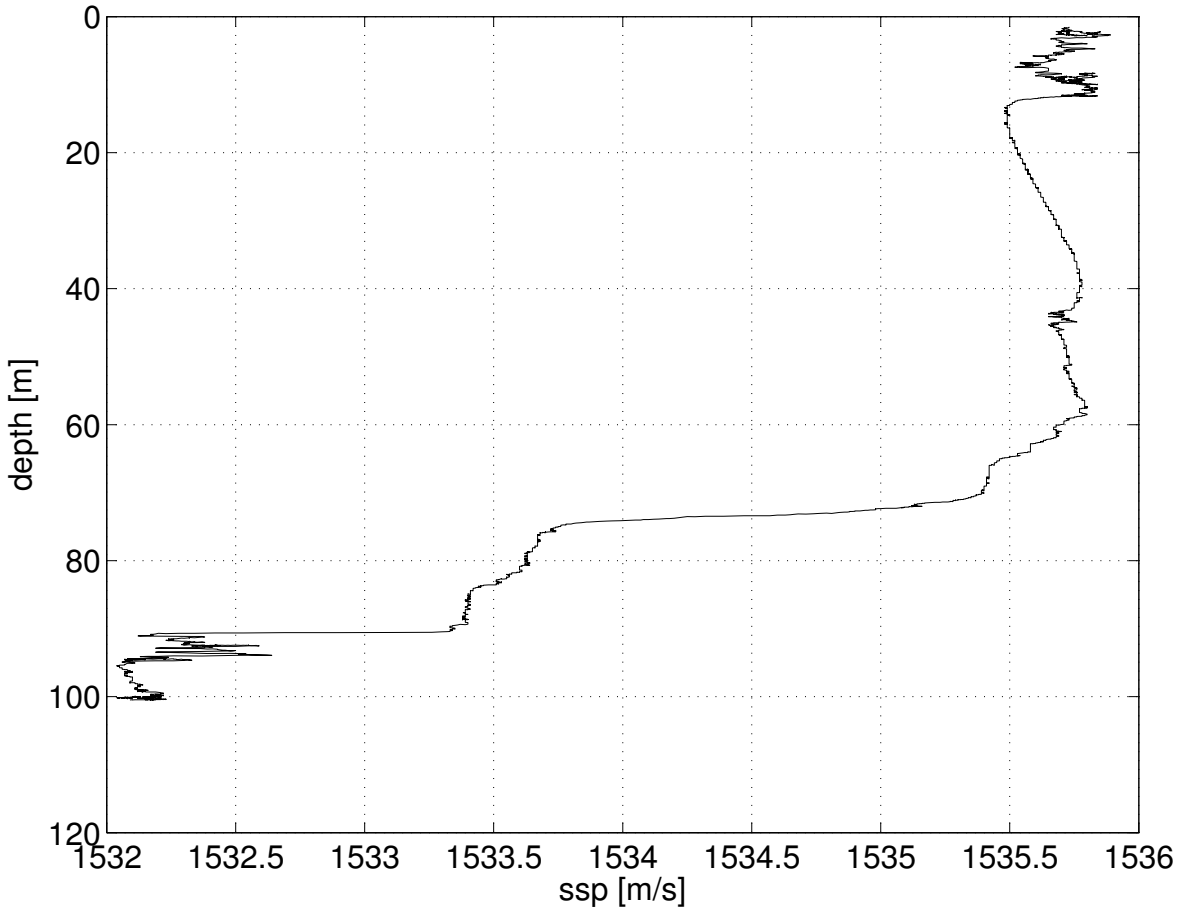

Figure 2.7. *Sound Speed Profile collected on Julian date 176 off the coast of Kauai Island.*

lar, in Fig. 2.8 we present the data from the thermistor at STA04 (Lat. $22\,°8.113'$ N, Long. $-159\,°48.4712'$ W) close to the transmitter.

2.3 Transmitted Signals and Post-processing

2.3.1 SPACE08

During SPACE08, several types of signals were transmitted. Here, we focus only on those sent in order to provide an accurate characterization of the channel and the communications performance. Among these signals, we consider Linear Frequency Modulated (LFM) pulses and binary maximum length sequences (m-sequence), which is a spectrally flat pseudo noise signal.

The carrier frequency for the LFM pulses was $13\,\mathrm{kHz}$ and the bandwidth was about

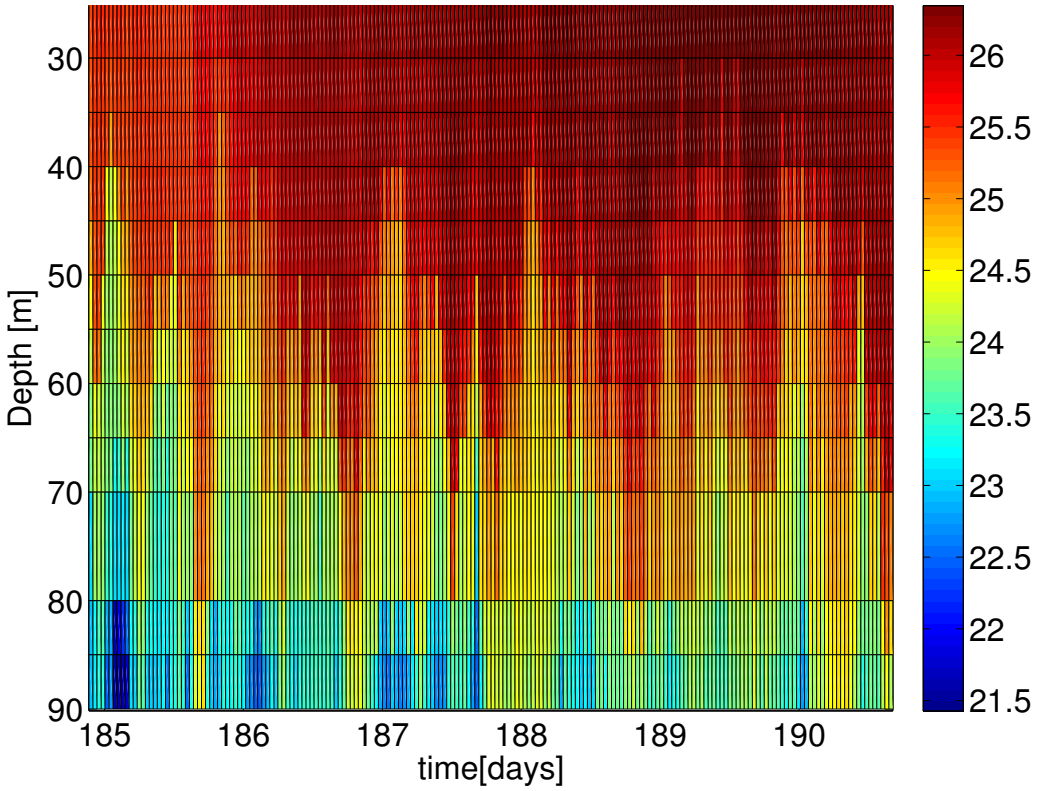

Figure 2.8. *Temperature in the water column on Julian date* 185 *to* 190*, during KAM11.*

8 kHz. These signals are suitable for providing a first estimate of the channel impulse response. Three trains, each consisting of 2042 fast pulses, were sent every two hours. Each fast pulse lasts 25 ms. We used this data to represent the amplitude of the channel impulse response as a function of time.

After the LFM pulses, m-sequences were transmitted. In particular, a file consisting of multiple repetitions of a 4095 point binary m-sequence was transmitted at a symbol rate of 6.5 kbps. These symbols were modulated according to a Binary Phase-Shift Keying (BPSK) scheme, at a carrier frequency of 13 kHz. A transmission three minutes in duration was made once every two hours, thus providing enough data to perform a statistical characterization. We first focused on the estimates of the channel impulse response by computing the correlation between the transmitted signal and the received signal, and then analyzed the communications performance in terms of SNR, Mean Square Error (MSE) of a Recursive Least Square (RLS) estimator, and eventually the Bit Error Rate (BER).

2.3.2 SubNet09

A purpose of SubNet09 was to prove the suitability of a signal format called JANUS [4] for robust underwater acoustic communications. Indeed, this signal is designed for unsolicited broadcasting of information relevant to nautical vessels, so that reliability is a requirement.

The preamble of this signal consists of three wakeup tones, a $400\,\mathrm{ms}$ silence, and either a Hyperbolic Frequency Modulated (HFM) sine wave or a sequence of 30 symbols taken from a predefined frequency-hopping pattern. The latter is employed as a probe for timing synchronization and for SNR estimation. The actual data are transmitted using a 13-subcarrier Frequency-Hopping Binary Frequency-Shift Keying (FH-BFSK) modulation with a predefined hopping pattern and a hopping rate of 1 hop per transmitted symbol. The data portion of the JANUS signal is further divided into a 144-bit header and an optional payload, which was not sent during the considered experiments.

JANUS signals are partially protected from errors by means of Physical (PHY)-layer Forward Error Correction (FEC), implemented through fixed interleaving and a convolutional channel code of generating polynomials $(753_8, 561_8)$. In addition, the frequency hopping sequence is designed to escape multipath patterns featuring long delay spread.

From the preamble of these signals, we estimated the channel impulse response, which we used in statistical characterization of the channel. Moreover, we inferred the communications performance, such as the SNR, BER and Packet Error Rate (PER), from the header of the signal.

2.3.3 KAM11

During the KAM11 experiment, signals similar to those transmitted during SPACE08 were sent, i.e., LFM pulses and m-sequences. Nevertheless, different modulations and coding schemes were also tested. In particular, we will show the results obtained by analyzing signals transmitted according to BPSK and Quaternary Phase-Shift Keying (QPSK) modulation schemes. The carrier frequency and bandwidth of the omni-directional source were $13\ \mathrm{kHz}$ and $8\ \mathrm{kHz}$, respectively.

We will focus on six sound files, which the source transmitted every two hours. Each file consists of an initial period of silence, a train of 31 packets, separated in time by $280\,\mathrm{ms}$ in

order to avoid interference between contiguous packets, and two longer packets. Overall, the file lasts one minute (including also silence), and in this study we will focus on the 31 data packets, each containing 6500 modulation symbols, transmitted at 6250 $\mathrm{symb/s}$.

We computed a first estimate of the channel impulse response, by exploiting the LFM signals, whereas we inferred the communications performance, such as the SNR, BER and PER, from the aforementioned packets.

2.4 Analogies and Differences

In this section, we highlight the aspects that make these data sets interesting and suitable for statistical analysis, and useful for designing more effective communication algorithms and networking protocols. In particular, we point out the analogies and the differences that characterize these data sets.

One of the analogies is the *fixed scenario*. In fact, from a practical point of view, this is the easiest way of deploying instruments and collecting data in the ocean or sea. Deployment operations are not always smooth, especially when the sea conditions are bad. For this reason, even though the scientific community expresses interest in mobile underwater acoustic communications, long-term experimental trials still employ stationary nodes. However, some efforts on mobile deployments are worth mentioning, such as those during both SPACE08 and SubNet09. In particular, a horizontal array of hydrophones was towed by either a ship or a vehicle, in order to capture, while moving, the signals sent by the fixed source. These signals are not considered in this thesis. Instead, we focus on the long-term recordings from stationary transducers, in order to infer statistics which give some insight on those dynamics, which communications and network algorithms have to face. In fact, even though the transmitters and receivers do not move, the environmental conditions in the experimental area are time-varying. Such conditions vary over time intervals, which are comparable to the amount of time needed for several packet exchanges, i.e., from a few seconds to a few minutes, thus becoming of interest for upper layers protocol design. Among those conditions, we showed wind speed and direction, which affect the surface and in band noise, and the temperature in the water column, which is responsible for the time fluctuations of the sound speed profile.

Another common characteristic is the *shallow water scenario*, although we can further

subdivide the scenarios into two categories: very shallow, such as in SPACE08 and shallow waters, as SubNet09 and KAM11. This is justified by the growing need for those applications, such as coastal monitoring and surveillance, which are specifically thought for shallow water. Moreover, shallow water communications are more prone to harsh channel conditions than deep water acoustic communications, thus also becoming more challenging from a technological point of view. It is worth noting that the considered scenarios are representative of a quite large variety of coastal areas. In fact, the coastal region can be either very shallow, with water depth around $15\,\mathrm{m}$, such as SPACE08, or shallow, characterized by a depth around $100\,\mathrm{m}$, such as KAM11 and SubNet09. In the thesis, we qualitatively assess which environmental conditions mostly affect the communications performance in these two categories.

The employed *frequencies and bandwidths* are similar in all these data sets. This actually makes it possible to compare the performance measured in these three different scenarios, thus providing insight on which conditions most affect the performance. Moreover, the chosen mid-frequencies region (from 7 to $17\,\mathrm{kHz}$) represents a good trade-off between capacity and the distances that have to be covered. As shown in Fig. 3.3 the employed center frequency and bandwidth are optimal over distances of the order of a few kms. Moreover, the developed technology works at similar frequencies and bandwidths such as Teledyne Benthos [2] and WHOI modems [5].

The main difference among the data sets is the *time scheduling of the transmissions and recordings*. During SPACE08, files, (each lasting almost one minute), were sent in order to measure the channel conditions and the communications performance of a specific communication system. In particular, m-sequences are suitable for the analysis of both channel conditions and communications performance in time, whereas LFM pulses are useful for estimating the channel, without much post-processing. However, the time sampling of these conditions and of the performance is given by the transmission rate of these files, i.e., every two hours. In this way, we can track the average performance over intervals three minutes long, every two hours during several days. SubNet09 presents different time sampling characteristics. In fact, even though the deployment lasted for three months, it was exploited on a few days throughout the entire summer season, in order to transmit a series of JANUS packets. As explained before, the JANUS format embeds both modulated symbols and an

Table 2.4. *Spatial coordinates of the deployed devices in KAM11.*

Description	**SPACE08**	**SubNet09**	**KAM11**
Carrier frequency	13 kHz	11.5 kHz	13 kHz
Bandwidth	8 kHz	5 kHz	8 kHz
Modulation scheme	BPSK	FH-BFSK	BPSK, QPSK
Maximum depth	15 m	80 m	100 m
Wind monitoring	yes	yes	no
Number of receivers	6	1	2
Number of transmitters	1	3	1
Surface conditions monitoring	yes	no	no
Temperature monitoring	no	yes	yes
Time sampling	3 minutes every 2 hours	1 second every 15 seconds	6 minutes every 2 hours
Duration	10 days	several hours (max 9) on different days	14 days
Season	October 2008	Summer 2009	June-July 2011

HFM pulse, or a probe sequence, which makes it possible to study both channel conditions and communications performance. However, the presence of multiple sources, rather than receivers, such as for SPACE08 and KAM11, is not suitable for spatial characterizations of simultaneous performance. This, on the other hand, is possible for both SPACE08 and KAM11. The latter is characterized by a similar scheduling as that used during SPACE08, but consists of longer observation intervals, such as six minutes instead of three minutes. For this reason, this data set is suitable for studies, that want to investigate on the relationship between environmental conditions, evolving in intervals six minutes long, and communications performance. Table 2.4 summarizes the main characteristics of the considered data sets.

Chapter 3

Statistical Characterization of the Underwater Acoustic Channel

3.1 Chapter Overview

This chapter is devoted to presenting a quantitative evaluation of the channel conditions and qualitative considerations on the relationship between acoustics and the environmental conditions, measured during the experiments previously described. In order to do so, we recall the definition of ergodic random process, which is the underlying assumption throughout the chapter. A random process is defined to be *ergodic*, if its statistics can be derived from the time series of its realizations. We assume that the CIR is an ergodic random process.

First, we estimate the CIR from experimental data sets, then we derive the time correlation coefficients and the power delay profiles. Successively, we focus on the impact of the estimated time-varying CIRs on the measured communications performance in terms of received SNR. Finally, we verify the Wide Sense Stationarity (WSS) assumption for the SNR process, and we validate a channel model, which has been proposed for Ultra-WideBand (UWB) channels in the literature.

3.2 Motivations and Related Work

The work presented here aims at quantifying the channel characteristics, that affect the performance of a communications system. The presented channel characterization provides useful insight for designing suitable solutions both at the PHY and upper layers of the communication stack. Specifically, we want to identify the aspects of the channel, that limit the performance of the most used communications systems. For this reason, we quantify the time correlation coefficient, from which the coherence time can be derived, and the power delay profile, from which the time spread of the channel can be inferred. Coherence time and time spread are the most important parameters for a receiving system, since they define how efficiently the channel can be used. Broadly speaking, both these metrics indicate the level of problems that a receiver has to compensate for, in terms of Doppler shift and spread, and distortion. Depending on the type of receiver, these phenomena give rise to loss of synchronization, Inter Symbol Interference (ISI), Inter Channel Interference (ICI).

Similar to these evaluations of the CIR and its second order statistics, we mention the results shown in [6–9], for various frequencies and using different probe signals. However, unlike most previous work, we perform here an extensive evaluation, spanning different durations and periods at different locations, thus providing a richer variety and examples of possible dynamics. Part of the presented results can be found in [10].

Tackling the problem from a different perspective, i.e., by considering the impact of the channel on the upper layers of the communication stack, we focus on the temporal behavior of the SNR. Since the SNR metric depends on the chosen receiving system, here, we deal with coherent and non-coherent receivers, since all receivers fall into any of these two categories. A coherent receiver is sensitive to the phase changes of the transmitted signal, whereas the non-coherent receiver is only affected by the amount of energy received in a symbol time. Moreover, we will present both instantaneous and average SNR estimates, even though we will focus more on the average communications performance, typically referred as packet SNR, which have a more relevant impact on the network protocols performance.

This channel characterization is quite different from those, that can be found in [9,11,12], where the authors showed how accurate the fitting between the statistics of a known Random Variable (RV) and the estimates from experimental data can be. In fact, here, we aim

more at quantifying the quality of the communications systems proposed for underwater acoustic communications, rather than finding a universal statistical model for the underwater channel.

In this chapter, we also deal with the assumption of wide-sense stationarity and in particular we evaluate the time interval over which the evolution of the chosen metric, representing the channel, can be modeled as a WSS random process. A WSS process is characterized by time invariant first and second order statistics. Such condition is required whenever an estimate is performed. This study has a twofold purpose: first, we validate the WSS property in order to estimate the second order channel statistics; second, since we envision the employment of a data adaptive estimator, which is able to predict the quality of the channel, we need to prove wide-sense stationarity, given that these estimators are optimized under the assumption that the channel fluctuations can be represented as a WSS random process. This perspective will be further developed in Chapter5.

In the literature, many stationarity tests, especially focusing on the RF wireless channel, such those in [13–15], have been performed. However the stationarity properties of the underwater acoustic channel have not been studied yet. The results presented here, have been published in [16].

Eventually, we propose a channel model, useful for both simulation and implementation in coherent equalizers, which make use of channel estimates. In fact, as shown in the following sections, the channel exhibit high attenuation, large channel delay spread, Doppler spread and, consequently, incur low throughput and reliability. In particular, the large delay spread causes inter-symbol interference (ISI), which can be compensated by equalization of the received sequence. However, the performance of coherent equalizers is highly sensitive to the availability of accurate channel estimates. To this end, it is crucial to develop channel estimation strategies that exploit the intrinsic nature of underwater acoustic propagation to improve the estimation accuracy. In a shallow water environment, not only the channel is characterized by a sparse structure but also by phenomena such as diffuse scattering, diffraction effects and frequency dispersion, which are better represented by a dense channel. We therefore validate a novel Hybrid Sparse Diffuse (HSD) model, first proposed in [17] for UWB channels, which describes the channel as the superposition of two independent components: the sparse component, which models the resolvable multipath signals,

owing to the fine delay resolution, and the diffuse component, which models other propagation phenomena, such as dense scattering and frequency dispersion.

In the literature, several underwater acoustic channel estimators based on sparse approximations and compressed sensing have been proposed and successfully employed, such as those in [18], [19], and [20]. In [21], a comparative study among purely sparse and Least Squares (LS) channel estimators has been performed, showing that the former, while improving the estimation accuracy when the channel is truly sparse, are robust even when the channel does not exhibit a sparse nature. However, in many scenarios of interest, e.g., shallow water environments, also a dense channel has been observed. For these scenarios, a purely sparse model does not appropriately represent the channel behavior, which is instead suitably described by the proposed model. These results have been published in [22].

3.3 Overview on Models for the Underwater Acoustic Channel

3.3.1 Environmental Conditions and Channel Characteristics

We briefly mention the main environmental conditions, that have an impact on the communications performance, especially in the analyzed data sets. As pointed out before, we exclusively focus on shallow water scenarios, in which acoustic waves travelling from the source to the destination reach the bottom and/or the surface at least once [23]. In these scenarios the acoustic waves interact more with the boundaries, both the surface and the bottom, thus giving rise to more severe channel conditions, since the received signals are more attenuated and scattered. In particular, the coefficient of absorption of the bottom depends on the bathymetry and on the type of material on the sea floor, which can be sandy, rocky or muddy, whereas the coefficient of reflection of the surface depends on the roughness of the surface. If waves break on the surface, air bubbles are trapped in the upper layers of the water column, giving rise to further absorption and scattering phenomena.

Another environmental parameter, that plays a key role in the acoustic propagation, is the sound velocity over the water column, also called SSP. This measure is defined over the vertical space, since the ocean is a vertically stratified medium, i.e., the water conditions vary more heavily in the vertical than in the horizontal space. The SSP is a function of both time and space, and it determines the propagation paths of the acoustic waves. Finally, the

environmental conditions mostly affecting the acoustic propagation, and therefore the communications performance, in a shallow water scenario are: i) the sound speed profile; ii) the bathymetry; iii) the type of bottom; iv) the surface roughness, which depends on the wind, and v) inhomogeneities in the water. It is worth noting that among these environmental conditions the SSP, the surface roughness and the inhomogeneities are time-varying conditions (though on different time scales).

The characterization of the channel is a key step in the development, design and study of the performance of communication schemes and networking protocols. Here we will discuss and analyze the main characteristics of the channel, which are more important to properly design communication algorithms and networking protocols. In this section, we want to describe the features of the channel, that can be found in the literature, especially in studies on the physical layer, such as [18–20, 24, 25].

The channel considered here belongs to the class of ultra-wideband (UWB) channels, since the center frequency has the same order of magnitude as the bandwidth of the system. Moreover, since the sound speed can be approximated as $1500\,\mathrm{m/s}$, i.e., five times faster than in the air, but two hundred thousands times slower than electromagnetic waves in the air, the first and last arrivals of the channel reach the receiver separated in time by more than a symbol period, which means that the channel is frequency-selective. The lack of a channel model for the UWB case, also in the terrestrial wireless case, limits the development and improvement of these communication systems. In [18–20] the underwater acoustic channel is represented as simply sparse, i.e., the arrivals can be distinguished from each other and there is no energy between two successive arrivals. Frequency-selectivity is one of the main features of the underwater acoustic channel together with the time-variability.

As underscored in Section 3.3.1, the propagation depends on the environment which changes in time, thus producing a time-varying channel even though the transmitter and the receiver are static. Time-variability and frequency-selectivity limit the communications performance and require the employment of techniques able to compensate for them, such as equalizers and orthogonal frequency division modulation (OFDM) schemes.

Another peculiarity of the underwater channel is the relationship between the capacity and the distance, established in [26], by using deterministic functions, representing noise and attenuation. This relationship states that the longer the link, the smaller the available

bandwidth. This result is very important when deploying nodes, which then can transmit up to a certain distance, given the communication bandwidth and center frequency.

Therefore, the main characteristics of the communication channel are:

- frequency selectivity
- time-variability
- capacity dependent on the distance.

In this thesis, we quantitatively evaluate the time variability and frequency selectivity of the channel, measured during three experimental trials, and we study their effect on the communication performance.

3.3.2 Models for the Underwater Acoustic Channel

In this section, we discuss the models for the underwater acoustic channel, presented in the literature so far. In particular, we present here only one model, which gives insight on the aforementioned relationship between capacity and distance, since this is one of the most used models to analyze network protocols.

In the literature, we identify three approaches to model the underwater acoustic channel: deterministic, statistical and hybrid. Deterministic models represent the channel as a function of different input variables, such as the employed frequencies, the distance, and the like. Among these deterministic channels, we mention channel simulators and ray tracers, such as [27], which, based on the environmental characteristics, and by using the physics of the acoustic propagation, provide a channel impulse response at a certain moment and position.

Even though these models are useful to better understand the cause-effect relationship between the environment and the communication performance, they are limited in representing the time variability and the space distribution of the quality of the channel. For this reason, statistical models have been proposed in [11, 12], specifically for representing the time-varying conditions over fixed links. Nevertheless, these models cannot be completely generalized to different scenarios, e.g., with different bathymetry, sound speed profiles and surface conditions.

Therefore, hybrid channel models try to represent both the time-varying conditions and the deterministic components of the channel impulse response, which could be derived from the geometry of the scenario. Nevertheless, the usability of these models is limited, since they require both a sufficient knowledge of the environment, like the deterministic models, and of the level of time-variability, like statistical models, thus leading to a cumbersome parameterized model.

We now give an example of a model proposed in [26], that is sufficiently detailed to give insight, especially for deployment, but general enough to be easily applied on different scenarios. In the literature, this model is also used to infer the performance of network protocols, nevertheless, as proved in [28, 29] a channel simulator, properly fed with time-varying environmental conditions, should be employed in order to obtain more accurate results.

3.3.3 Example of a Path Loss Model

Path loss $A(d, f)$ is defined as the attenuation on a single path from the transmitter to the receiver. As part of the transmitted power $\mathrm{P_{tx}}$ is lost, mainly due to spreading loss and absorption loss, the received power is:

$$\mathrm{P_{rx}} = \frac{\mathrm{P_{tx}}}{A(d, f)} \tag{3.1}$$

Spreading loss is due to the distribution of the fixed amount of transmitted power over an increasingly larger surface area when the signal propagates away from the source. This kind of loss is expressed as a polynomial function of the distance between the source and the destination; its degree (k), called the spreading factor, depends on the geometry of the propagation. In shallow water waves spread with a cylindrical shape ($k = 1$) whereas in deep water waves experience spherical propagation ($k = 2$).

The absorption loss is due to the conversion of acoustic pressure into heat. The absorption loss is computed through the absorption coefficient $a(f)$ which is a function of signal frequency. This function has been proposed by Thorp, who found a fitting function from empirical measurements obtained with low-frequency signals.

$$a(f) = 0.11\frac{f^2}{1+f^2} + 44\frac{f^2}{4100+f^2} + 2.75 \cdot 10^{-4} f^2 + 0.003. \tag{3.2}$$

The absorption coefficient for frequency above a few hundreds Hz is presented in Equation (3.2), and is measured in $[\mathrm{dB/km}]$ while frequency is expressed in kHz.

Path loss is described by the equation (3.3) expressed in linear scale.

$$A(d, f) = d^k a(f)^d \tag{3.3}$$

where d^k is the counterpart of radio attenuation in the air and $[a(f)]^d$ is called the absorption loss.

3.3.4 Noise in Underwater Channel

The main causes of noise in the underwater environment are turbulence, shipping, wind, and thermal noise. These major sources of noise are dominant in different bands of the signal spectrum. In Figure 3.1 the PSD of noise is depicted with different colors in order to stress this fact.

Noise PSD is impacted by turbulence in the very low frequency region ($f \leq 10$ Hz), whereas it is influenced by shipping in the band from ten to a hundred Hz. In the following region, which is the operating region of the majority of acoustic systems, the most important noise source is wind. Finally thermal noise, which is the noise due to electrical components in the receiver circuits, is dominant in the region beyond a hundred kHz. These contributions are expressed in terms of power spectral density.

$$\mathrm{N_t}(f) = 17 - 30\log(f) \tag{3.4}$$

$$\mathrm{N_s}(f) = 40 + 20(s - 0.5) + 26\log(f) - 60\log(f + 0.03) \tag{3.5}$$

$$\mathrm{N_w}(f) = 50 + 7.5w^{1/2} + 20\log(f) - 40\log(f + 0.4) \tag{3.6}$$

$$\mathrm{N_{th}}(f) = -15 + 20\log(f) \tag{3.7}$$

3.3.5 Signal to Noise Ratio at the Receiver

From the above model, the SNR can be inferred as the ratio between the received power usually expressed in $\mu\mathrm{Pa}$ and the noise power in the signal band. In the following, we do not use this model, but we estimate this metric on the available data set. However, this part of the study is useful to investigate further the relationship between the communications performance, the distance, and the employed carrier frequency. Assuming that the signal

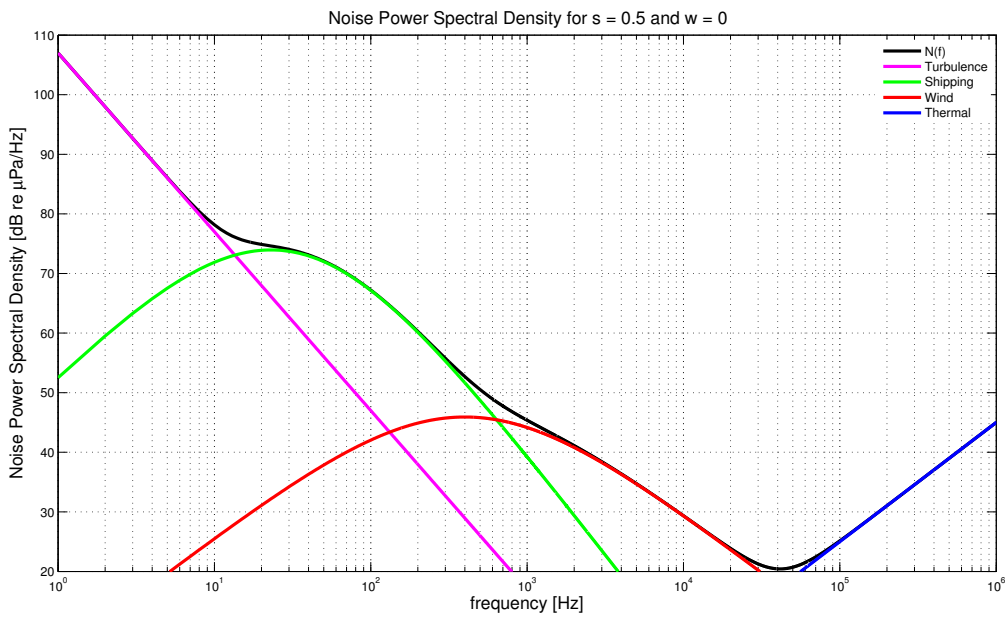

Figure 3.1. *Power spectral density of noise in the underwater channel.*

is transmitted in a sufficiently narrow band, the noise PSD can be approximated with a constant value. Hence the SNR becomes:

$$\mathrm{SNR} = \frac{\mathrm{P_{rx}}}{B(d)N(f)}. \tag{3.8}$$

Combining equation (3.1) with equation (3.8) we get:

$$\mathrm{SNR} = \frac{\mathrm{P_{tx}}}{A(d,f)N(f)B(d)} \tag{3.9}$$

Drawing the quantity $\frac{1}{A(d,f)N(f)}$ it can be noticed that an optimal transmission frequency exists that maximizes SNR. This is depicted in Figure 3.2. In this study a piece-wise log-linear approximation of the optimal frequency and bandwidth derived in [30] is employed. Figure 3.3 shows the dependence on distance of both the optimal communication frequency $f_0(d)$ and the bandwidth $B(d)$, defined as $B(d) = \{f : \mathrm{SNR}(d,f) \geq \mathrm{SNR}(d,f_0)/2\}$. Since the actual frequency and bandwidth values are obtained by lengthy numerical integrations, a piece-wise log-linear approximation for both $f_0(d)$ and $B(d)$ is employed. This approximation is obtained by calculating the coefficients ϕ_0, ϕ_1, of the tangent lines in the actual trend of $f_0(d)$ and $B(d)$ in logarithmic scale, hence frequency (in logarithmic scale) is given by:

$$f = \phi_0 + \phi_1 d \tag{3.10}$$

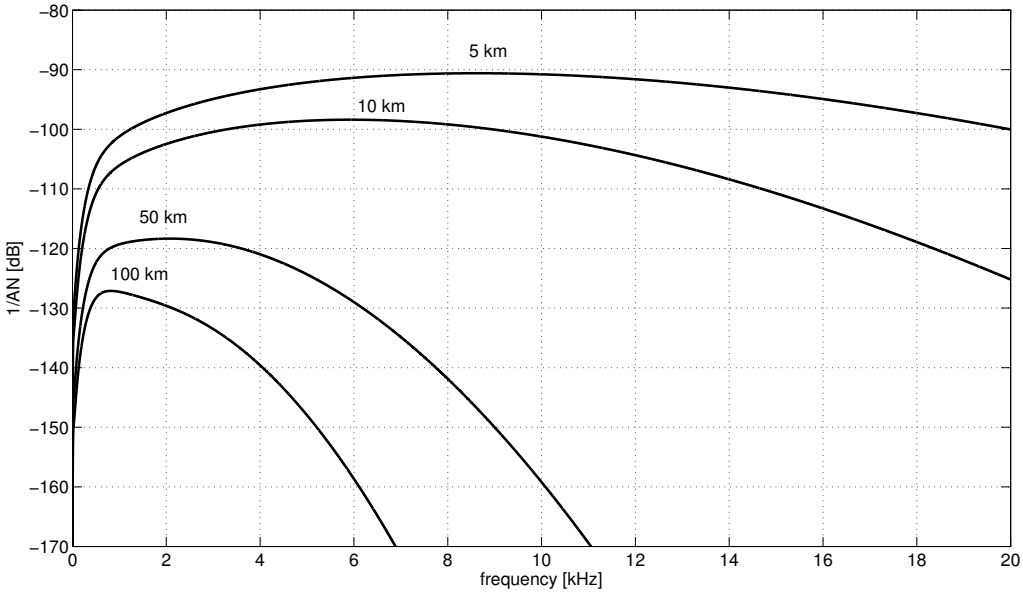

Figure 3.2. *The quantity* $(A(d, f)N(f))^{-1}$ *drawn for some distances.*

where d is also in logarithmic scale. The accuracy of these approximations is shown in Figure 3.3.

3.4 Channel Characterization from Experimental Data

3.4.1 Estimates of Channel Impulse Responses

In this section, we present the estimates of the CIR for the underwater acoustic channels measured during SPACE08, SubNet09, and KAM11. This study is required for the following statistical characterization.

We estimate the CIR by using the HFM and LFM pulses, during the three experiments. These waveforms have been specifically designed to have a peaked autocorrelation function, so as to provide a first estimate of the channel, by simply applying an energy correlator at the receiver, i.e., by matching the transmitted waveform with its reversed complex conjugated replica. It can be noticed that these estimates are accurate only if the SNR is sufficiently high. We recall that the three experiments have also different observation periods, and therefore the results are limited to those intervals. However, we will show here plots that juxtapose

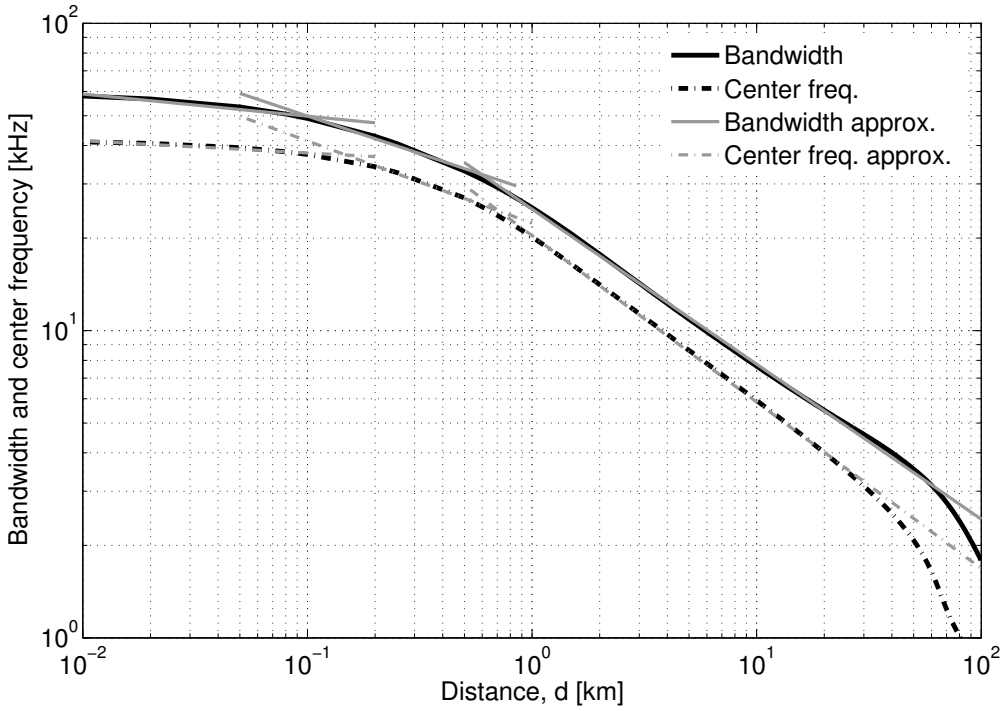

Figure 3.3. *Piece-wise log-linear approximation of $B(d)$ and $f_0(d)$ as a function of distance.*

consecutive channel realizations: the time at which the realization is measured is reported on the y-axis, whereas the x-axis shows the observation time within a single realization.

In particular, for SPACE08, we consider the train of fast LFM pulses, which lasts almost one minute and was repeated three times. This experiment was designed in order to obtain high SNR at the receiver, thus providing accurate estimates of the CIR. The repetition of three files, each consisting of a train of LFM pulses, makes it possible to constantly estimate instantaneous realizations of the channel for a time interval of almost three minutes. Since the time interval between two consecutive pulses is exactly known, the estimates of the CIRs could be aligned with respect to the first arrival. In this way, it is possible to follow the fluctuations of each arrival. Figure 3.4 represents the estimates performed on a file received during Julian date 295 at noon, between the source and the first hydrophone at S5.

For SubNet09, we obtain the CIRs from the HFM, which were embedded in the JANUS format at the beginning of the packet. However, since the received SNR was not always sufficient to get accurate estimates for all receivers, we consider only the signals measured at the deepest hydrophone H4 ($80\,\mathrm{m}$), at which the received SNR was sufficient. Transmissions were made every 30 seconds during a period of up to 9 hours. Nevertheless, the transmitter

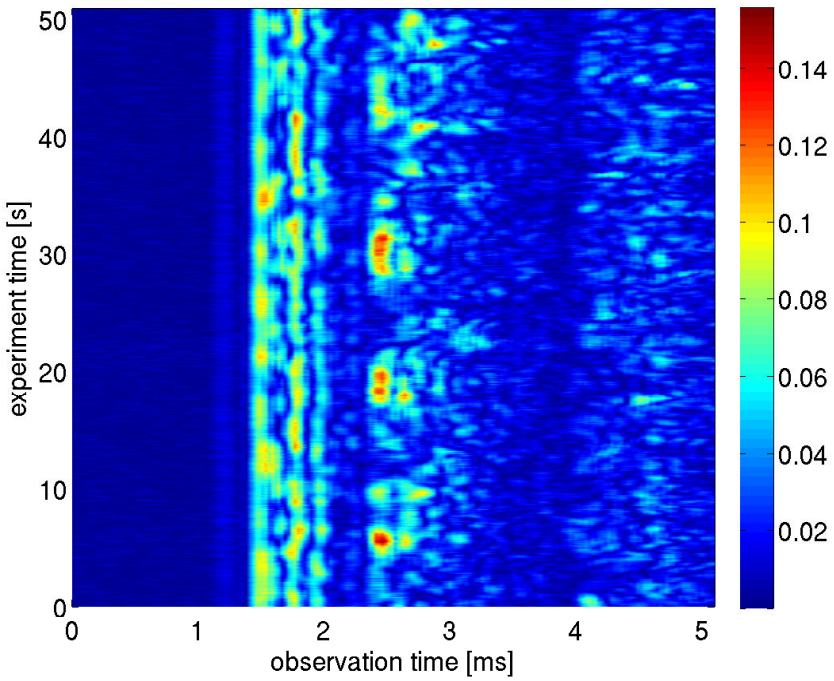

Figure 3.4. *Pseudocolor plot of the amplitude of the CIR measured during SPACE08, at S5, which is* $1000\,\mathrm{m}$ *from the transmitter.*

and the receiver were not synchronized with respect to a shared clock, and therefore it was not possible to synchronize all the estimates to the first arrival, but rather we aligned them with respect to the maximum amplitude arrival. In this way we could not track the time fluctuations of each arrival. From Fig. 3.5, we can observe that link T1–H4 is quite stable: a second, faint arrival is found between 10 and $20\,\mathrm{ms}$, and a very strong main arrival is sometimes preceded by a smaller reflection.

During KAM11, the same LFM pulses used for SPACE08 were employed, therefore we could use the same estimation process for this experiment. However, the one minute file was repeated six times, so as to provide an estimate over an interval lasting six minutes. In this way, we could get insights on the fluctuations of the CIR over that interval. Figure 3.6 shows a pseudocolor plot of the amplitude of the CIR, measured at receiver R1, which was $3\,\mathrm{km}$ from the source. The observation time is about three minutes and a half, since after that, a synchronization problem occurred.

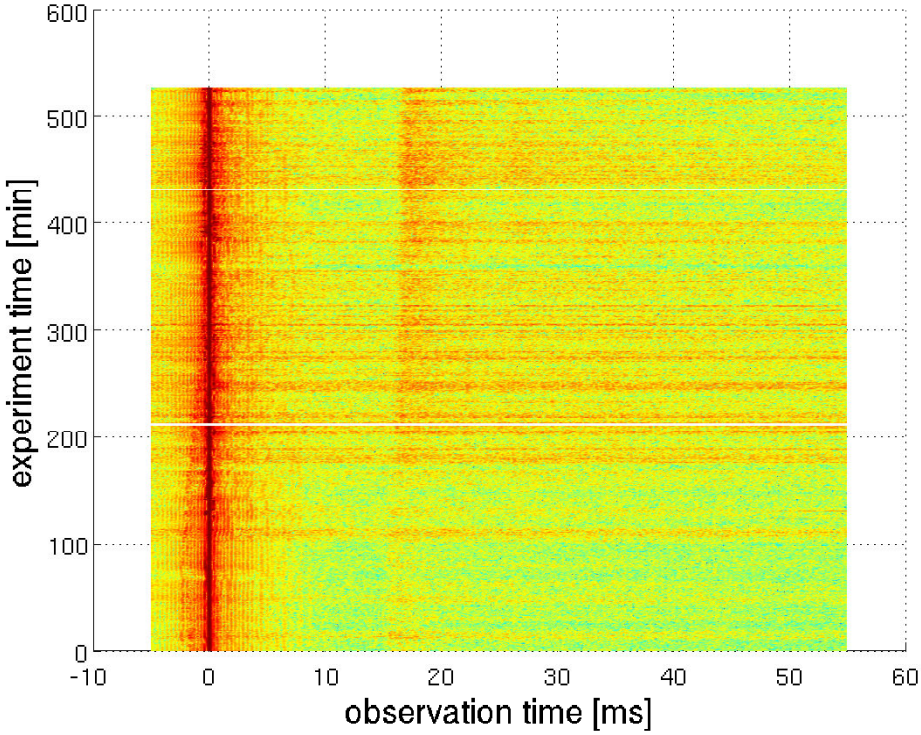

Figure 3.5. *Pseudocolor plot of measured channel impulse response amplitudes for the link between T1 and H4, during SubNet09, on June 5th.*

3.4.2 Time Correlation Coefficient

The correlation coefficient is estimated starting from the CIR. Given the set $\mathcal{C}_\tau$ of all pairs of responses separated by a time lapse of τ, we align these responses to the time of arrival of their respective maximum-amplitude taps, we compute the normalized correlation of signals within each pair, and finally take the average over all pairs in $\mathcal{C}_\tau$ as follows [31]

$$\rho(\tau) = \frac{1}{|\mathcal{C}_\tau|} \sum_{\mathcal{C}_\tau} \frac{\left| \sum_t g^*(t,0) g(t,\tau) \right|}{\sqrt{\sum_t |g(t,0)|^2 \sum_t |g(t,\tau)|^2}}, \tag{3.11}$$

where $g(t,0)$ and $g(t,\tau)$ are any two channel responses separated by a time lapse of τ, and $|\mathcal{C}_\tau|$ is the cardinality of the set containing such pairs.

The time correlation coefficient measured during SPACE08 on Julian date 295 is shown in Fig. 3.7. The coefficient ρ is estimated by considering CIRs, presented in Fig. 3.4, for the links between the source and all the receivers. We can notice that the correlation coefficient

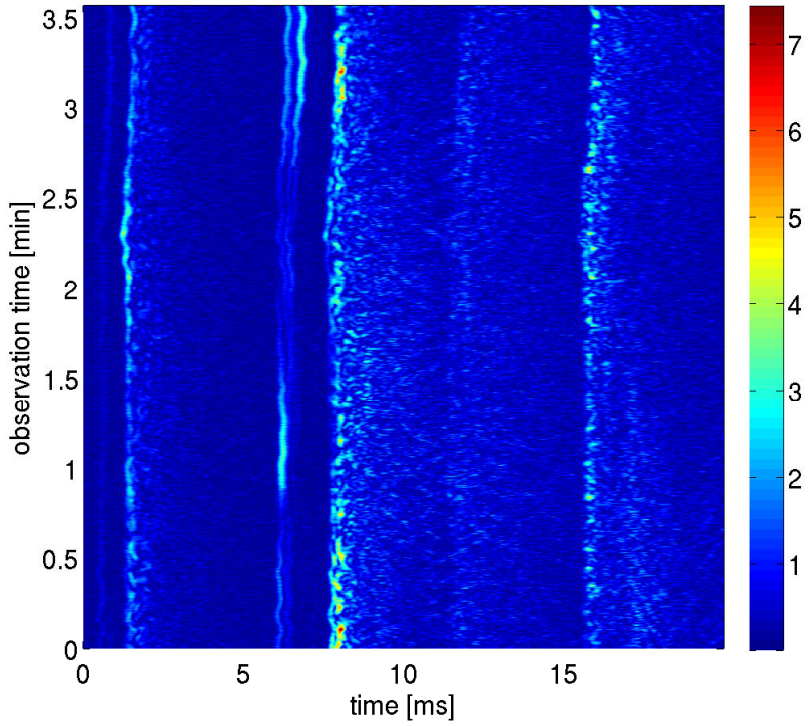

Figure 3.6. *Pseudocolor plot of measured channel impulse response amplitudes at receiver* $R1$ *at* $3\,\mathrm{km}$ *from the transmitter, on Julian date* 187*, at 8 am GMT, during KAM11.*

increases in correspondence to the almost-periodic fourth arrival peak, which occurs every ten seconds. The same behavior can be observed for signals at S6, whereas less correlated CIRs are measured at the shorter links, S3 and S4. Here, we showed the correlation coefficient, estimated among the CIRs in only one file, lasting almost one minute. Therefore, the same study can be applied to all the files, in order to infer the time variability of the correlation function.

For SubNet09, given the experimental setup, the values of τ we can measure are integer multiples of $30\,\mathrm{s}$: for instance, for $\tau = 30\,\mathrm{s}$, we perform an ensemble average of the correlation coefficients between all signals transmitted at $(0, 30\,\mathrm{s})$, $(30\,\mathrm{s}, 60\,\mathrm{s})$, and so forth. Fig. 3.8 collects the correlation coefficients of the channel impulse responses as a function of the time displacement τ for the links between all transmitters and H4. The general behavior of the curves is to decrease to a fairly stable value, which depends on the transmitter-receiver pair. By defining the coherence time as the offset after which the correlation coefficient falls below some practical value (say, 0.8 [7]), we observe that, from the previous evalu-

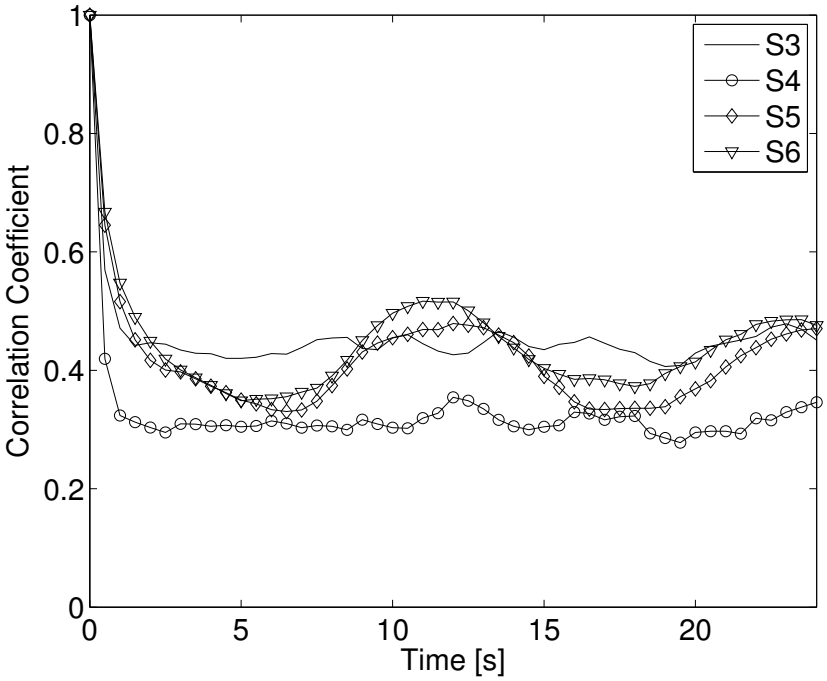

Figure 3.7. *Channel correlation coefficient ρ as a function of the time lapse τ, during SPACE08, at Julian date 295, noon (GMT).*

ation, we can infer the coherence time for these links. In particular, we note that within the inter-transmission time interval of $30\,\mathrm{s}$ the correlation of the T3–H4 channel falls quite abruptly, suggesting that the coherence time is indeed short; a higher rate of signal transmission would help estimate the actual coherence time with greater precision.

For KAM11, we replicate the same study as that performed for SPACE08. Here we consider only the closest receiver (R1 at $3\,\mathrm{km}$), at Julian date 187 during the time interval for which we showed the CIRs. As expected, there is very low correlation between successive CIRs, separated in time by τ. In fact, during the chosen time window, patterns in the arrivals structure do not occur.

3.4.3 Power Delay Profile

The analysis of the CIR also provides some insight on its average duration, called the channel time spread, which is required for tuning the parameters of adaptive signal processing algorithms at the receiver. The channel time spread can be inferred from the PDP, i.e., the mean square value of the amplitude of the CIR. When considering the SubNet09

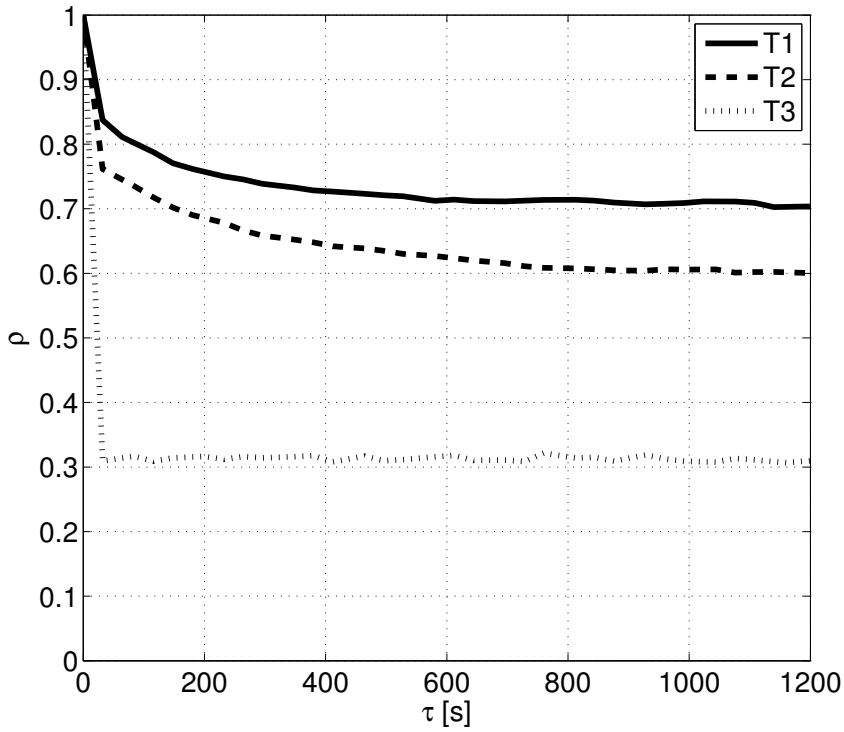

Figure 3.8. *Channel correlation coefficient ρ as a function of the time lapse τ in June. The considered links are from each transmitter T1, T2, T3 to hydrophone H4.*

data set, we consider arrivals spaced by at least $2\,\mathrm{ms}$ and carrying at least 1% of the energy of the peak arrival. All PDPs are normalized to their peak value and aligned to the time of the strongest arrival. The measured values for all links in June are summarized in Table 3.1.

Table 3.1. *Measured time spread in* ms *for all links in June.*

tx/rx	T1	T2	T3
H1	20	20	3
H2	18	22	5
H4	~ 0	15	10

In regard to the SPACE08 and KAM11 data sets, we show here the time series of the estimated channel time spread, during one specific day. In particular, for SPACE08, we consider Julian date 296. The time series is shown in Fig. 3.10: each point represent the

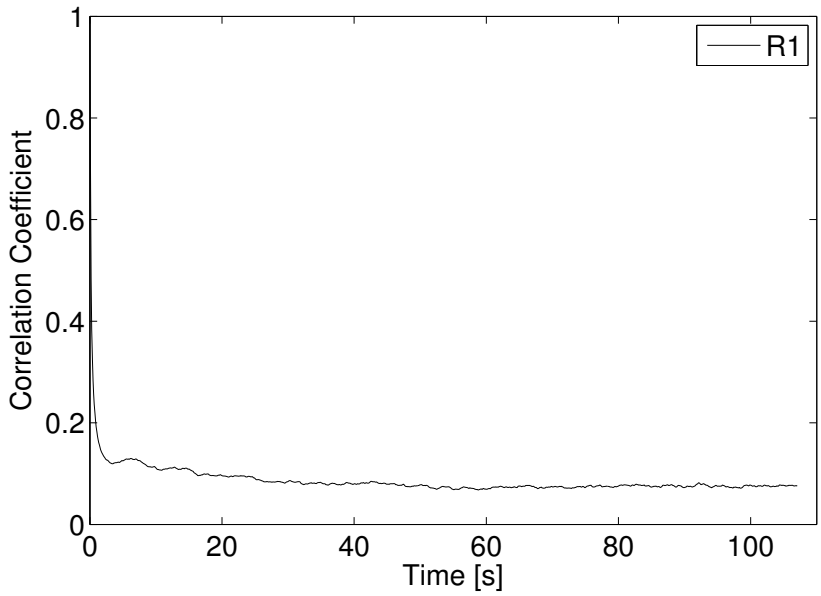

Figure 3.9. *Channel correlation coefficient ρ as a function of the time lapse τ, during KAM11, Julian date* 187*, 8 am, at receiver R1.*

measured value of the duration of the power delay profile, estimated over one file every two hours. The time spread is defined here as the interval of time within which 90% of the power delay profile lies. From Fig. 3.10, it can be noticed that longer links are less affected by multipath arrivals, which may be absorbed before reaching the receiver. However, the time spread does not exceed $3\,\mathrm{ms}$ at all the receivers, thus representing quite good conditions. Analogously, we show the results for KAM11, for Julian date 187 and receiver R1. Fig. 3.11 represents the time series of the time spread during one day. It is worth noting how the time spread varies in one day, from a minimum value of $7\,\mathrm{ms}$ to a maximum of $20\,\mathrm{ms}$. These conditions heavily affect the communication performance in terms of SNR, and consequently BER and even PER, if proper decoding algorithms are not employed.

3.5 Average Channel Quality Metrics

3.5.1 Instantaneous and Average Signal to Noise Ratio

Here, we show the instantaneous input SNR, estimated from the data collected during the SubNet 2009 sea trials and the average output SNR, inferred from the KAM11 data set. We exploit the sent probe signal, a chirp or a set of frequency-hopped frequency-shift keying

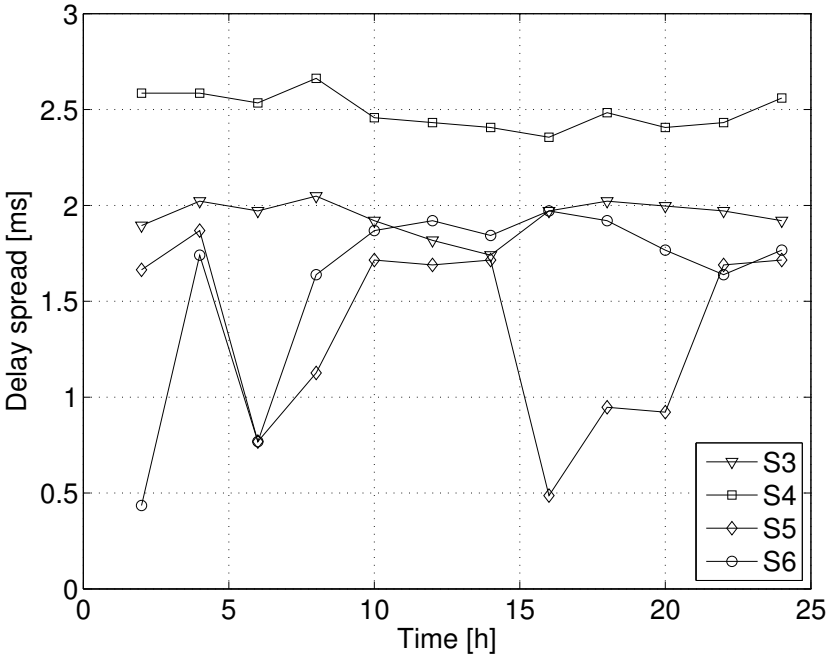

Figure 3.10. *Time spread estimate τ as a function of time, during the Julian date 296 at receivers S3, S4, S5 and S6, in SPACE08.*

modulation symbols, in order to obtain SNR traces. This SNR is an instantaneous estimate of the ratio between the received energy, subtracted by the in band noise power, and the noise power.

We consider the experiment starting at 23:30 GMT on 30 August 2010 and lasted until 8:33 GMT on the following day. For reference, we report in Figure 3.12 an example of SNR time series, for the links between transmitter T1 and all hydrophones, for an experiment lasting almost 9 hours, where transmissions were performed once every $15\,\mathrm{s}$. From this figure we observe a higher SNR on average for the T1–H4 link, which is due to the downward-refractive behavior of the channel during SubNet09; in addition, we observe that in this particular case all links experience time-varying fading effects, as not only do the SNR samples oscillate around their average value, but this average value also varies following changes in propagation conditions (for example, the SNR over T1–H2 steadily increases throughout the experiment).

During KAM11, we evaluate both the input and what we call output SNR, averaged over one second. The latter is estimated as the ratio between the energy associated to a transmit-

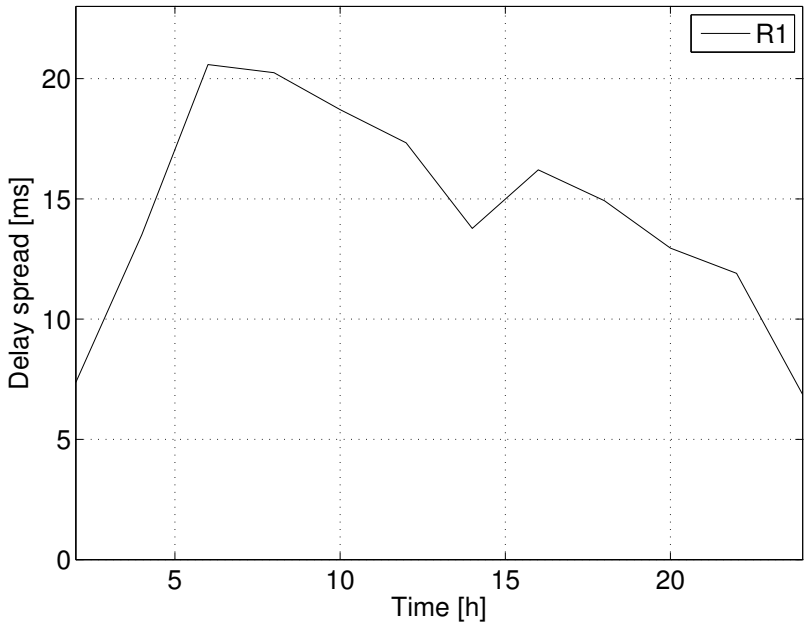

Figure 3.11. *Time spread estimate τ as a function of time, during the Julian date 187 at receiver R1 in KAM11.*

ted symbol and the power of the noise plus the interference process. We can estimate this value by considering the software decision at the output of an equalizer. Here, in particular, we consider a Decision Feedback Equalizer (DFE). We show here the time series of the observed SNRs over an interval of six minutes at 4 am on Julian date 187 and at 00 am on date 188. The length of the observation interval allows us to measure the fluctuations of the SNR due to both rapid and slow environmental changes.

In Figures 3.13(b) and 3.14(b) we plot the estimated output symbol SNR, averaged over a packet, at times 4 am and 00 am, respectively. The used parameters for the DFE are: a feed-forward filter length of $1\,\mathrm{ms}$, a feedback filter length of $10\,\mathrm{ms}$, and we are combining the received signals at channels 1, 4, 7 and 10, which respectively are $45.55\,\mathrm{m}$, $45.4\,\mathrm{m}$, $45.25\,\mathrm{m}$ and $45.1\,\mathrm{m}$ below the surface.

Over the observation interval, the SNR varies between 9 and $17\,\mathrm{dB}$ at 4 am, and between 4 and $12\,\mathrm{dB}$ at 00 am. We observe a quite smooth and almost periodic fluctuation, in both Figures 3.13(b) and 3.14(b). In fact, we can see an increased SNR at minutes one and five in Figure 3.13(b), and at minutes three and five in Figure 3.14(b). This behavior suggests that it may be possible to predict the communication system performance over subsequent

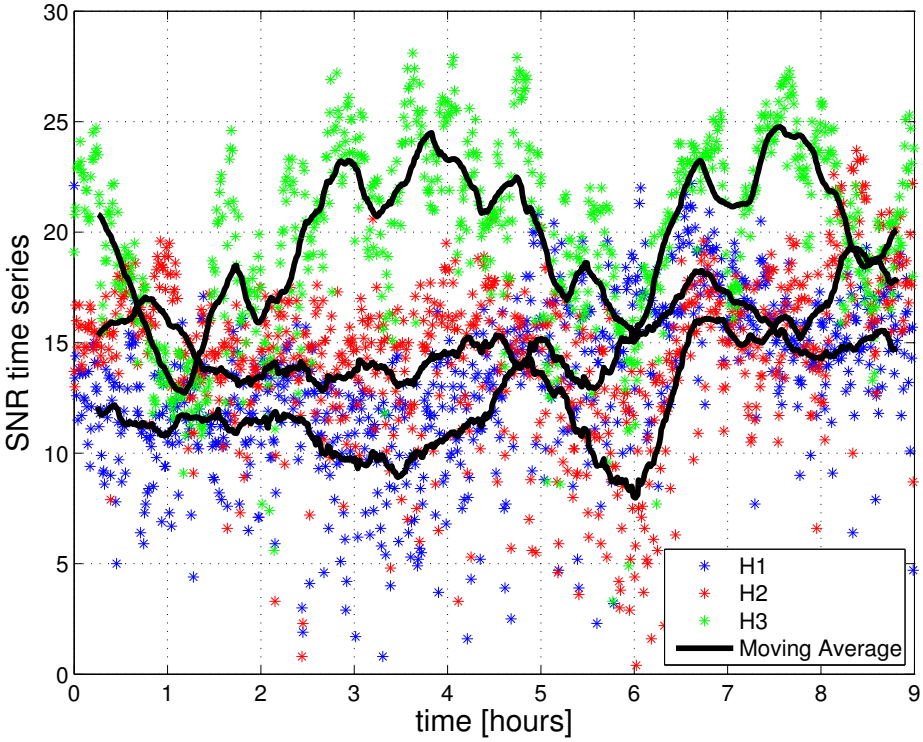

Figure 3.12. *Time series of SNR in* dB *for transmissions between T1 and all hydrophones during an experiment in SubNet09. Moving averages are provided as a solid black line.*

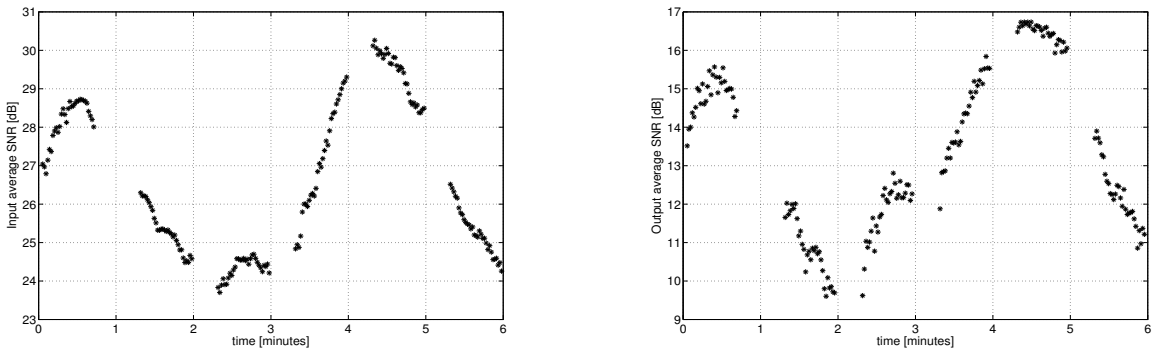

(a) Average input SNR on Julian date 187, at 4 am during KAM11.

(b) Average output SNR on Julian date 187, at 4 am during KAM11.

Figure 3.13. *Julian date 187, at 4 am during KAM11.*

packets: we will investigate this topic in Chapter 5.

Figures 3.13(a) and 3.14(a) show the average packet input SNR, which is computed as the ratio between the average energy of the received packet and the in band noise power measured before the train of packets. We observe the same fluctuations that we notice for the

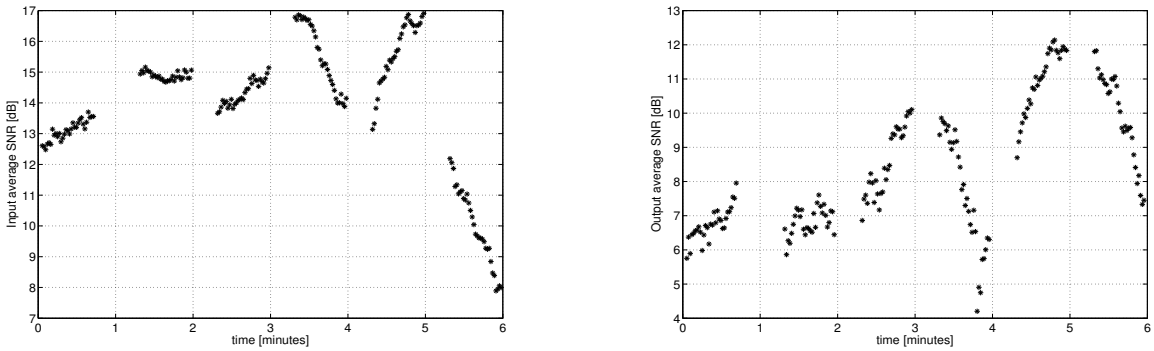

(a) Average input SNR on Julian date 188, at 00 am during KAM11.

(b) Average output SNR on Julian date 188, at 00 am during KAM11.

Figure 3.14. *Julian date 188, at 00 am during KAM11.*

output SNR, even though the input SNR varies between 24 and $30\,\mathrm{dB}$ in Figure 3.13(a) and between 7 and $17\,\mathrm{dB}$ in Figure 3.14(a). The correlation between the input and output SNRs is more evident in Figure 3.13 than in Figure 3.14, because for that epoch the strongest arrival was not always the most stable. The gap between the input and output SNR represents the loss due to ISI and shows how strong the most stable arrival is relative to the other arrivals. We measure and show the input SNR, in order to test and prove that the fluctuations observed for the output SNR were caused by the environment and not by the post-processing on the data. Given that we observe the same almost periodical behavior for the average input and output SNRs, we can conclude that those fluctuation are environment-driven.

We can also observe that the decrease or increase rate of the input and output SNR are slightly different, thus suggesting that the relative strength of the most stable arrival to the multipaths arrivals is not constant over time, but rather depends on the rapidly varying not-consistent arrivals, causing ISI. Comparing Figures 3.13 and 3.14, we can also notice that higher input SNRs, such as those in Figure 3.13(a), do not always correspond to an equivalent improvement of the output SNRs. For example, we observe a gap between the input SNRs, at dates 187 and 188 around the sixth minute, of about $16\,\mathrm{dB}$, whereas the corresponding gap between the output SNRs is only about $4\,\mathrm{dB}$. This means that, for the system under consideration (wide-band, single carrier), if we increase the transmission power, we do not always get correspondingly better communications performance. This is why, in a frequency selective scenario, power control and adaptive modulation techniques do not

have the same performance. In this case, power control would not improve the system performance as much as an updated adaptive modulation scheme would. Also for this reason we will investigate this technique in Chapter 4.

3.5.2 Channel Energy Time Series

Another metric, proportional to the input SNR, is the channel energy, which we estimated for the SPACE08 data set. Specifically, we analyze its fluctuations in time. Calling $g(t)$ the estimated channel impulse response measured in the time interval $t \in [0, NT_s]$, we estimate the energy as:

$$E_g = T_s \sum_{i=0}^{N-1} |g(i)|^2 \tag{3.12}$$

where T_s is the sampling interval. We compute the channel estimate over segments of the received signal that are 400 symbols long (which corresponds to $60\ \mathrm{ms}$). After each estimation we shift the window by 100 symbols, which corresponds to $15\ \mathrm{ms}$, resulting in an estimate every $15\ \mathrm{ms}$ over windows of $60\ \mathrm{ms}$. Figs. 3.15(a), 3.15(b), 3.16(a) and 3.16(b) show the energy time series during Julian dates from 292 to 301 (which corresponds to days from October 18 to 27) in a dB scale. We can notice that the energy of the communication channel between the transmitter and the closest receivers (S3 and S4) is spread in the same interval, $[-26, -38]\ \mathrm{dB}$, whereas the energy of links between the source and systems S5 and S6 exhibits greater macro variability[1]. More specifically the energy of the channel between the transmitter and S5 is in the interval $[-75, -45]\ \mathrm{dB}$, and the range of fluctuations at S5 is much greater than it is at S6. This observation implies that not only the distance but also the orientation between the transmitter and the receiver matters for underwater acoustic communications. It can be noticed that the four time series have the same main fluctuations: this suggests that those macro fluctuations are due to environmental changes which affect the receivers in the same way.

3.6 Wide Sense Stationarity Validation

In this section, we address the problem of validating the wide-sense stationarity assumption, which is usually made when estimating the statistics of a process. First, we will briefly

[1]For macro variability we mean fluctuations over intervals of several hours

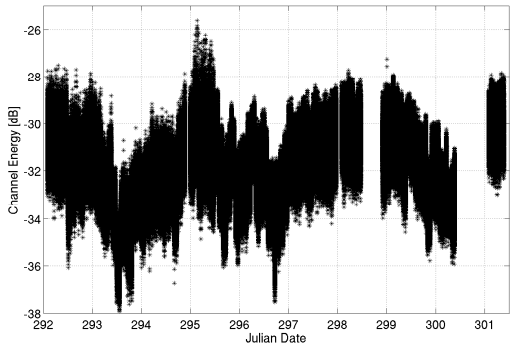

(a) Channel energy time series at S3 from Julian Date 295 to 301.

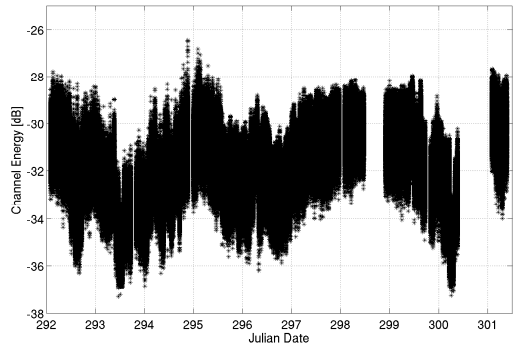

(b) Channel energy time series at S4 from Julian Date 295 to 301.

Figure 3.15. *Channel energy of the link between the source and receiving stations S3 and S4 (*200 m *Southeast and Southwest).*

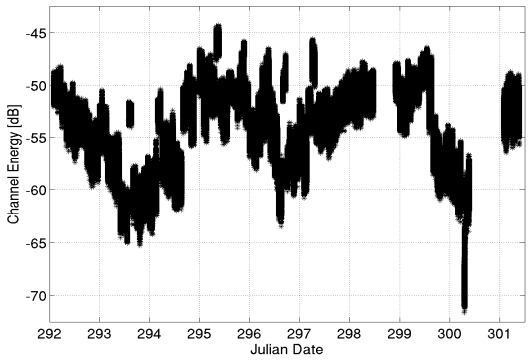

(a) Channel energy time series at S5 from Julian Date 295 to 301.

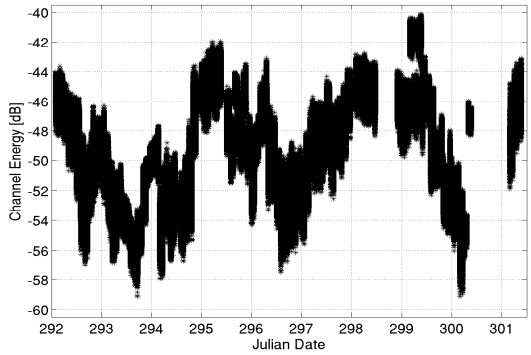

(b) Channel energy time series at S6 from Julian Date 295 to 301.

Figure 3.16. *Channel energy of the link between the source and receiving stations S5 and S6 (*1000 m *Southeast and Southwest).*

present the methodology that we used and the results regarding the channel energy for the SPACE08 data set, which is the one presenting the most stable time series of the communication performance. The same study could be applied to the SubNet09 and KAM11 data sets, which however have not been considered here. In fact, the former is not suitable for this study, since the intervals of observations were too long (15 s), whereas the latter has just been collected and work is in progress.

3.6.1 Stationarity Test

The used procedure is described in detail in [32] but is also briefly presented here. The method aims at determining the stationarity time scale of a signal by comparing the local spectra statistics to the global spectrum, obtained by marginalization. We compute the local spectra by using the multitaper spectrogram defined as:

$$S_{g,K}(t,f) = \frac{1}{K}\sum_{k=1}^{K} S_g{}^{(h_k)}(t,f), \tag{3.13}$$

where $S_g{}^{(h_k)}(t,f)$ is the spectrogram computed with the k-th Hermite function, and is given by:

$$S_g{}^{(h_k)}(t,f) = \Big|\int g(s)h_k(s-t)e^{-i2\pi fs}ds\Big|^2. \tag{3.14}$$

The symbol $h_k(t)$ stands for the k-th Hermite function, whose length is T_h. We will vary T_h in order to test the stationarity for different time intervals. Usually what one can do is to consider the variability of the local spectra with respect to the global spectrum but, given that a variability is always observed, we need to compare these variations to those between the local and global spectra of the surrogate data. A surrogate data set is a stationarized version of the experimental data set. It is obtained by multiplying the amplitude of the Fourier transform of the original time series by an independent identically distributed phase sequence and then applying the inverse Fourier transform. In this way the correlation function of the obtained process depends only on the interval between two sequences and not on the absolute times at which they are taken. What we compute are just realizations of the random process, therefore computing more realizations by randomization improves the test. We will call the number of randomizations J. Then we compute the distance between the local spectra and the Global Spectrum (GS) obtained by marginalization, which can be expressed as:

$$\text{GS} = E[S_{g,K}(t,f)]_t = \frac{1}{T}\sum_{i=1}^{T} S_{g,K}(i,f). \tag{3.15}$$

The distance we compute is defined as a combination of the Kullback-Leibler divergence and the log-spectral deviation, respectively defined as [33]:

$$D_{KL}(L,G) = \int_{\Omega}(L(f)-G(f))\log\frac{L(f)}{G(f)}df, \tag{3.16}$$

$$D_{LSD}(L,G) = \int_{\Omega} \left| \log \frac{L(f)}{G(f)} \right| df, \tag{3.17}$$

where $L(f)$ and $G(f)$ are respectively the local and the global spectrum, and f is the frequency variable over the space Ω. The combination that we consider is the following:

$$D(L,G) = D_{KL}(\tilde{L},\tilde{G}) \cdot (1 + D_{LDS}(L,G)) \tag{3.18}$$

where $\tilde{L}$ and $\tilde{G}$ are the normalized versions of L and G. We compute the N distances between the N local spectra and GS, and for each surrogate data we do the same, i.e., we have J sets with N distances each. We consider the variance of each set of N distances, hence only a value for the original data which we will indicate as Θ_1 and J values for the surrogates, which we will indicate as a vector $\mathbf{\Theta}_0$. The authors in [32] showed that the elements of $\mathbf{\Theta}_0$ can be thought as realizations of a random variable γ distributed according to a Gamma distribution, which can be represented by the following probability distribution function:

$$f(x;a,b) = x^{a-1} \frac{\exp^{\frac{-x}{b}}}{b^a \Gamma(a)} \text{ for } x \geq 0, \tag{3.19}$$

where a and b are two positive parameters. Thanks to this result, we can estimate the parameters of the Gamma distribution from the variances computed on surrogates. We choose a probability of failure of the test (in our case 5%) and, from the cumulative distribution function, we determine the threshold of the variance such that the probability that the variance is less than or equal to that threshold is 95% (we will call this threshold α). Then the test can be written as:

$$d(x) = \begin{cases} 1 & \text{if } \Theta_1 > \alpha : \text{non stationary;} \\ 0 & \text{if } \Theta_1 \leq \alpha : \text{stationary.} \end{cases} \tag{3.20}$$

When the hypothesis of stationarity is rejected, a measure of non-stationarity, which is called index of non-stationarity ($\mathcal{INS}$) is defined as

$$\mathcal{INS} := \sqrt{\frac{\Theta_1}{E[\gamma]}}, \tag{3.21}$$

where $E[\gamma]$ is the average value of the random variable, which we approximate as the average of the elements in the vector $\mathbf{\Theta}_0$. Given that the $\mathcal{INS}$ depends on the length of the Hermite window T_h, the authors in [32] defined a scale of non-stationarity ($\mathcal{SNS}$) which is the normalized value of T_h such that the $\mathcal{INS}$ is maximum:

$$\mathcal{SNS} = \frac{1}{T} \arg\max_{T_h} \mathcal{INS}(T_h). \tag{3.22}$$

This scale of non-stationarity gives a measure of how variable the process is. In this work we do not compute this measure, because we are primarily interested in the stationarity interval, but leave it as an interesting topic for future study.

3.6.2 The Interval of Stationarity

In this subsection, we present the results of the stationarity test and the estimate of the interval of stationarity. In particular, we are interested in assessing the wide-sense stationarity over different time scales: a short time scale (of the order of tenths of a second) which concerns physical layer applications, and a long time scale (of the order of tens of seconds) for upper layer applications, such as Automatic Repeat reQuest (ARQ), medium access control (MAC) and routing protocols. For example, we want to understand whether or not we can assume stationarity in case we want to develop a predictor of the link quality in the second layer of the ISO/OSI architecture, which is responsible for packet reliability and for medium access control. In this case we can trigger decisions, such as not to access the channel in the next step because the predicted channel quality is bad. Nevertheless, for a scenario where the distances of nodes are between some hundreds of meters to a few kilometers, the packet travel time [2] is between tenths of seconds to one second [3], so that, considering the feedback and possible retransmissions allowed in the protocol, the delivery time becomes of the orders of a few seconds.

In the implementation of the procedure [34], we test the stationarity of the process in a time window $90\,\mathrm{s}$ long, and we choose to compute $J = 50$ randomizations. T_h is varied from 1001 to a third of the length of the time series, with increments of 500 samples at every iteration. We estimate the spectrum by using the first 10 Hermite functions and we estimate the Gamma distribution parameters as maximum-likelihood estimates.

The test, performed on the whole data set, gives as a result that the process is stationary for all the considered T_h. Therefore the process is stationary over at least a three-minute period. This is verified for all the receiving systems. This implies that we can study data adaptive estimators for both the physical and the upper layers, assuming stationarity for the received energy process. Moreover, thanks to this result, we can estimate the power spectral

[2] The travel time is the time that the sound wave needs to propagate from the transmitter to the receiver.

[3] We consider here a sound speed of $1500\ \mathrm{m/s}$, and distances between $200\ \mathrm{m}$ and $1500\ \mathrm{m}$

density of the overall energy over three-minute intervals, in order to see how variable the spectrum is over time.

3.7 Validation of a Hybrid Sparse Diffuse Channel Model for Underwater Acoustic Channels

In this section, we show the numerical results on the validation of a channel model, which has been proposed for ultra wideband channels in [1, 17, 35]. Underwater acoustic channels are actually ultra wideband, i.e., the bandwidth is comparable to the central frequency, as in the considered data sets. We also prove in Section 3.4.3 that the CIR can be thought as sparse, as also studies in [19,20] confirm. Here, we validate an hybrid sparse and diffuse channel, by using the SPACE08 data set, and we quantify how accurate this model is compared to the purely sparse or diffuse models.

3.7.1 Brief Model Overview

We consider a point-to-point underwater acoustic channel. The source transmits a sequence of M pilot symbols, $x(n), n = -(L-1), \ldots, M-L$, over a channel $h(l), l = 0, \ldots, L-1$ with known delay spread $L \geq 1$. The received discrete-time, baseband signal over the corresponding observation interval of length $N = M - L + 1$, is given by

$$y(n) = \sum_{l=0}^{L-1} h(l)x(n-l) + w(n), \quad n = 0, \ldots, N-1,$$

where $w(n) \in \mathcal{CN}(0, \sigma_w^2)$ is Independent and Identically Distributed (IID) circular Gaussian noise.

By collecting the N received, noise and channel samples in the column vectors

$$\mathbf{y} = [y(0), y(1), \ldots, y(N-1)]^T$$
$$\mathbf{w} = [w(0), w(1), \ldots, w(N-1)]^T \in \mathbb{C}^N$$
$$\mathbf{h} = [h(0), h(1), \ldots, h(L-1)]^T \in \mathbb{C}^L$$

respectively, and letting $\mathbf{X} \in \mathbb{C}^{N \times L}$ be the $N \times L$ Toeplitz matrix associated with the pilot sequence, with the vector of the transmitted pilot sequence $[x(-i), x(1-i), \ldots, x(N-1-i)]^T$

as its ith column, $i = 0, \ldots, L-1$, we have the following matrix representation:

$$\mathbf{y} = \mathbf{X}\mathbf{h} + \mathbf{w}. \tag{3.23}$$

The discrete baseband channel vector $\mathbf{h}$ is modeled according to the HSD model developed in [1,17] for UWB systems, *i.e.*,

$$\mathbf{h} = \mathbf{a}_s \odot \mathbf{c}_s + \mathbf{h}_d, \tag{3.24}$$

where $\mathbf{a}_s \odot \mathbf{c}_s$ is the *sparse component*, and $\mathbf{h}_d$ is the *diffuse component*. In particular, $\mathbf{a}_s \in \{0,1\}^L$ is the *sparsity pattern*, whose entries are equal to one in the positions corresponding to the resolvable multipath components, and zero otherwise; its entries are drawn IID from a Bernoulli RV with parameter q ,$\mathcal{B}(q)$, where $q \ll 1$ so as to enforce sparsity. The *sparse coefficient* vector $\mathbf{c}_s$ is modeled as a deterministic and unknown vector. Finally, we use the Rayleigh fading assumption for the diffuse component, $\mathbf{h}_d \sim \mathcal{CN}(\mathbf{0}, \Lambda_d)$, where Λ_d is diagonal, with diagonal entries given by the PDP $\mathcal{P}_d(k), k = 0, \ldots, L-1$.

Remark 3.7.1. We assume that $\mathbf{c}_s$ is a deterministic and unknown vector, because the statistics of the specular components, that vary according to the large scale fading, are usually difficult to estimate. On the other hand, the Rayleigh fading assumption for the diffuse component is consistent with the fact that it arises from the contribution of multiple paths in a single resolvable delay bin. Its amplitude and phase vary according to the small scale fading. Its PDP can be accurately estimated by averaging the fading over subsequent realizations of the fading process. This information may then be used to estimate the channel via the linear Minimum Mean Square Error (MMSE) estimator [36], which improves the accuracy over LS.

In [1,17] a three-step channel estimator is developed, and it is based on the HSD model:

1. The sparse coefficient vector $\mathbf{c}_s$ is estimated via LS, giving the estimate $\hat{\mathbf{c}}_s = \mathbf{h}_{LS}$.

2. The sparsity pattern $\mathbf{a}_s$ is estimated via M (MAP) [36], giving the estimate $\hat{\mathbf{a}}_s$. We will indicate this estimate as G-Thres, which means generalized thresholding estimator.

3. The diffuse component $\mathbf{h}_d$ is estimated via MMSE, based on the residual estimation error after removing the estimated sparse component, $(\mathbf{1} - \hat{\mathbf{a}}_s) \odot \mathbf{h}_{LS}$.

3.7.2 Power Delay Profile Modeling

In this section, we model the PDP of the diffuse component. In particular, we assume an exponential PDP, and we measure the fitting of this model to the sample PDP estimated from the data, based on the SPACE08 data set.

The source transmits a pseudo-noise sequence of length $60\,\mathrm{s}$, with symbols drawn from $\{-1, 1\}$ at rate $6510\,\mathrm{symbols/s}$. The corresponding received sequence is divided into sub-sequences of length $30\,\mathrm{ms}$ each, corresponding to $N = 194$ samples. Let $\mathbf{y}^{(i)}$ be the observation vector from the ith sub-sequence, and $\mathbf{X}^{(i)}$ be the Toeplitz matrix associated with the corresponding pilot sequence. A time series of LS channel estimates with delay spread $15\,\mathrm{ms}$ ($L = 97$ samples) is generated as $\mathbf{h}_{LS}^{(i)} = \left(\mathbf{X}^{(i)*}\mathbf{X}^{(i)}\right)^{-1}\mathbf{X}^{(i)*}\mathbf{y}^{(i)}$. This time series therefore represents the samples of the time-varying channel spaced in time $30\,\mathrm{ms}$ apart.

The sample PDP is computed by averaging over $N_{ch} = 1878$ subsequent channel realizations, corresponding to an observation window of $56\,\mathrm{s}$. We have

$$\hat{\mathcal{P}}_{sample}(k) = \frac{1}{N_{ch}} \sum_{i=0}^{N_{ch}-1} \left|\mathbf{h}_{LS}^{(i)}(k)\right|^2 . \tag{3.25}$$

We now evaluate the exponential model for the PDP of the diffuse component, and we compare it with the sample PDP estimated from the data. At this point, since we are not assuming any a priori model for the PDP, and therefore we cannot distinguish the specular components from the diffuse background, which is unknown, we keep the sparse component to compute the sample PDP and the exponential fitting.

Let $\mathcal{P}_d(k) = \beta e^{-\omega k}$, $k = 0, \ldots, L-1$ be the exponential PDP as a function of the channel delay. This is parameterized by the *power* β, and the *decay* ω. Notice that $\ln \mathcal{P}_d(k) = \ln \beta - \omega k = \rho - \omega k$, where we have defined $\rho = \ln \beta$. These parameters can be estimated by computing a linear fitting of $\ln \hat{\mathcal{P}}_{sample}(k)$, *i.e.*, by solving

$$\{\hat{\rho}, \hat{\omega}\} = \arg\min_{\rho,\omega} \sum_k \left|\ln \hat{\mathcal{P}}_{sample}(k) - \rho + \omega k\right|^2 . \tag{3.26}$$

We then determine the fitting error of the estimated exponential PDP with the sample PDP estimate as

$$f\left(\hat{\mathcal{P}}_{sample}\right) = \sum_k \left|\ln \hat{\mathcal{P}}_{sample}(k) - \hat{\rho} + \hat{\omega} k\right|^2 . \tag{3.27}$$

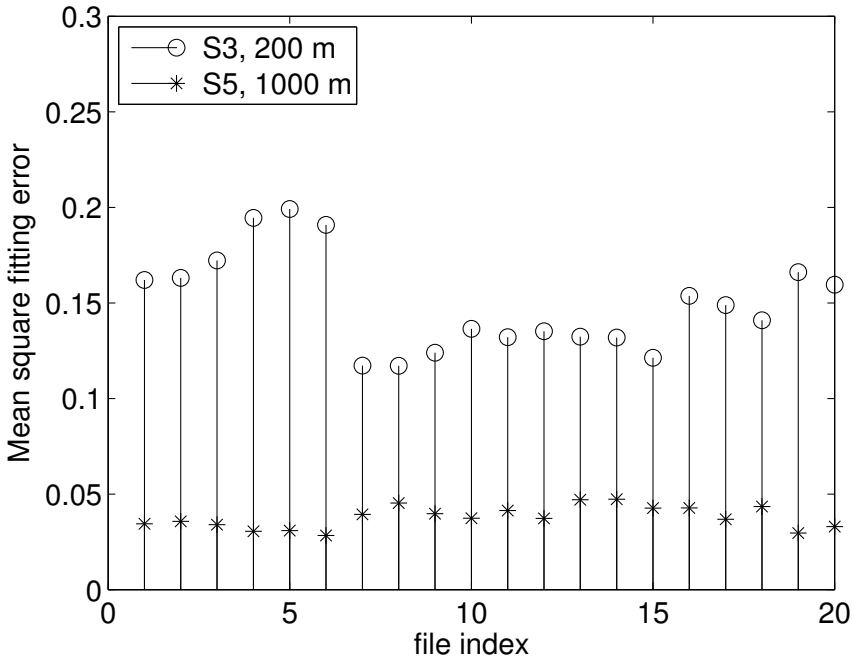

Figure 3.17. *Fitting error of the sample PDP, estimated from the data, to the exponential PDP. The smaller the error, the better the fitting of the sample PDP to the exponential model.*

Figure 3.17 shows the fitting error for the two receivers S3 and S5, respectively, over a representative subset of the SPACE08 data set. We notice that S5, which is the receiver farther away from the transmitter, fits the exponential PDP better than receiver S3. This may be due to a multiplicative loss at each water surface or bottom bounce and an exponential absorption loss of the propagation medium.

Figure 3.18 shows a typical diffuse PDP for receivers S3 and S5, respectively. We observe that receiver S5 exhibits a more diffuse channel than receiver S3, and a good fitting to the exponential model. On the other hand, for receiver S3 a clustered model, where few strong resolvable multipath components are followed by a cluster of arrivals, seems more appropriate.

Let d_{TR} be the distance between transmitter and receiver, h_T the depth of the transmitter/receiver pair below the sea level, h_B their height above the seabed, and $c \simeq 1.5\,\mathrm{km/s}$ the speed of the sound wave in the water. The line of sight component reaches the receiver with a delay $\frac{d_{TR}}{c}$. The echo reflected by the sea surface reaches the receiver with a delay $\frac{\sqrt{d_{TR}^2+4h_T^2}}{c}$, ideally assuming that the reflection occurs at distance $\frac{d_{TR}}{2}$ from the source

(a similar expression holds for the echo reflected by the seabed). Therefore, the interarrival time between the line of sight and the echo reflected by the sea surface is given by $\tau_{inter}(d_{TR}) = \frac{\sqrt{d_{TR}^2+4h_T^2}-d_{TR}}{c}$, which is a decreasing function of d_{TR}. Therefore, the further away the receiver from the transmitter, the smaller the interarrival time, the richer the interaction of the multipath components, and the more diffuse the nature exhibited by the underwater acoustic channel.

3.7.3 Numerical Results

We now present some numerical results, and we compare the mean squared prediction error of the received sequence using HSD, LS, and a purely sparse estimator, as a function of the SNR. In order to generate all the SNR values of interest, we add the underwater acoustic noise sequence $\mathbf{w}^{(i)}$, scaled by a factor $\sqrt{S}^{-1} > 0$, to the received sequence $\mathbf{y}^{(i)}$ in the estimation phase, so as to induce SNR dependent channel estimation errors. Letting $\hat{\mathbf{h}}^{(i)}$ be the ith channel estimate, estimated from the noisy received sequence $\mathbf{y}^{(i)} + \sqrt{S}^{-1}\mathbf{w}^{(i)}$, $\mathbf{y}^{(i+1)}$ be the observed sequence that we want to predict, and $\mathbf{X}^{(i+1)}$ be the Toeplitz matrix associated with the corresponding pilot sequence, the MSE for the prediction of $\mathbf{y}^{(i+1)}$ is defined as

$$\mathbb{E}\left[\left\|\mathbf{y}^{(i+1)} - \mathbf{X}^{(i+1)}\hat{\mathbf{h}}^{(i)}\right\|_2^2\right], \tag{3.28}$$

where the expectation is computed with respect to the realizations of the noise (intrinsic noise in the experimental data set and additional noise $\mathbf{w}^{(i)}$) and of the channel. The overall mean squared prediction error is computed by averaging the sample squared error term $\left\|\mathbf{y}^{(i+1)} - \mathbf{X}^{(i+1)}\hat{\mathbf{h}}^{(i)}\right\|_2^2$ over the sub-sequence index i, and over multiple received sequences, each $60\,\mathrm{s}$ long, collected over different times and environmental conditions.

For the HSD model, we consider the G-Thres estimator, with $\alpha = \ln\left(\frac{1-\tilde{q}}{\tilde{q}}\right)$, $\tilde{q} = 0.001$.

We consider two different cases for the estimate of the PDP of the diffuse component: the sample PDP estimate, averaged over $N_{ch} = 1878$ subsequent channel realizations, corresponding to a temporal window of $56\,\mathrm{s}$; and the exponential PDP model, based on only one channel realization. In the latter case, we employ the Expectation-Maximization (EM) algorithm [37] developed in [1], which exploits the HSD structure of the channel to jointly estimate the sparse and diffuse components, and the power β and decay rate ω of the exponential PDP of the diffuse component. One realization of the channel is sufficient in this

case, due to the structure of the PDP which makes it possible to average the fading over the delay dimension, rather than over subsequent channel realizations.

As to the purely sparse case, we employ the G-Thres estimator assuming no diffuse component, to allow a fair comparison with the HSD model. This estimator, due to its thresholding operation, generates a sparse channel structure.

Figures 3.19 and 3.20 show the mean squared prediction error for receivers S3 and S5 for the G-Thres estimator, respectively. In particular, the labels "G-Thres data" and "G-Thres model" refer to the G-Thres estimators using the sample estimate of the PDP of the diffuse component and the exponential PDP model, respectively.

We notice that both the G-Thres and the sparse estimators perform better than LS, as observed in [18, 19, 21] for other sparse estimators. Moreover, in the low SNR region the G-Thres and the purely sparse estimators achieve the same prediction error. In fact, in this region, the diffuse component $\mathbf{h}_d$ is below the noise floor, and cannot thus be distinguished from the noise. Therefore, an accurate estimate of $\mathbf{h}_d$ is not possible in this regime, and the HSD model does not bring any advantage over a purely sparse one. On the other hand, in the high SNR region all the estimators converge to the prediction error of LS. This can be explained with the fact that, when the noise level is negligible compared to the signal level, the prior knowledge about the channel structure provides no useful information. Moreover, the prediction error floor for high SNR is the result of intrinsic noise in the experimental data set, and of channel perturbations over subsequent observation intervals (notice that the prediction error floor is different for receivers S3 and S5, due to the fact that they incur different noise levels and rate of channel variations).

The G-Thres estimators outperform the purely sparse estimator in the medium SNR range. In fact, although based on a simplified model of the diffuse and the sparse components, they are able to capture further diffuse structure of the underwater acoustic channel, which is discarded by a purely sparse estimator.

Comparing the two G-Thres estimators (with sample PDP estimate of the diffuse component and exponential PDP model), we observe that the best prediction accuracy is achieved by the G-Thres estimator with the sample estimate of the PDP. However, the G-Thres estimator based on the exponential model for the PDP performs very close to this lower bound, although some performance loss can be observed in the medium SNR range, due to a non

perfect fitting of the data to the model.

Notice that a similar behavior of the estimators can be observed for receivers S3 and S5, despite the fact that receiver S3 exhibits a sparser channel structure than receiver S5. We conclude that the G-Thres estimator is robust, and achieves good estimation accuracy even in channels which do not exhibit a diffuse nature.

Finally, in Figures 3.21 and 3.22 we plot the outputs of the G-Thres estimator, with the estimate of the sparse and diffuse components, for a channel realization at receivers S3 and S5, respectively, and for the high and medium SNR regimes. We notice that only one specular component is detected at receiver S5 at high SNR. In fact, receiver S5 exhibits a more diffuse channel, and a good fitting to the exponential PDP model, as discussed in Section 3.7.2. On the other hand, a larger number of sparse components are detected at receiver S3, which exhibits a sparser structure (Figure 3.18).

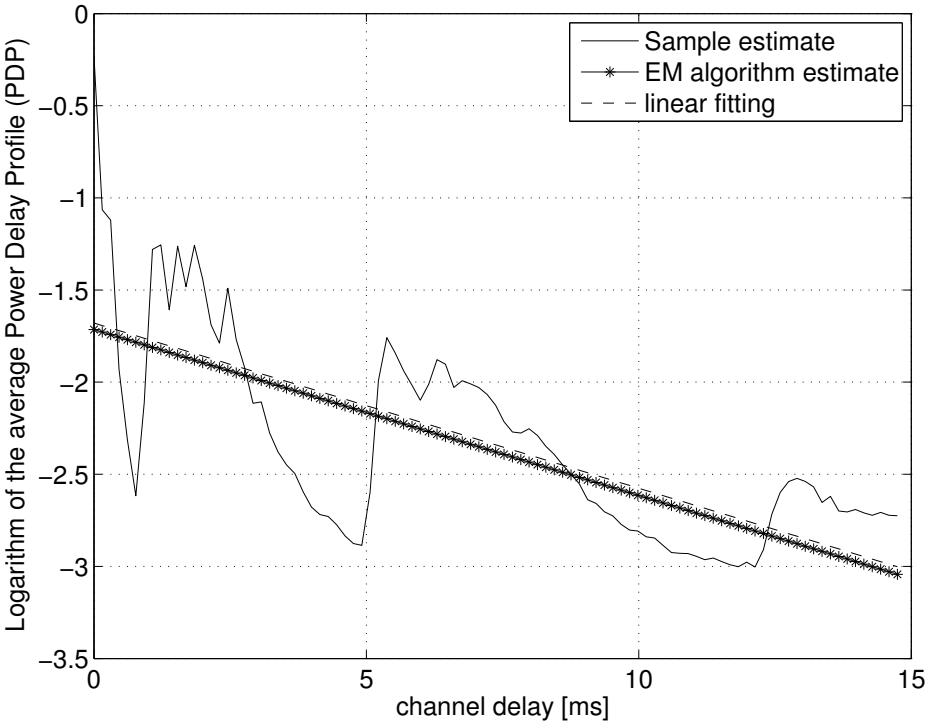

(a) Receiver S3

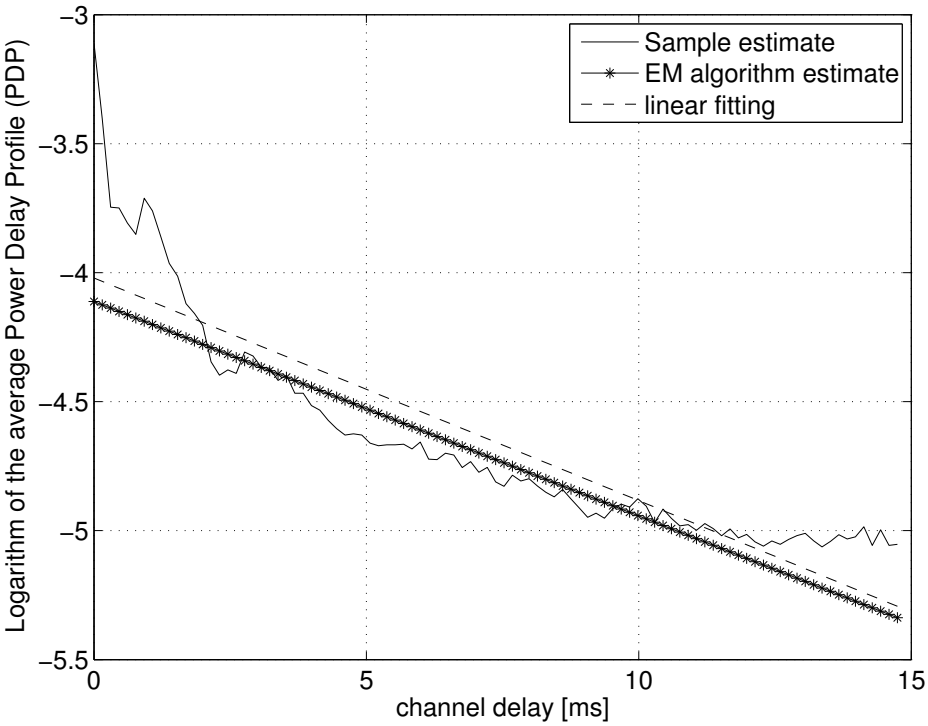

(b) Receiver S5

Figure 3.18. *A typical sample PDP for receivers S3 and S5, with the exponential PDP estimated by linear fitting, and the PDP estimate based on the EM algorithm [1].*

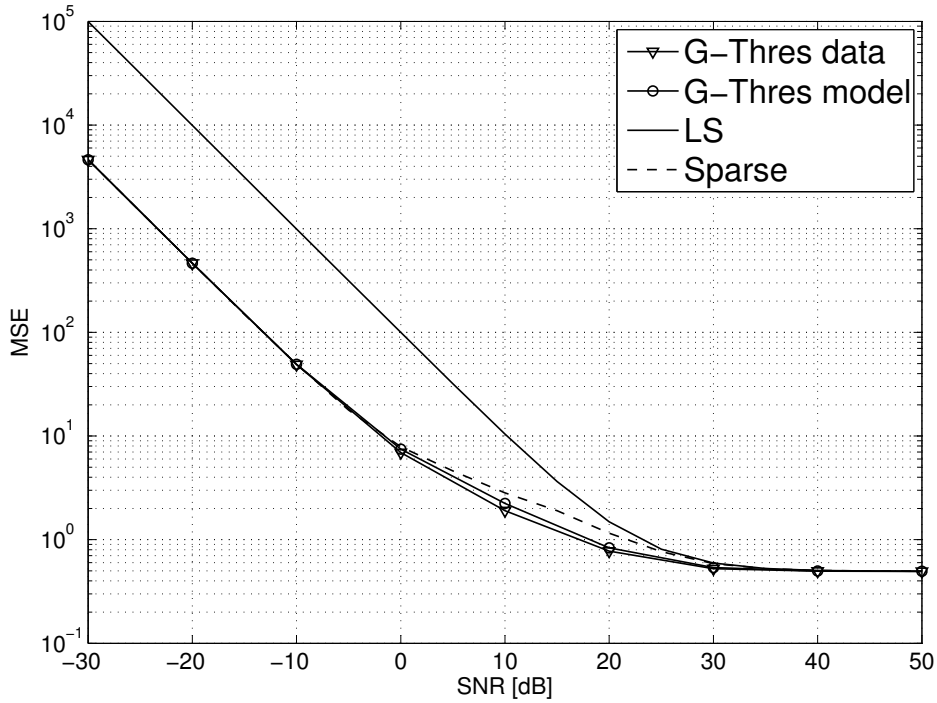

(a) Entire SNR range

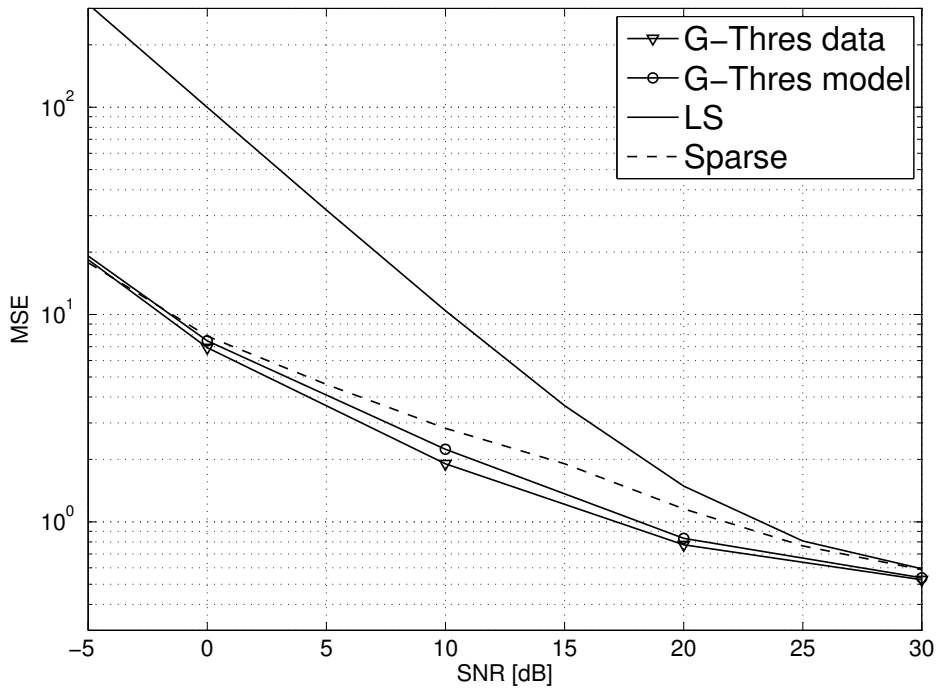

(b) Zoom in medium SNR range

Figure 3.19. *Mean square prediction error of the observed sequence for receiver S3, G-Thres estimator.*

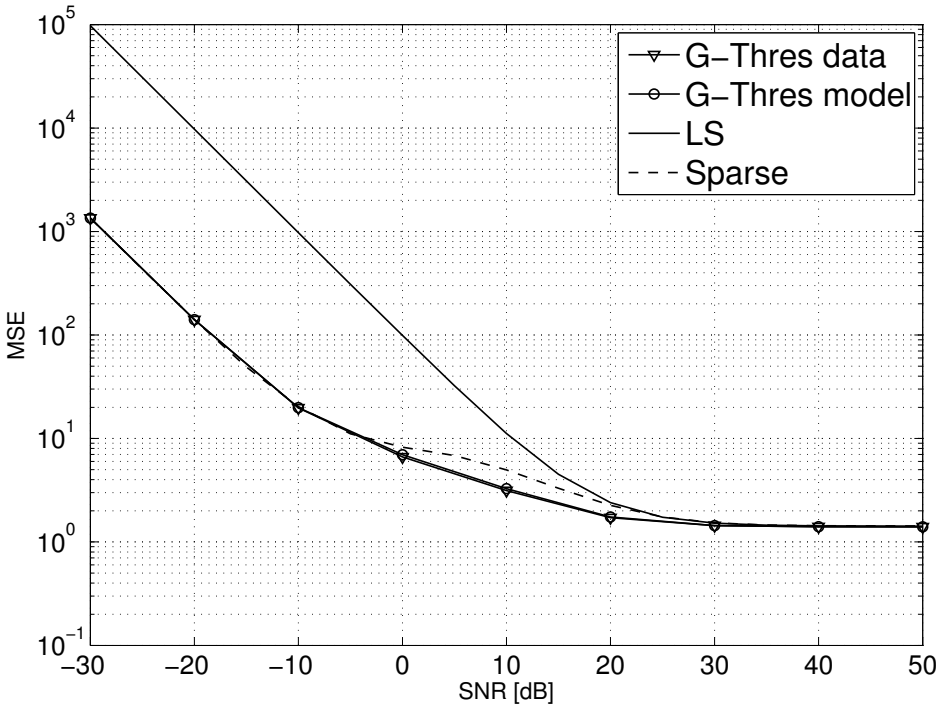

(a) Entire SNR range

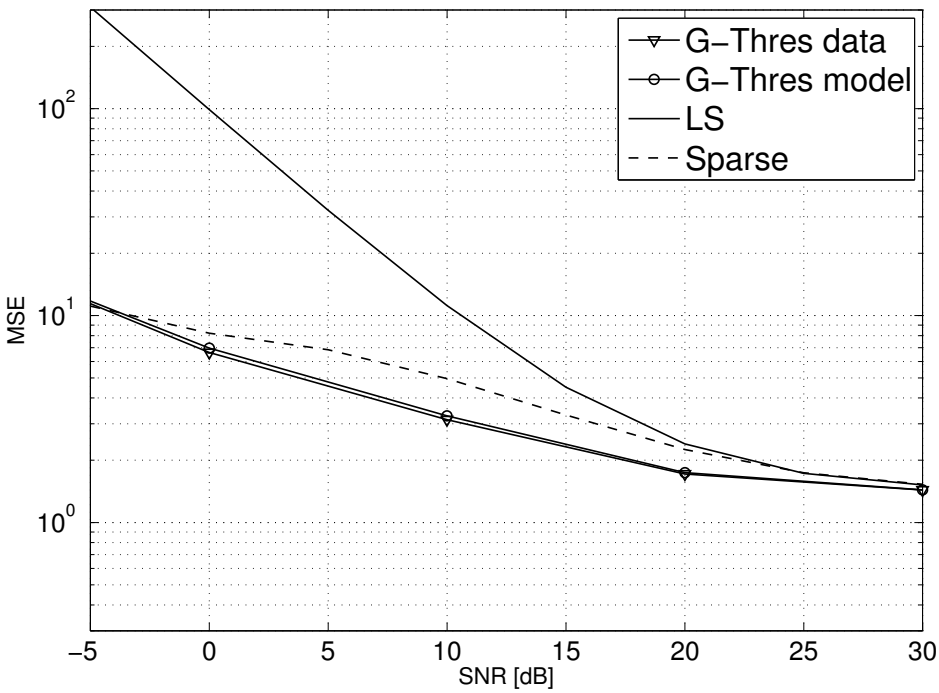

(b) Zoom in medium SNR range

Figure 3.20. *Mean square prediction error of the observed sequence for receiver S5, G-Thres estimator.*

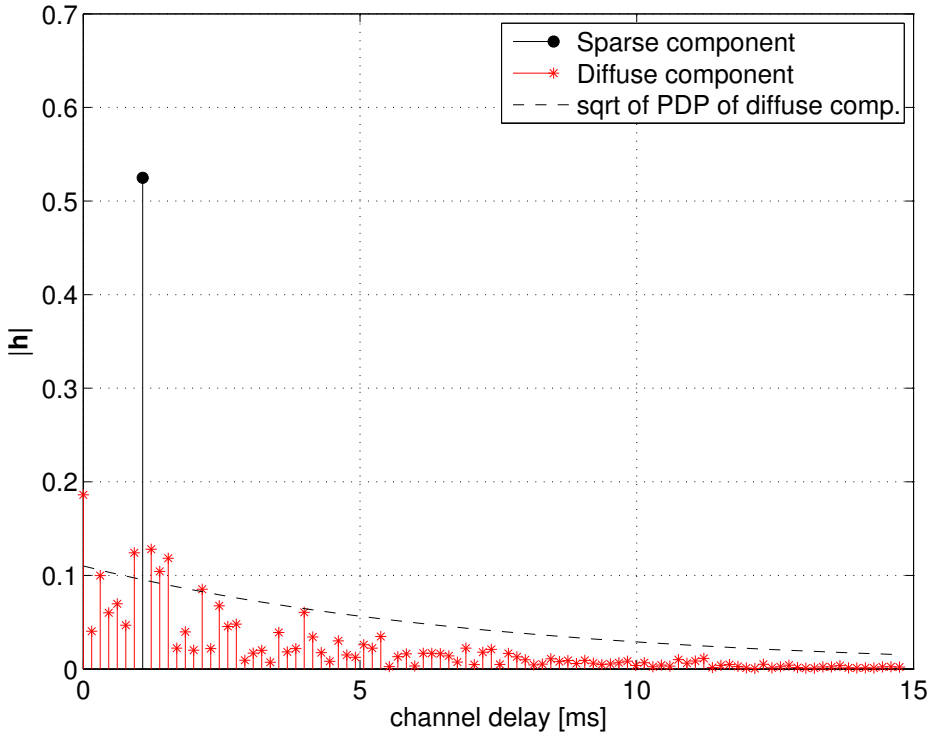

(a) SNR=10dB

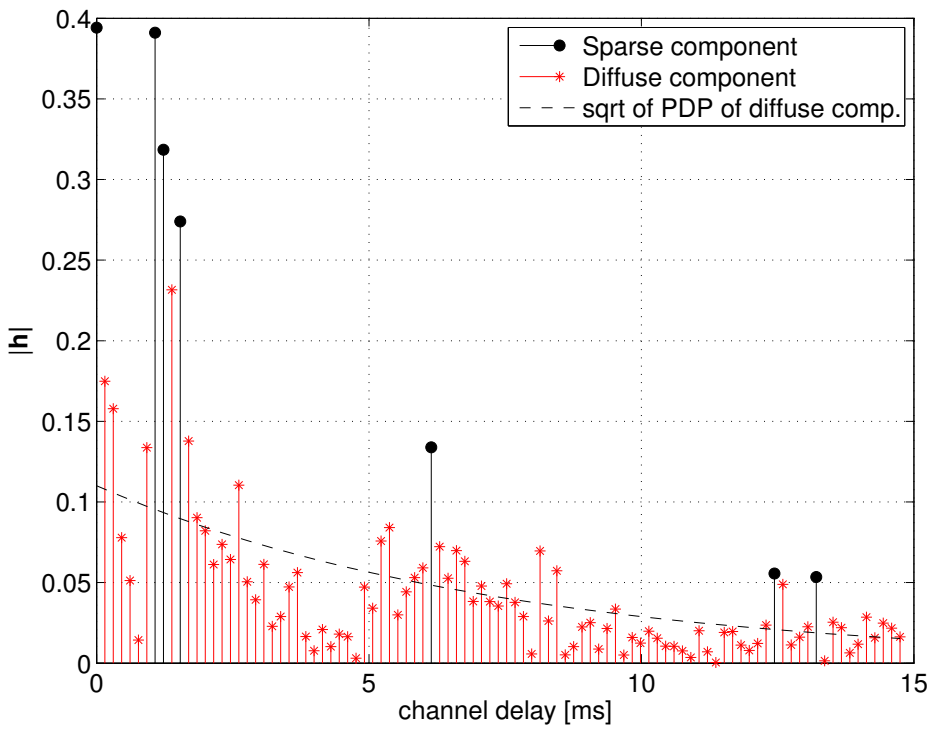

(b) SNR=50dB

Figure 3.21. *G-Thres estimator, estimated sparse and diffuse components for receiver S3.*

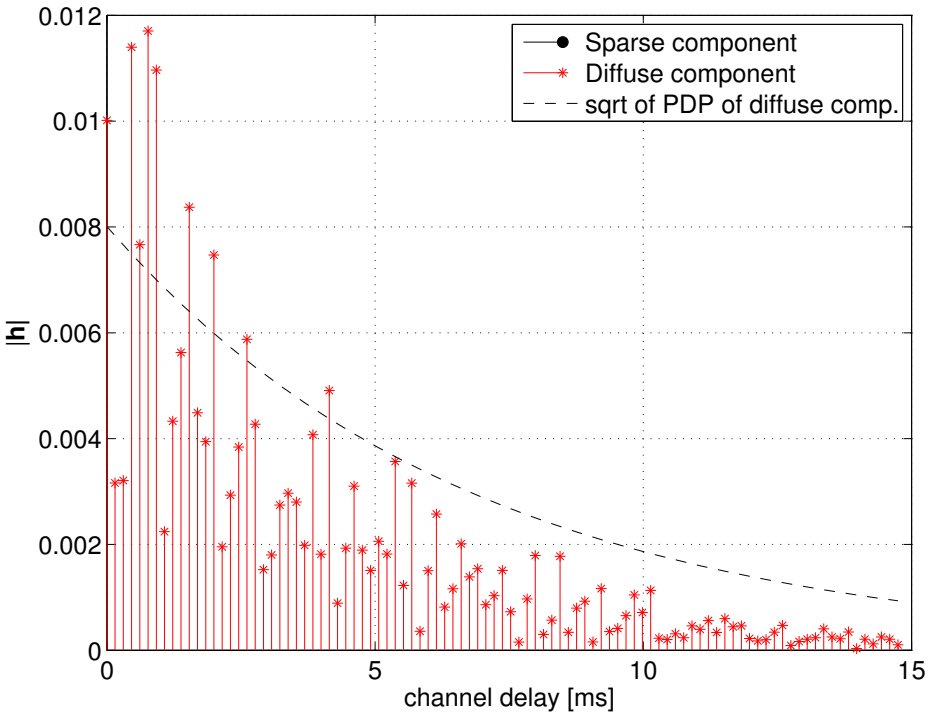

(a) SNR=10dB

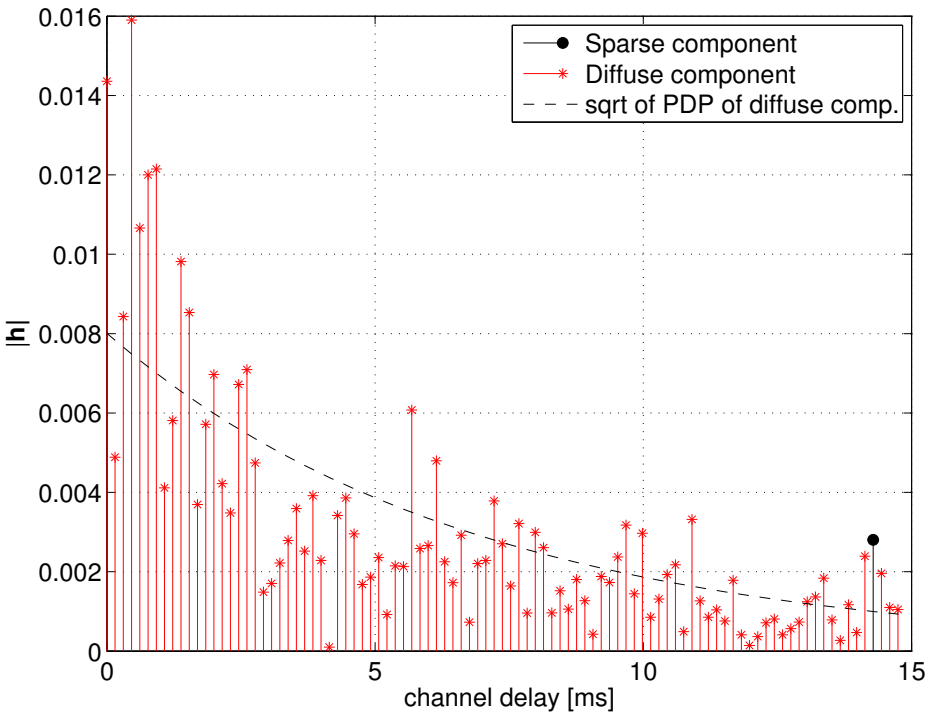

(b) SNR=50dB

Figure 3.22. *G-Thres estimator, estimated sparse and diffuse components for receiver S5.*

Chapter 4

Adaptive Communications Schemes and Model Validation

4.1 Chapter Overview

This Chapter is devoted to presenting analytical and simulation results on the performance of two adaptive communications schemes, namely HARQ and AM, proposed to mitigate the effects of the time-varying channel conditions. As observed in the previous chapter, the communications performance heavily varies with time. For this reason, we also evaluate and validate statistical models for HARQ and AM techniques.

More specifically, we present a comparative study between the performance obtained via simulation and those computed by analytical models, thus validating the proposed models. Results show that these models, which have been proposed for terrestrial wireless communications, are good candidates for representing the average performance of the aforementioned techniques also in the underwater acoustic scenario.

4.2 Motivations and Related Work

We perform these studies in order to fill the gap between modeling and technological development of underwater acoustic communications systems. In particular, to the authors' knowledge, the characterization of the packet error process cannot be found in the litera-

ture, and techniques such as HARQ or adaptive modulation have spurred the interest of the community only recently.

First, we study the packet error process and its statistics, since it affects the performance of all the upper layers protocols, thus representing a key metric in assessing the design and performance of network protocols. We discuss the suitability of Markov models for representing the temporal evolution of the realizations of the packet error process. This study aims at defining an accurate model for the PER process, to be used in networks simulators, and to provide insight on the type of assumptions that can be made about the statistics of the PER in further studies. Given the lack of extensive data, it is hard to find contributions about this aspect for the underwater acoustic case, whereas this approach and models are broadly accepted for terrestrial wireless communications.

Second, we investigate the problem of reliable underwater communications, which require, possibly more than other traditionally lossy channels such as the terrestrial radio or the satellite channel, the employment of effective error control. The two basic techniques over time-varying channels are FEC, which is based on the use of error-correction codes without any retransmission, and pure ARQ, which adopts retransmissions without coding. In this study, we considered a combined approach, so as to realize what is usually referred to as a HARQ scheme [38]. This solution, if properly designed, is able to combine the best of both techniques, namely to protect the data sent with error correcting codes already from the first transmission, yet allowing retransmissions if needed; this spares the need for introducing unnecessarily high amounts of redundancy in the codeword, which would be inefficient in underwater channels. The rationale is to find a suitable technique for counteracting the time-variability of the channel conditions. In fact, the problem of channel code design arises when dealing with applications for underwater networks, requiring reliability. Nevertheless, the underwater channel often causes heavy loss of information and high error correlation. We believe that a deep understanding of HARQ techniques over the acoustic channel is necessary in order to properly model the performance of the applications of interest. In the literature, Markov chains are generally recognized as a useful means to represent wireless channels and analytically characterize techniques such as ARQ / HARQ operating on top of them [39, 40]. Many papers evaluate the performance of ARQ or HARQ over a Markov channel: for example, the authors of [41] analyze HARQ schemes representing a

fading channel through a Markov chain, whereas in [42] the delay statistics of HARQ are evaluated when both the arrivals and the channel error process are Markov. The approach considered here is different from these related works, since we aim at identifying whether a Markov representation may be appropriate for the underwater acoustic channel, when HARQ is used on top of it, and in this case how the parameters of the Markov chain should be set.

Finally, we consider AM techniques, which tune the constellation size of the used modulation, depending on the available information about the channel state, e.g., as perceived by the transmitter or as fed back by the receiver. The purpose of AM is two-fold: to achieve higher spectral efficiency (by using more efficient modulations whenever the channel so allows) and to reduce the chance of outage events (by avoiding the use of complex schemes when the channel cannot support them). While AM is a well established technique for link adaptation in terrestrial radio networks [43–46], it has received comparatively much less attention in underwater acoustic networks. However, a few works do propose the use of AM. In particular, [47] focuses on variable-rate Mary Frequency-Shift Keying (FSK) modulations, where the proper rate is chosen based on a preliminary exchange of control packets for SNR estimation. Adaptive modulation and coding has also been analyzed in [48], where the authors post-process data collected during the AUVfest 2007 campaign. A transmit array of 10 elements and a receive array of 8 elements were deployed in the Gulf of Mexico; different modulation (from BPSK to multi-level PSK) and turbo coding rates (from $7/8$ down to $1/3$) were employed to modulate the subcarriers of a multitone transmit signal in both a Single-Input Single-Output (SISO) and a Multiple-Input Multiple-Output (MIMO) configuration. The overlooking of AM can be at least partially explained by the difficulty of implementing such schemes in real-time systems today. However, the next generations of underwater devices will be likely able to support real-time variable-rate modulation. Here, we assume that the channel SNR process is updated once for every received packet, and that the corresponding SNR value is fed back to the transmitter so that the adaptation of the modulation scheme can be performed prior to the subsequent transmission. As we will detail in the following, the transmissions of our dataset are sufficiently spaced to make a per-packet modulation update process feasible. However, in order to simulate a less ideal case where greater delay affects the feedback from the receiver, we also consider the availability of only

outdated channel estimates. In any event, the system considers instantaneous (instead of average) SNR samples to be fed back to the transmitter. Starting from SNR traces, we discuss their fitting using Rayleigh as well as Nakagami-m distributions, and use the models to obtain the performance of simple BPSK as well as more complex Mary quadrature amplitude modulation (M-QAM) schemes with square constellation. We note that perfect Channel State Information (CSI) at the transmitter is assumed here: given that the only information required to run the AM scheme is the SNR of the current transmission, this assumption is reasonable.

4.3 Analysis of SNR and packet error rate

This section is devoted to the analysis of the PER measured during SubNet09, we call *experiment A* and *experiment B*, the experiments carried out on May 30 and August 30, respectively. We start by analyzing PER as a function of SNR for the JANUS waveforms being considered. The correctness of the packet is inferred through a CRC check at the receiver after standard processing, i.e., detection of signal probe, reconstruction of the hopping pattern, non-coherent detection of BFSK symbols, de-interleaving and soft Viterbi decoding of the PHY-level convolutional code. Fig. 4.1 plots PER against SNR for all experiments listed in the previous subsection, for all transmitter-receiver links. The figure has been obtained by considering SNR bins of size $0.5\,\mathrm{dB}$ and by calculating the relative frequency of packet errors for all packets whose SNR falls in the same bin. Different markers and colors correspond to different transmitters. Fig. 4.1 also includes a linear regression fitting the relationship between PER and SNR expressed in dBs, i.e.,

$$\mathrm{PER} = \alpha \cdot \mathrm{SNR} + \beta. \tag{4.1}$$

A negative-slope line adequately fits data in this case, in accordance to the approximate performance of incoherent BFSK detection in the high SNR regime and in the presence of frequency-flat fading (recall that the frequency hopping pattern is designed to help escape multipath). Fig. 4.1 suggests that the closest link (i.e., from T3, in green) yields different performance with respect to the links from T1 and T2: this is due to the harsher multipath footprint, whereby secondary paths yield significant power with respect to the main arrival path. As a consequence, the line that fits only the outcomes from T3 (light grey) has lower

Table 4.1. *Coefficients of PER fitting lines.*

TX nodes	Slope (α)	Intercept (β)	MSE (same TX)	MSE (all TX)
T1+T2	-0.035	0.775	0.0101	0.0164
T1+T2+T3	-0.026	0.676	0.0136	0.0136
T3	-0.019	0.580	0.0095	0.0197

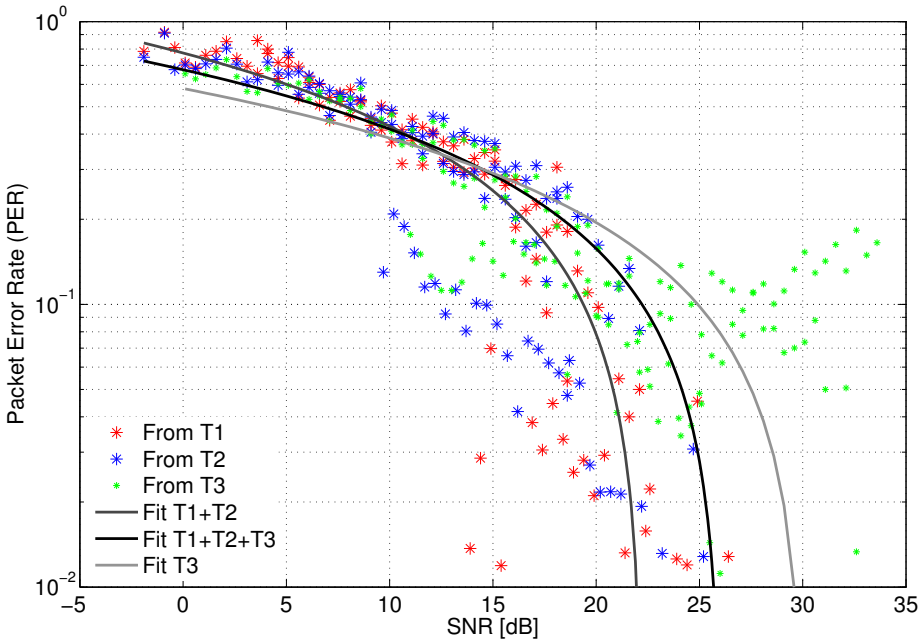

Figure 4.1. *Log-scale scatterplot of PER as a function of SNR for varying transmitter and all receivers. Linear fits of the joint scatterplot of all transmitters as compared to the joint scatterplot of T1 and T2, as well as the scatterplot of T3, are also provided.*

slope than the other lines. Depending on the required degree of accuracy, one may decide to use the T1+T2+T3 fit, which considers data from all transmitters while providing an acceptably higher MSE with respect to the MSE of the linear fit of T3 points (see Table 4.1).

As a first approximation, we may incorporate fitted PER curves into a simulator so as to reproduce the PER for matching modulation and receiver processing and in similar environments as the shallow summer waters of Pianosa. However, we would still need to factor in the correlation among SNR values, including those experienced between the same fixed transmitter and receiver: assuming uncorrelated SNR realizations may actually be too strong an assumption. This is exemplified in Figs. 4.2 and 4.4, which show the SNR time series for the signals transmitted by T2 during experiments A and B, respectively, as received

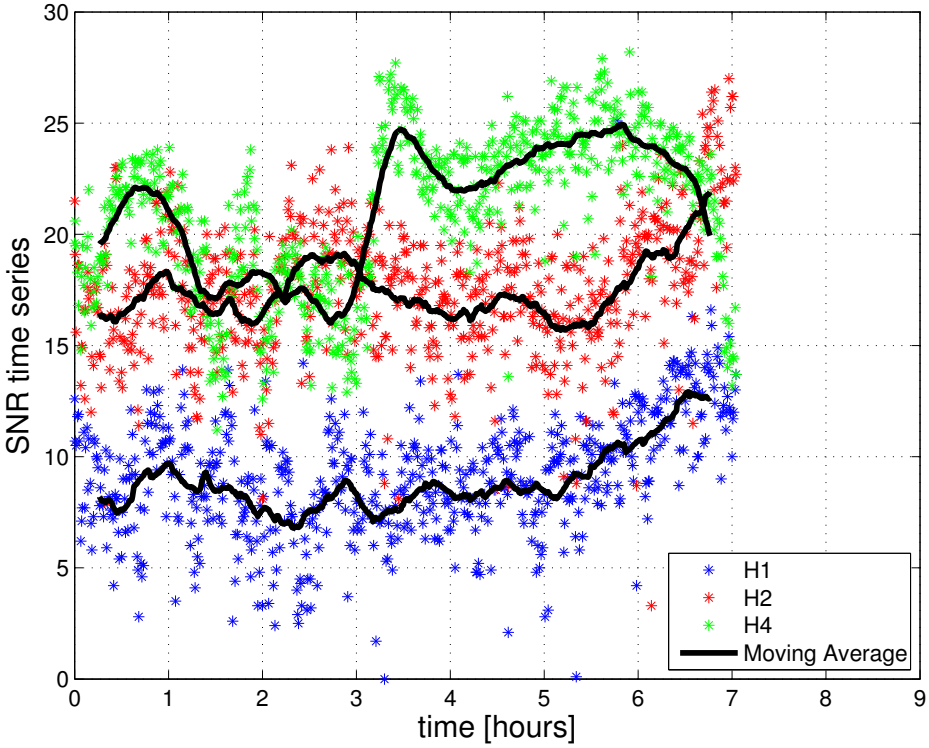

Figure 4.2. *Time series of SNR for transmissions from T2 during experiment A. Moving averages over 50 samples are provided as a solid black line.*

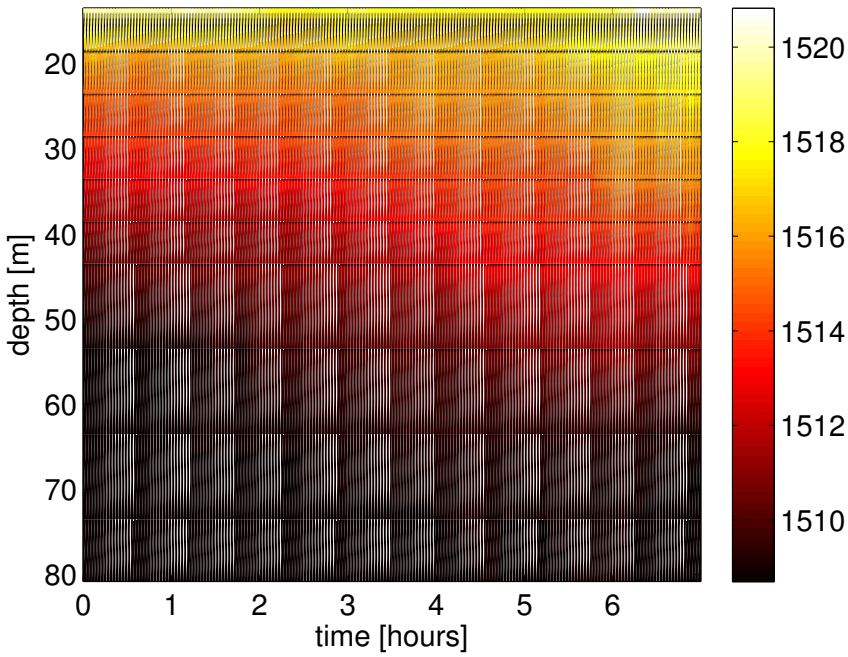

Figure 4.3. *Sound speed profile [* m/s*] at different depths as a function of time during experiment A.*

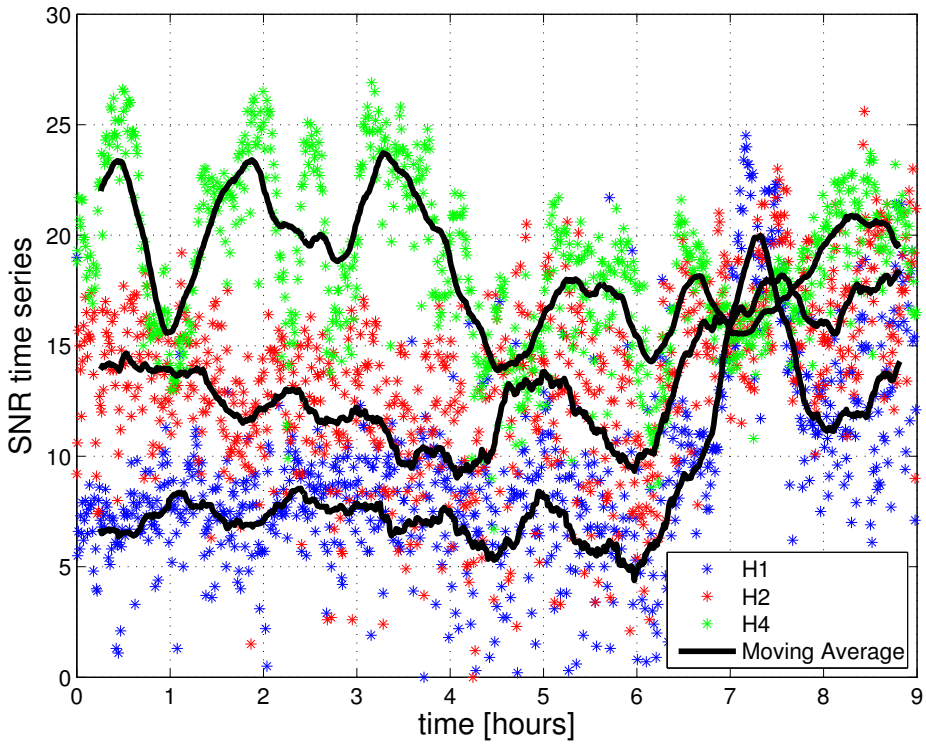

Figure 4.4. *Time series of SNR for transmissions from T2 during experiment B. Moving averages over 50 samples are provided as a solid black line.*

by all hydrophones of the VA. For better clarity, a moving average over 50 samples of the trace is also shown as a black solid line. The figures show that some links are quite stable throughout the duration of the experiment, whereas others experience greater instability. For instance, the link T2–H1 in Fig. 4.2 is stable almost throughout the whole experiment, with the exception of a slight increase towards the end, as we will explain later. The same applies to the T2–H2 link as well. On the contrary, the link T2–H1 in Fig. 4.4 remains stable around an average SNR of 7 dB for roughly 6 hours, then experiences an abrupt improvement as its SNR increases to more than 20 dB, before falling back to roughly 13 dB. Similar observations apply to the T2–H2 link as well. Some oscillations of up to 10 dB in the value of SNR over the T2–H4 link can be observed in both figures; however it should be noted that the SNR remains very high, hence oscillations are not expected to have a significant impact on PER. We will elaborate on this point in the following section.

The most significant variations on the SNR in Figs. 4.2 and 4.4 cannot be ascribed to noise, because different hydrophones of the VA are differently affected. To give at least a partial explanation, we must therefore observe the time series of the sound speed at different

depths (SSP) in the water column close to the VA.[1] Fig. 4.3 reports the sound speed samples taken every two minutes for the whole duration of experiment A. We observe a sound speed increase in the upper water layers from 6 to 7 hours after the beginning of the experiment; this changes the way acoustic waves are refracted, and in this case allows more power to be bent toward hydrophones closer to the surface (H1 and H2). For the same reason the SNR over the T2–H4 link decreases (H4 is the deepest hydrophone). Unfortunately, due to thermistor chain down time, we cannot display a similar plot for experiment B.

The variations of the average SNR over macroscopic time scales discussed above motivates us to analyze whether such variations can be profitably tracked through synthetic models such as Markov models (MMs) and Hidden Markov Model (HMM)s, which incorporate memory of past events. The following section is devoted to the discussion of their applicability to the proposed scenario.

4.4 Markov models

To keep track of channel memory, we consider three different models: a 2-state Markov channel, which keeps memory of one previous event (MM1); an extension of the same model bearing a memory of 2 previous events and resulting in a 4-state channel (we will refer to this model as MM2), and a 2-state HMM. The accuracy of these models is then compared to an IID error model and to real channel traces.[2] To evaluate the accuracy of the models, we consider the predicted average error probability ε, the probability mass function (pmf) of the length of an error burst (i.e., the probability $p_b(k)$ that the number b of consecutive errors (i.e., an error burst) is equal to k) and the m-step error correlation (i.e., the probability $\xi_{n,m} = \mathbb{P}[\text{packet } n+m \text{ erroneous}|\text{packet } n \text{ erroneous}]$). We choose these metrics because i) the average error probability ε is the primary check for the correctness of an estimated model; ii) an accurate approximation of the pmf of error bursts is important to assess the

[1] We recall that the testbed deployment included a thermistor chain, which is used to indirectly measure sound speed at different depths by virtue of the Mackenzie formula [49] and by assuming that water salinity does not vary significantly throughout the summer season.

[2] The MM1 model was also considered in a comparative study [50] focused on N-states Markov channel models, where however the number of states tracks changes in the SNR level instead of providing explicit memory of past error events; in addition, we note that the study in [50] considers an iso-velocity medium and trains models using simulated channel traces instead of field measurements.

impact of the model on network protocols, other than being tightly related to the chosen model (e.g., a 2-state Markov model exhibits a geometric burst length pmf [51]); finally iii) second-order statistics such as the m-step error correlation $\xi_{n,m}$ have a significant impact on network protocols and may lead to design guidelines (e.g., protocols should not insist on transmitting over a channel whose errors are still highly correlated for high m).

4.4.1 2-state Markov model (MM1)

This model is characterized by two states, labeled 0 and 1, where 0 represents a correct packet reception event. The model is trained by estimating the transition probabilities of the matrix

$$\mathbf{P}_2 = \begin{pmatrix} p_{00} & p_{01} \\ p_{10} & p_{11} \end{pmatrix}, \tag{4.2}$$

which regulates the transition between correct and wrong receptions, and where the subscript 2 refers to the number of states. Let us call $\boldsymbol{\pi} = [\pi_0 \ \pi_1]$ the vector containing the steady-state distribution of the Markov chain, i.e., the solution to the system of equations $\pi_j = \sum_i \pi_i p_{ij}$ under the constraint that $\sum_i \pi_i = 1$. In this case, the error probability is $\varepsilon_2 = \pi_1 = p_{01}/(p_{01} + p_{10})$; moreover, we have $p_b(k) = p_{11}^{k-1} p_{10}$, and $\xi_{n,m} = p_{1,1}^{(m)}$, where $p_{1,1}^{(m)}$ is the element in position $(1, 1)$ of the m-step transition matrix, $\mathbf{P}^m$.

4.4.2 4-state Markov model with memory of two past events (MM2)

This model expands the 2-state model by explicitly incorporating further memory of past events within states. Four states are defined, i.e., (00), (01), (10) and (11), where 0 and 1 represents again a correct and a wrong packet reception; the transition probabilities between these states are thus arranged into a 4×4 matrix $\mathbf{P}_4$, with elements of the kind $p_{(k-1\ k),(k\ k+1)}$, where the event with index k is in common between the pair before and after the transition. In this case, the average probability of error is $\varepsilon = \pi_{01} + \pi_{11}$; the pmf of the burst length is found by considering the evolution of the Markov process from the only state leading to errors after a successful packet reception, i.e., state (10):

$$p_b(k) = \begin{cases} p_{01,10} & k = 1 \\ p_{01,11} p_{11,11}^{k-2} p_{11,10} & k \geq 2 \end{cases} \tag{4.3}$$

Similarly, $\xi_{n,m}$ is found as

$$\xi_{n,m} = \frac{\pi_{01}\left(p^{(m)}_{01,01} + p^{(m)}_{01,11}\right) + \pi_{11}\left(p^{(m)}_{11,01} + p^{(m)}_{11,11}\right)}{\pi_{01} + \pi_{11}}. \tag{4.4}$$

4.4.3 2-state hidden Markov model

HMMs assume that a non-observable state structure lies beneath observed values for a certain random process [52]. In this case, we observe erroneous or correct packet reception, and make the assumption that the probability of such events actually depends on the (hidden) state of the channel. As in the hidden Gilbert-Elliot model [53, 54], the state may represent a different level of goodness of the channel, corresponding to a different probability of receiving a packet correctly.

HMMs can be described in terms of a transition probability matrix $\mathbf{P}_H$ (whose structure is the same as $\mathbf{P}_2$ in this case); furthermore, by defining $\phi_i(j)$ as the probability that event j is observed in state i, we can define the following diagonal observation probability matrices

$$\mathbf{C} = \begin{pmatrix} \phi_0(0) & 0 \\ 0 & \phi_1(0) \end{pmatrix} \quad \mathbf{E} = \begin{pmatrix} \phi_0(1) & 0 \\ 0 & \phi_1(1) \end{pmatrix}, \tag{4.5}$$

which respectively model correct (matrix $\mathbf{C}$) and erroneous (matrix $\mathbf{E}$) packet reception in either state [51, 52]. Since the state of the chain is hidden, all statistics must be averaged through the stationary distribution of the underlying Markov process.

Therefore, the average probability of error is $\varepsilon = \boldsymbol{\pi}\mathbf{E}\,\mathbf{e}$, where $\mathbf{e} = [1\ 1]^T$, and we recall that $\boldsymbol{\pi}$ is the steady-state probability distribution vector of the hidden Markov chain. In addition, we remark that the matrix products $\mathbf{P}_H\mathbf{E}$ and $\mathbf{P}_H\mathbf{C}$ yield the joint probability of making a transition and observing an erroneous or correct packet, respectively, *after* the transition has been completed. The burst length probability distribution can be found in accordance to the previous definitions:

$$p_b(k) = \frac{\boldsymbol{\pi}\mathbf{C}(\mathbf{P}_H\mathbf{E})^k\mathbf{P}_H\mathbf{C}\,\mathbf{e}}{\boldsymbol{\pi}\mathbf{C}\mathbf{P}_H\mathbf{E}\,\mathbf{e}} \tag{4.6}$$

The conditional probability $\xi_{n,m}$ is found by considering k-step spaced error events, by averaging over the probability of being initially in state 0 or 1, and by conditioning on the event that an error was in fact observed on the initial state, i.e.,

$$\xi_{n,m} = \frac{\boldsymbol{\pi}\mathbf{E}\mathbf{P}_H^m\mathbf{E}\,\mathbf{e}}{\boldsymbol{\pi}\mathbf{E}\,\mathbf{e}}, \tag{4.7}$$

where we note that both terms of the fraction are scalar.

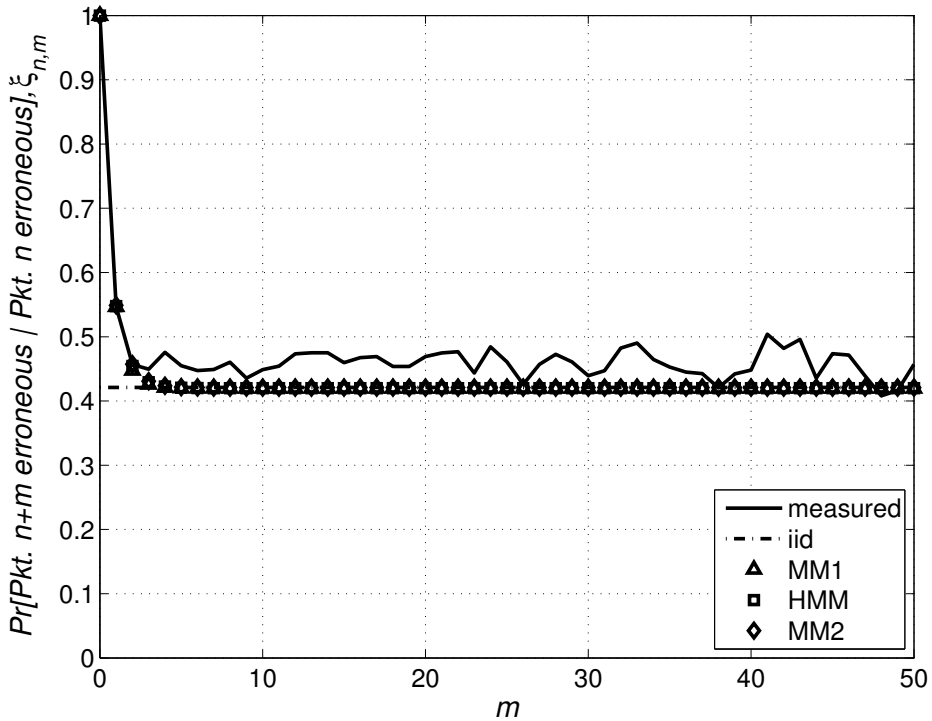

Figure 4.5. *m-step error correlation. Link T2–H1, experiment A.*

4.4.4 Comparison among Markov Models and Channel Traces

We begin by comparing the average probability of successful packet reception, $1 - \varepsilon$, as predicted by the models and as measured from data traces. This test is a basic check that the models are correct; however, it is worth noting that a simple slotted Stop-and-Wait Automatic Repeat reQuest (ARQ) protocol, would exhibit a throughput of $1-\varepsilon$, normalized to the round-trip time. The results of the evaluation are reported in Table 4.2 and show good accordance with measurements.

Consider now the k-step error correlation $\xi_{n,m}$ defined in Section 4.4. Figs. from 4.5 to 4.10 show this metric for the links between T2 and all hydrophones during experiments A and B, respectively. The figures compare $\xi_{n,m}$ as predicted by all models against the probability of having an erroneous packet using an IID model and against measured traces. The pictures suggest that non-hidden models perfectly reproduce short-term correlation (i.e., where their inherent memory of past errors allows a correct representation of the channel behavior); however, they converge very quickly to their stationary behavior, as indicated by the fact that predicted error correlation quickly reaches the IID floor; on the contrary, the

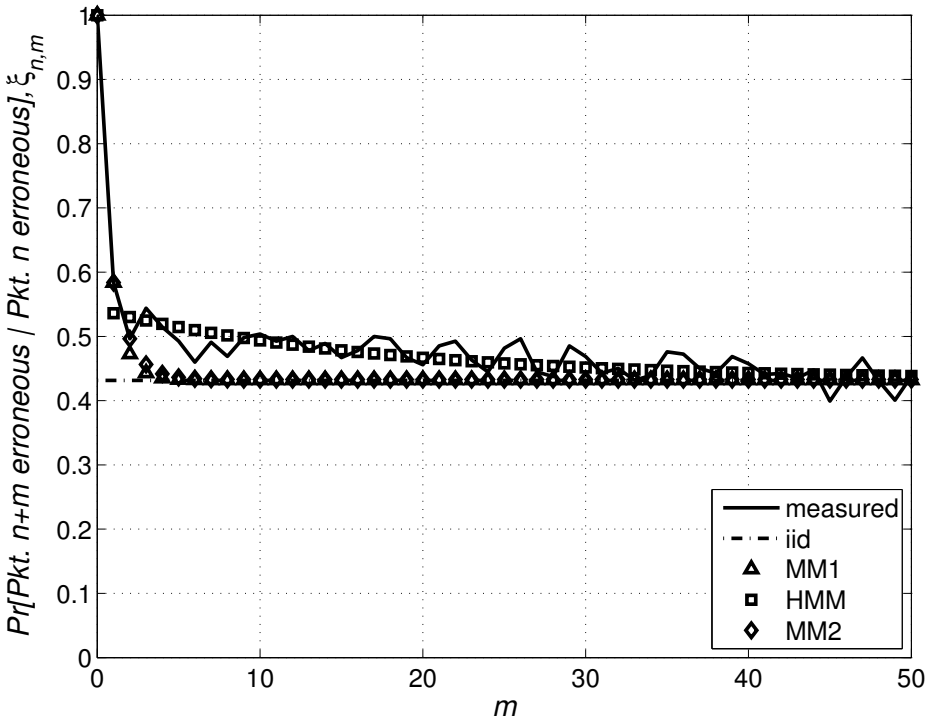

Figure 4.6. *m-step error correlation. Link T2–H2, experiment A.*

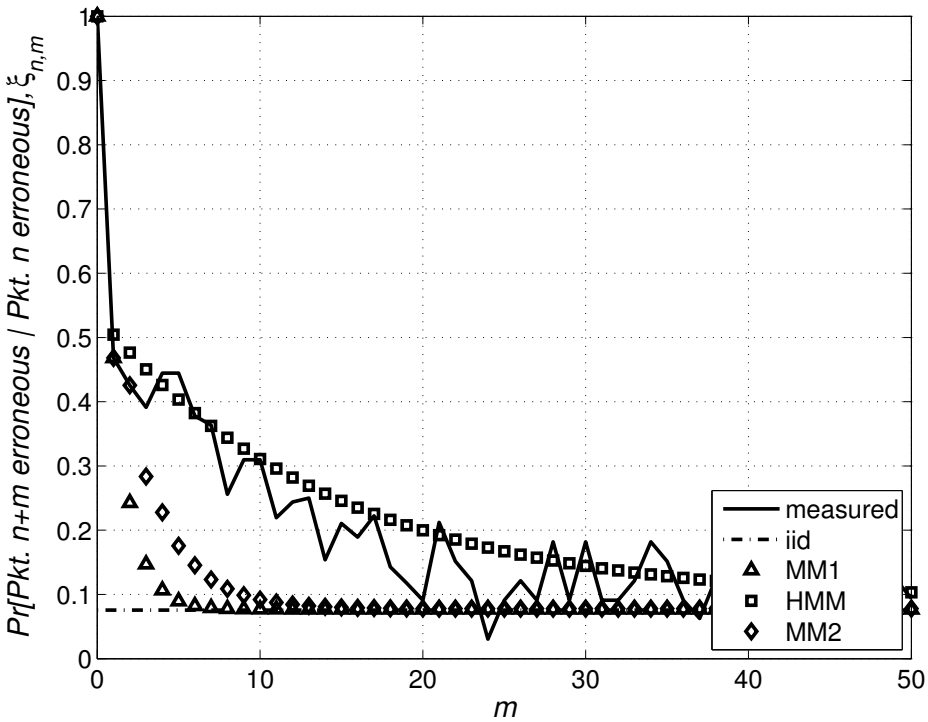

Figure 4.7. *m-step error correlation. Link T2–H4, experiment A.*

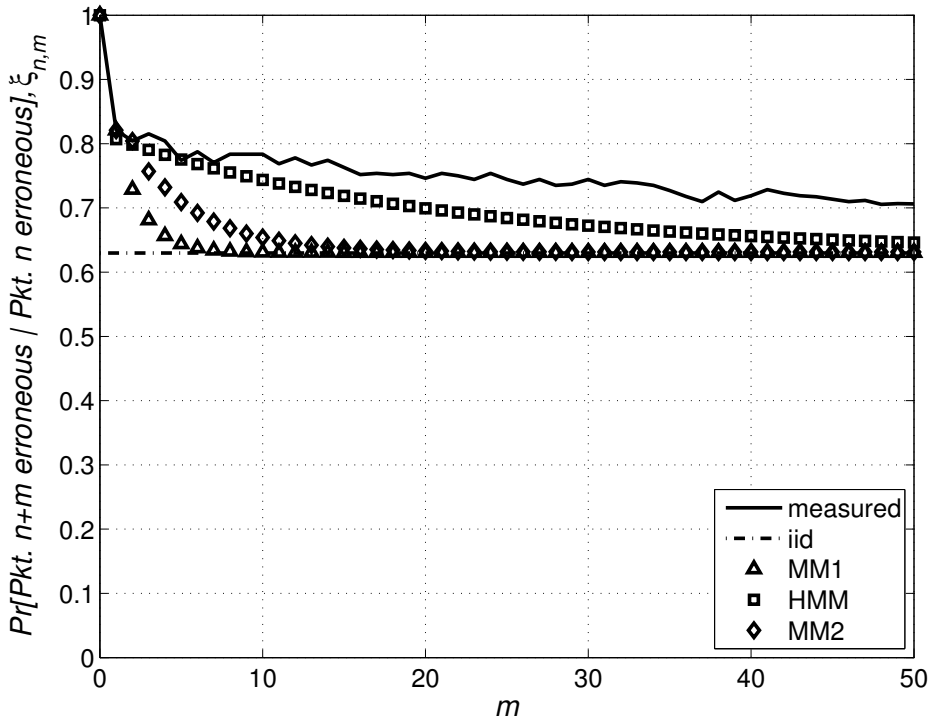

Figure 4.8. *m-step error correlation. Link T2–H1, experiment B.*

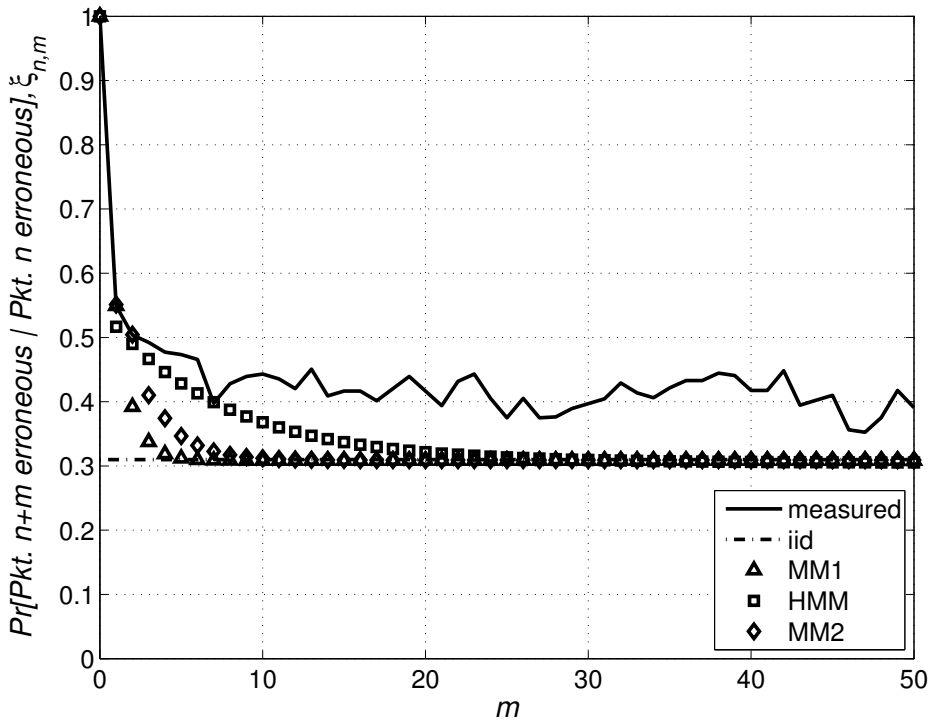

Figure 4.9. *m-step error correlation. Link T2–H2, experiment B.*

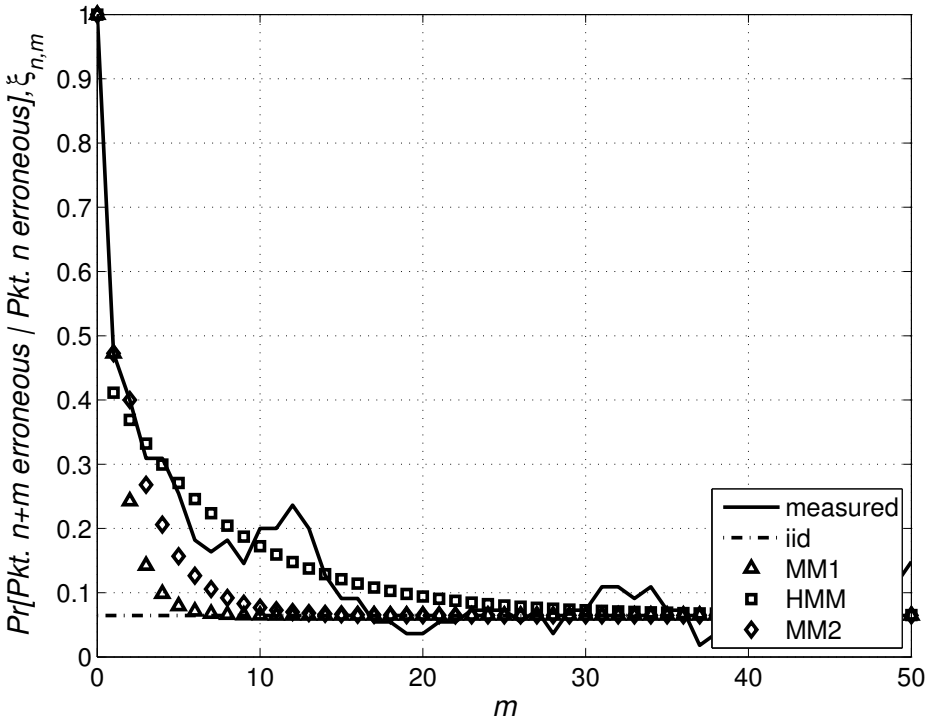

Figure 4.10. *m-step error correlation. Link T2–H4, experiment B.*

HMM achieves a much better reproduction of long-term error correlation, at the price of only a slight approximation of short-term correlation.

By comparing the results from Figs. 4.5 to 4.10 to those in Figs. 4.2 and 4.4, we can note that channel traces are not always representative of a hidden model. For example, the T1–H1 and T2–H2 links in Fig. 4.2 are quite stable even on a long time scale, and can be successfully modeled by non-hidden approaches as well. Conversely, such links as T2–H4 in Fig. 4.2 as well as all links in Fig. 4.4 exhibit much larger oscillations, which an HMM is expected to capture more effectively. Figs. 4.7 and 4.8– 4.10 confirm this intuition by showing that HMMs adhere better to measured error correlation values on the long term. Indeed, while in some cases HMMs also converge to the IID floor faster than measured data (e.g., Figs. 4.8 and 4.9), they do so slower than non-hidden models do.

The goodness of HMMs is also suggested by the observation of the pmf of the length of an error burst, $p_b(k)$. We focus again on transmitter T2 and on experiments A and B, whose results are reported from Figs. 4.11 to 4.16. These figures compare $p_b(k)$ as predicted by the models against the pdf estimated from real data (represented by red star-shaped markers). The figures show that in general the best approximation of data is yielded by MM2, followed

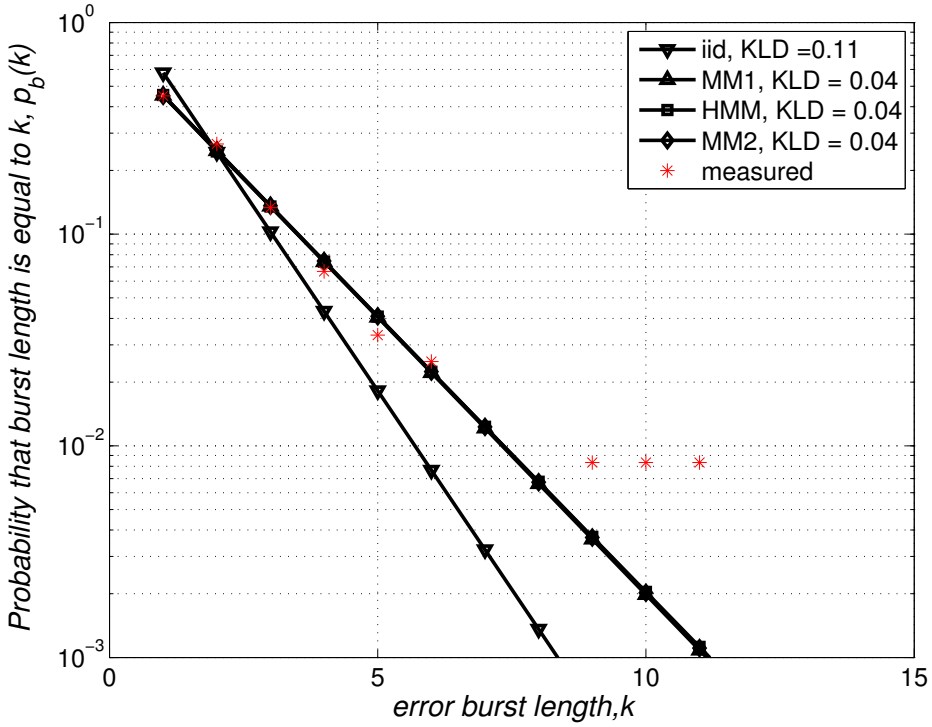

Figure 4.11. *Probability of observing k consecutive errors. Link T2–H1, experiment A.*

by HMM and MM1, with occasionally similar performance on some of the links. To further support this assertion, we have reported in the legend of each picture the Kullback-Leibler divergence (KLD) of predicted pmfs from the pmf estimated from data traces. In almost all cases the divergence is smaller for the MM2 and HMM models than for the MM1 and IID models, with the exception of Fig. 4.12, where the KLD of the HMM slightly exceeds that of non-hidden models. Along with the satisfactory approximation of long-term error correlation, this suggests that HMM models are good candidates for a synthetic model of acoustic channels. We remark that we have focused only on transmissions from T2 in experiments A and B, but these results are representative of all other experiments and links, which would allow to draw the same conclusions.

4.5 Performance of the Hybrid ARQ technique

4.5.1 Channel Model

For the present discussion, we consider transmissions subject to an HARQ error control mechanism described as follows. Nodes transmit information frames, where each frame is

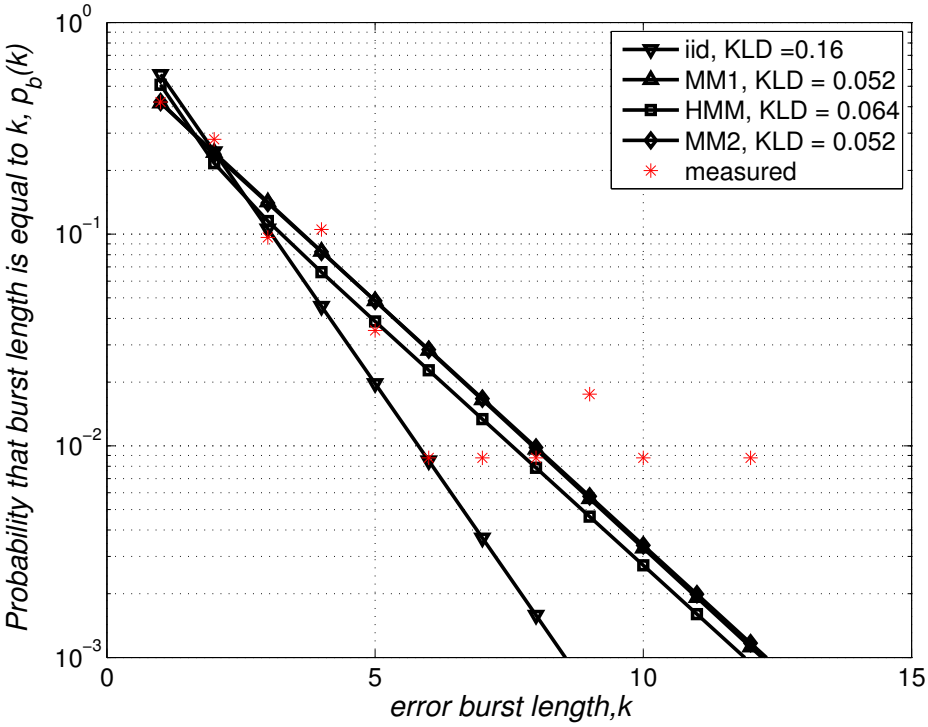

Figure 4.12. *Probability of observing k consecutive errors. Link T2–H2, experiment A.*

actually derived from a long codeword of a low-rate code. Each frame is composed of multiple HARQ packets, or fragments, which for simplicity are assumed to be all of the same size. In addition, we assume that each fragment, if correctly received, is sufficient to recover the whole codeword. Every time a packet is sent, the receiver replies with a feedback Acknowledgment (ACK) or Not Acknowledgment (NACK) message, respectively indicating correct or incorrect packet reception. In the following, we will consider both Type I and Type II HARQ [55]. In Type I HARQ, only one coded fragment is sent per information frame, actually resulting in a FEC strategy to protect the frame against errors; in case a transmitter receives a NACK, it provides a retransmission of the same HARQ fragment. In Type II HARQ, instead, every information frame is associated to multiple HARQ fragments, and NACKs trigger the transmission of a new fragment each time: therefore, subsequent detection attempts are based on the availability of additional redundancy, and the corresponding scheme is usually referred to as Incremental Redundancy Hybrid Automatic Repeat reQuest (IR-HARQ).

In what follows, we will match the transmission SNR traces gathered during the SubNet09 campaign with the HARQ framework described above, by assuming that each packet

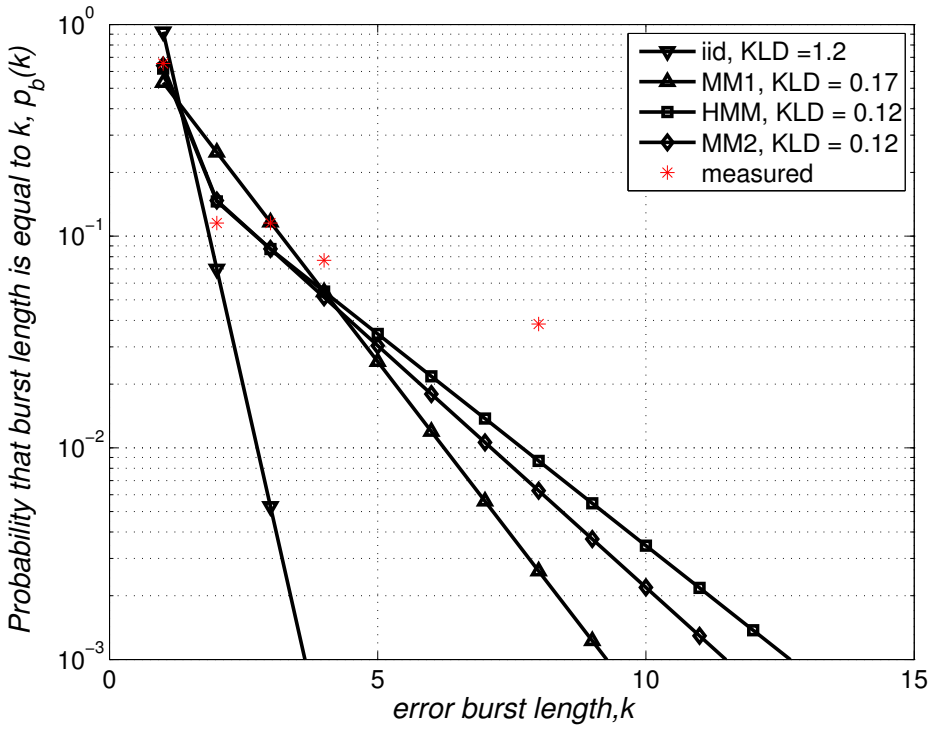

Figure 4.13. *Probability of observing k consecutive errors. Link T2–H4, experiment A.*

transmission actually carries one HARQ fragment formed by resorting to "good" Low Density Parity Check (LDPC) code ensembles such as those considered in [56]. The performance of these codes can be characterized from an information-theoretic point of view in terms of SNR thresholds: for a single transmission, a single threshold can be found that determines if decoding is immediately successful or not; for multiple transmissions, each bearing a different SNR in general, a *reliable* region can be defined as outlined in the following section [56].

The purpose of the following analysis is to determine reliable SNR regions for LDPC transmission over the links between the acoustic modems and the hydrophones. We remark that these depend on channel conditions, which in these cases are those experienced during the experiments listed at the end of the previous section. Starting from this analysis, we estimate a Markov model of the channel following the guidelines in [57] for the optimal quantization of the reliable SNR region and use the model for characterizing the performance of an IR-HARQ scheme based on the discussed LDPC code.

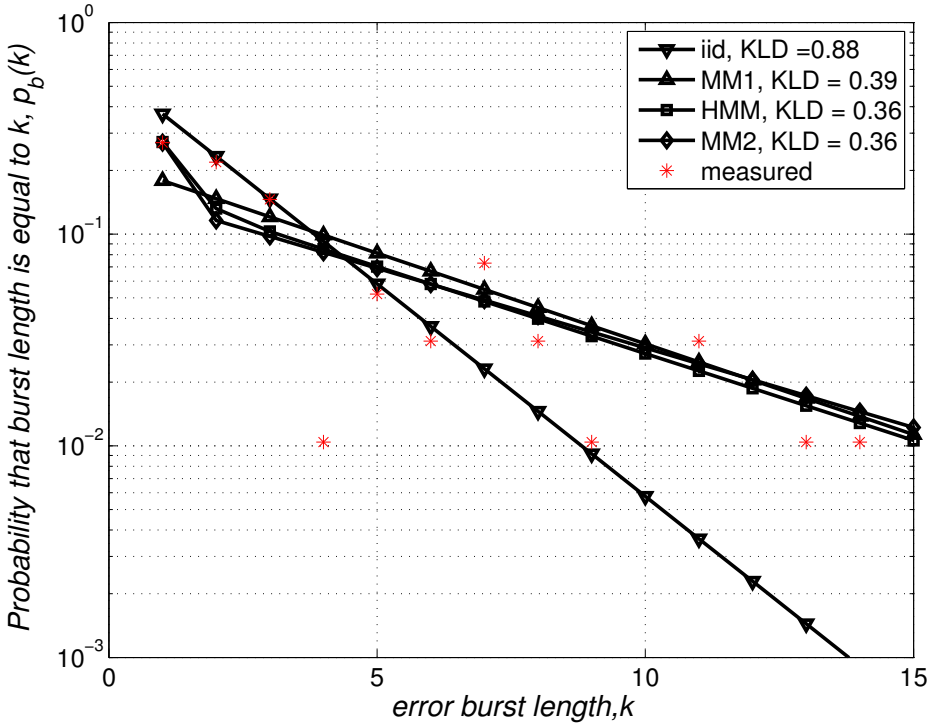

Figure 4.14. *Probability of observing k consecutive errors. Link T2–H1, experiment B.*

4.5.2 Reliable SNR regions

The reliable region model for characterizing the performance of good code ensembles [56, 58] assumes that multiple fragments are transmitted sequentially, and that at the kth transmission decoding is based on all k fragments received so far, each bearing its own SNR value $s_1, \ldots, s_k$. The reliable region $\mathcal{R}(k)$ is defined as the subset of $\mathbb{R}^k$ containing the k-tuples of SNR values for which the decoding failure probability asymptotically vanishes as the codeword length increases. Any reliable region $\mathcal{R}(k)$ has the property that if a k-tuple of SNR values $(s_1, \ldots, s_k) \in \mathcal{R}(k)$ then the k-tuple $(s_1, \ldots, s'_k) \in \mathcal{R}(k)$ as well for every $s'_k > s_k$ [56]. This directly follows from the fact that if s_k suffices to enable correct decoding, any greater s'_k would suffice as well. In turn, this makes it possible to define the reliable region using a threshold model, where the minimum value the SNR of the kth transmission should have to ensure successful decoding depends on the sequence $\mathbf{s}^{(k-1)}$ of all previous $k-1$ SNR values. Such a threshold takes the form

$$\vartheta(\mathbf{s}^{(k-1)}) = \inf\{s_k \,:\, (s_1, \ldots, s_{k-1}, s_k) \in \mathcal{R}(k)\} \tag{4.8}$$

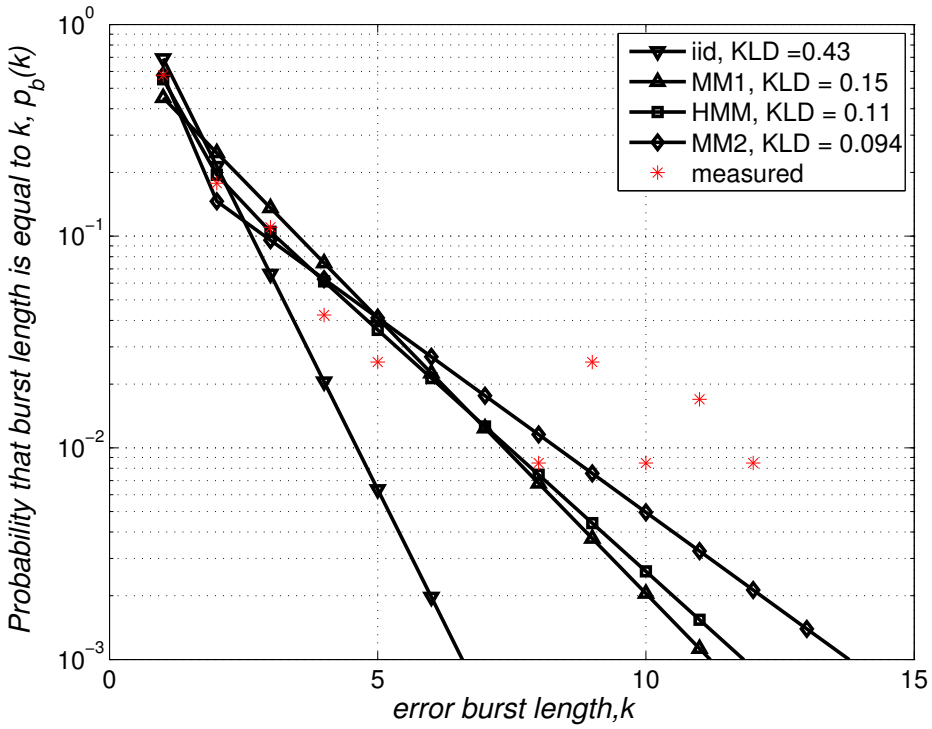

Figure 4.15. *Probability of observing k consecutive errors. Link T2–H2, experiment B.*

which can be used to verify whether correct decoding occurred at the kth transmission, i.e., by checking if $s_k \geq \vartheta(\mathbf{s}^{(k-1)})$ or not.

If the joint PDF or, equivalently, the joint distribution of the SNRs is known, the probability distribution of a given SNR k-tuple can be derived; analogously, SNR regions in $\mathbb{R}^k$ can be mapped into probability regions using the Cumulative Distribution Function (CDF) of the SNR [57]. The PDF of the SNR can be derived by fixing a link and analyzing the SNR time series over that link throughout the duration of an experiment. An example of an SNR time series is shown in Fig. 4.17, depicting the time evolution of the SNR over the links from all transmitters to hydrophone H1. A moving average of the time series taken over 25 samples is also shown as a solid black line. From the figure we see that the T3–H1 link (T3 is the closest to H1) experiences high SNR which is also quite stable over time, despite some events at the beginning of the experiment where the SNR drops 5 to $10\,\mathrm{dB}$ below its overall average value. These events are mainly due to environmental phenomena such as currents, causing temporary drops in the temperature of the upper water layers, which in turn affect how the acoustic energy propagates. We recall that H1 is placed at a depth of $20\,\mathrm{m}$, and is therefore more vulnerable to changes in superficial layer propagation parameters than other

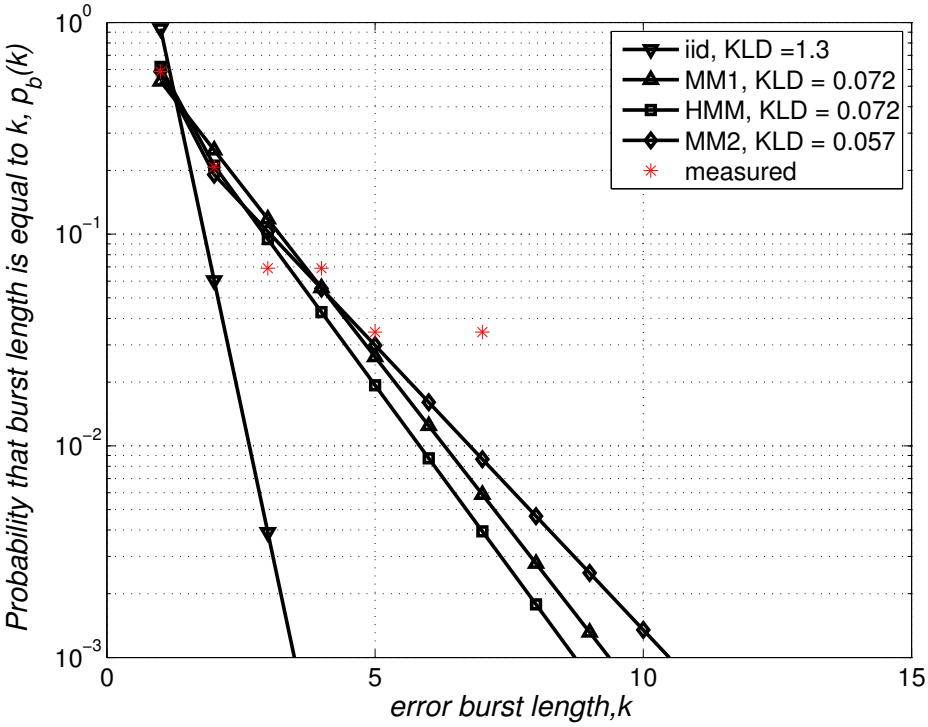

Figure 4.16. *Probability of observing k consecutive errors. Link T2–H4, experiment B.*

hydrophones. Nevertheless, the average SNR level is quite high over the T3–H1 link, as the dominating effect here is the short distance (and the consequent low attenuation) between T3 and H1. A different behavior is observed over the T1–H1 and T2–H1 links, respectively the intermediate and longest distance links. In particular the larger distance causes the variance of the SNR to increase, and makes the links more sensitive to oceanographic phenomena, as the average value of the T1–H1 SNR oscillates from roughly $5\,\mathrm{dB}$ down to $0\,\mathrm{dB}$ or less and then increases again up to $15\,\mathrm{dB}$. While a more accurate model of SNR distribution would consider the changes in the SNR average value and variance over time, it would also complicate the analysis of the system below, without yielding significantly better insight. Therefore, in the following we will take a simpler approach and estimate the statistics of the SNR as if they were stationary over the whole duration of the experiments. However, we will also validate the model by training it over a subset of the SNR traces and comparing the results to simulations carried out over a different portion of the same experiment.

In this light, Figs. 4.19, 4.20 and 4.21 show the empirical PDF of the SNR over the links from all transmitters (T1 to T3) to receiver H1 (the hydrophone placed at a depth of $20\,\mathrm{m}$).

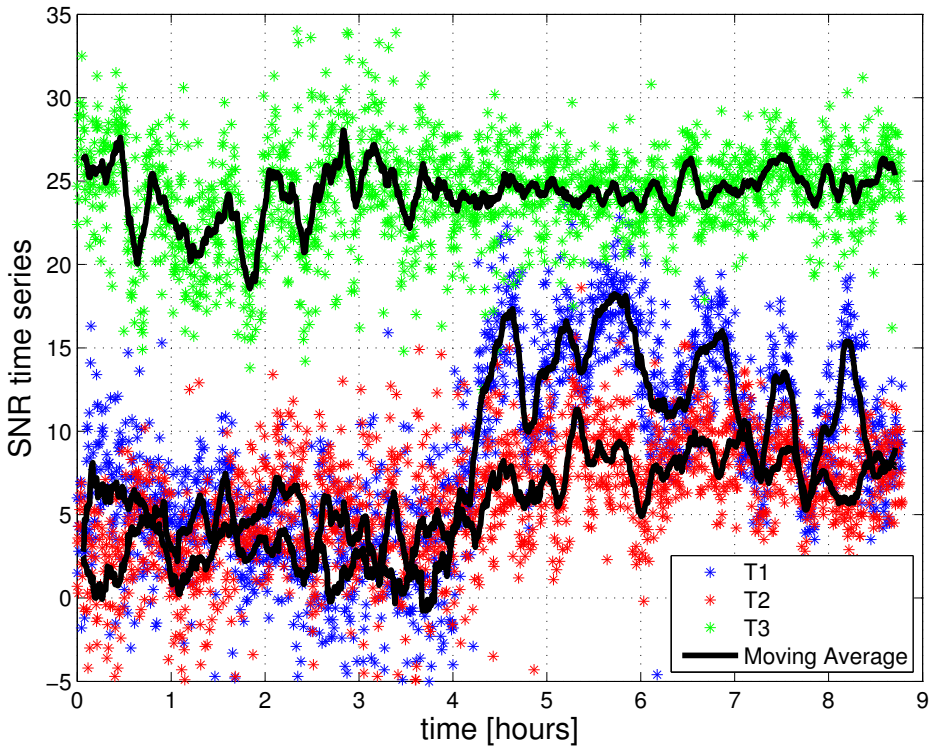

Figure 4.17. *Measured time series of the SNR over the links from all transmitters to hydrophone H1. A moving average taken over 25 samples is superimposed to the SNR time series as a solid black line.*

Each figure also shows a fit performed using a Gaussian PDF of the form

$$f_\Gamma(\gamma) = \frac{1}{\sigma\sqrt{2\pi}} \exp\left(-\frac{(\gamma-\mu)^2}{2\sigma^2}\right), \tag{4.9}$$

where the average value μ and variance σ^2 have been estimated to best fit the data in a least-squares sense; both μ and σ are reported in the legend. From (4.9), the probability that the SNR lies in any interval $[a, b]$ is then found straightforwardly as $\int_a^b f_\Gamma(\gamma)\,\mathrm{d}\gamma$. Starting from the SNR distribution, the reliable region of good LDPC code ensembles can be derived using the threshold model mentioned before and following the approach described in [56]. The reliable regions in the probability domain for links from T1, T2 and T3 to H1 are depicted in Figs. 4.22, 4.23 and 4.24, respectively, by considering two subsequent HARQ fragments. The reliable region lies to the upper right of the boundary curve shown as a solid black line; note that s_1 and s_2 represent the values taken by the cumulative distribution functions of the SNR of the first and second transmissions, respectively. Note that the reliable region is larger when the SNR distribution has higher average and lower variance. In particular, due to the very high average SNR experienced by the T3–H1 link, the reliable region tends to

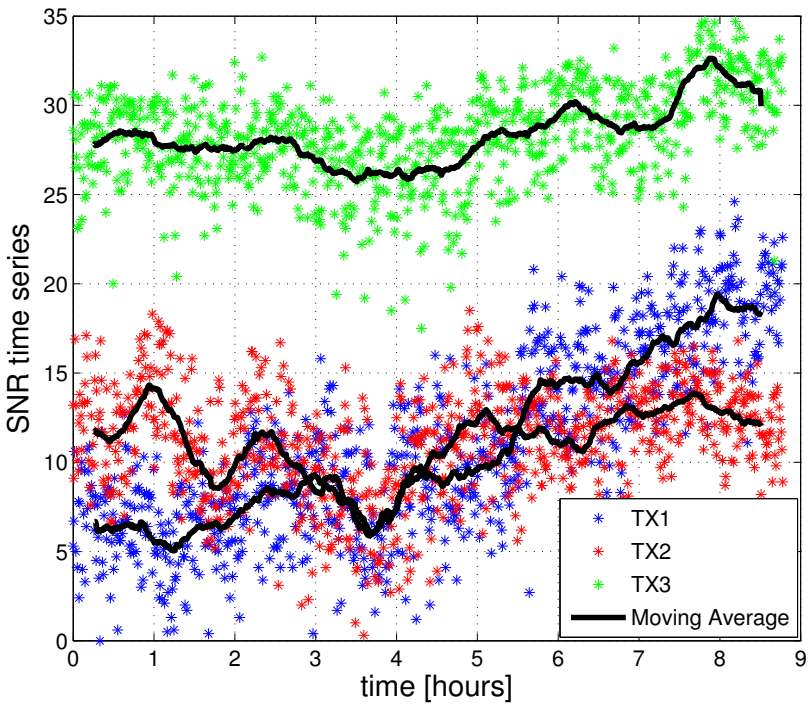

Figure 4.18. *Time series of the SNR over the links from all transmitters to hydrophone H2 throughout experiment A. A moving average of the time series taken over 25 samples is superimposed to the SNR scatterplot as a solid black line.*

occupy the whole space, and the unreliable region correspondingly collapses into the $(0, 0)$ point.

Figs. 4.22 to 4.24 refer to a specific experiment, and to a single receiver, but are representative of all other experiments and links between T1–T3 and the hydrophones: in fact, a generally good accordance between the SNR pdf and a proper Gaussian fit (albeit with different μ and σ for different experiments and links) was found to hold in all cases.

On top of the reliable region model, we construct a channel model following the guidelines for channel state quantization described in [57]. The procedure is briefly summarized in the following. Before channel quantization, a vector of channel states has the form $\mathbf{s}^{(k)}$, as defined above, where each element can take infinitely many values in $\mathbb{R}$. Quantizing channel states translates $\mathbf{s}^{(k)}$ into a k-tuple of discrete values, that evolve according to a Finite-State Markov Chain (FSMC). If N thresholds $\alpha_1, \ldots, \alpha_N$ divide $\mathbb{R}$ into $N+1$ intervals $I_0, \ldots, I_N$, where $I_j = [\alpha_j, \alpha_{j+1}[$, and we define $\alpha_0 = 0$ and $\alpha_{N+1} = +\infty$, any real value

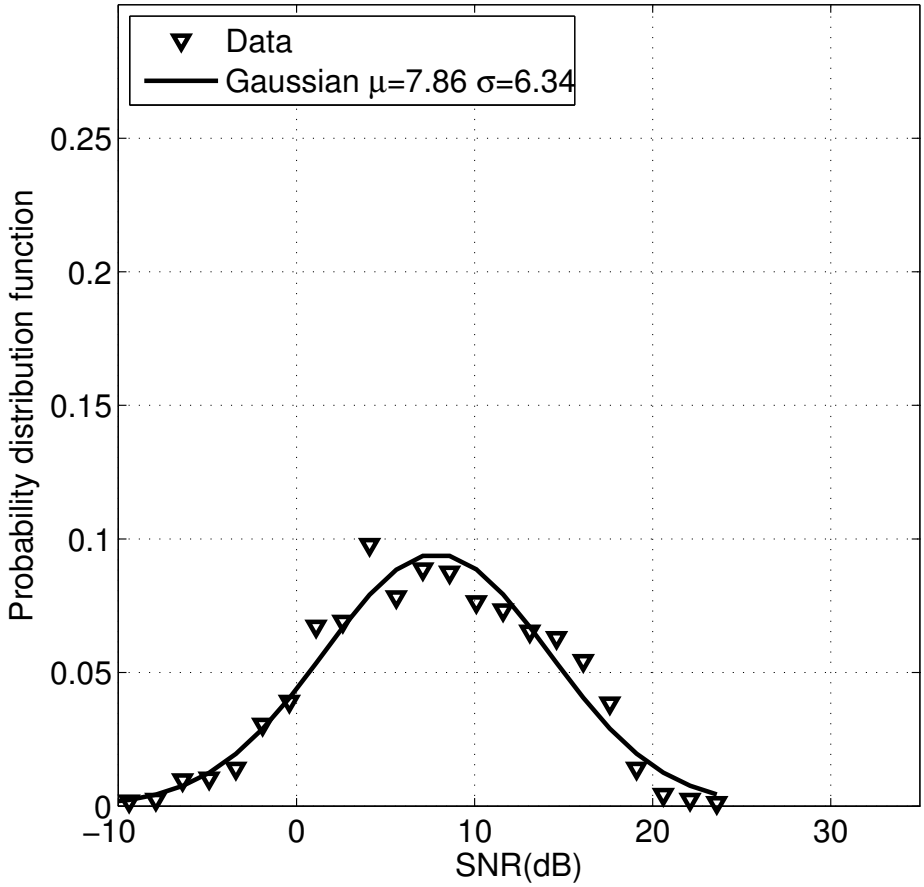

Figure 4.19. *Empirical PDF of the SNR and Gaussian fit over the T1–H1 link.*

becomes mapped into the discrete index j of the interval I_j it falls within. To formalize this mapping, define $d(s_k)$ as the function returning the interval of $\mathbb{R}$ where s_k is contained, i.e., $d(s_k) = j$ if $s_k \in I_j$. Now, by grouping the mappings for all elements of an SNR k-tuple $\mathbf{s}^{(k)}$ into a vector, we can write $\mathbf{d}^{(k)} = (d(s_1), \ldots, d(s_k))$, thereby establishing a map between every k-tuple $\mathbf{s}^{(k)}$ and an element of the set $\mathbb{Z}_{N+1}^k$, where $\mathbb{Z}_{N+1} = \{0, 1, \ldots, N\}$. In more detail, the vector $\mathbf{d}^{(k)}$ represents the fact that $\mathbf{s}^{(k)} \in I_{d(s_1)} \times I_{d(s_2)} \times \cdots \times I_{d(s_k)} = \mathcal{I}(\mathbf{d}^{(k)}) \subset \mathbb{R}^k$.

An FSMC channel model entails the assumption that the statistics of the SNR have the Markov property (a common means of describing correlated SNR evolution over time [39]); the model can then be derived from the distribution of the SNR, which in this case is given by the Gaussian fitting discussed above. If the pdf of the SNR, denoted with γ, is called $f_\Gamma(\gamma)$, the state space of the channel is $\mathbb{Z}_{N+1}$, and the steady-state distribution is given by

$$\pi_i = \int_{\alpha_i}^{\alpha_{i+1}} f_\Gamma(\gamma)\, \mathrm{d}\gamma, \quad i = 0, \ldots, N. \tag{4.10}$$

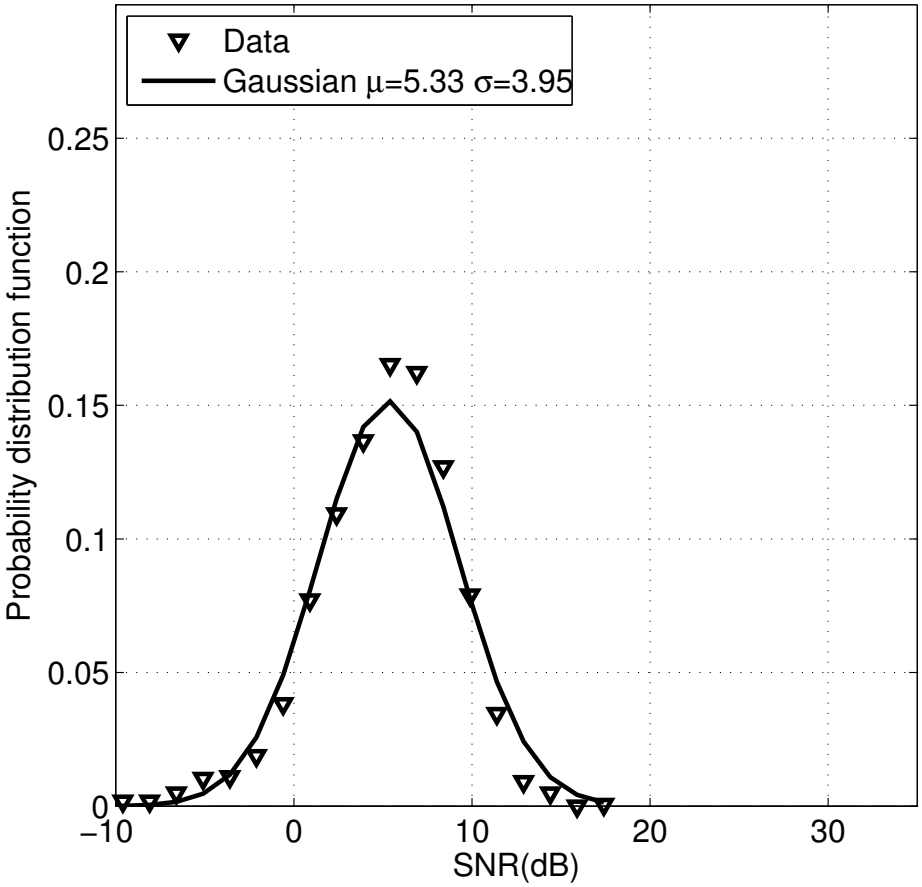

Figure 4.20. *Empirical PDF of the SNR and Gaussian fit over the T2–H1 link.*

Analogously, the probability that a transition between state i and j occurs, t_{ij}, can be derived as follows

$$t_{ij} = \frac{\int_{\alpha_i}^{\alpha_{i+1}} f_\Gamma(\gamma_0) \int_{\alpha_j}^{\alpha_{j+1}} f_\Gamma(\gamma|\gamma_0)\, \mathrm{d}\gamma\, \mathrm{d}\gamma_0}{\int_{\alpha_i}^{\alpha_{i+1}} f_\Gamma(\gamma_0)\, \mathrm{d}\gamma_0}, \quad i, j \in \mathbb{Z}_{N+1} \tag{4.11}$$

where $f_\Gamma(\gamma|\gamma_0)$ is the conditional pdf of the SNR γ given the previous SNR value γ_0.

The channel transition probability matrix is then defined as $\mathbf{T} = (t_{ij})$ for $i, j \in \mathbb{Z}_{N+1}$. We remark that given the limited size of the available SNR data sets, estimating a close-form fit of conditional distributions may yield little significance. We therefore resort to direct estimation of channel transition probabilities from the data, by taking the relative frequencies of SNR transitions between any two intervals I_i, I_j, where $i, j \in \mathbb{Z}_{N+1}$ represent the indices of the starting and ending intervals respectively.

It is worth noting that the transition probabilities strongly depend on the number of states used to quantize the channel, and therefore on the number of thresholds used for

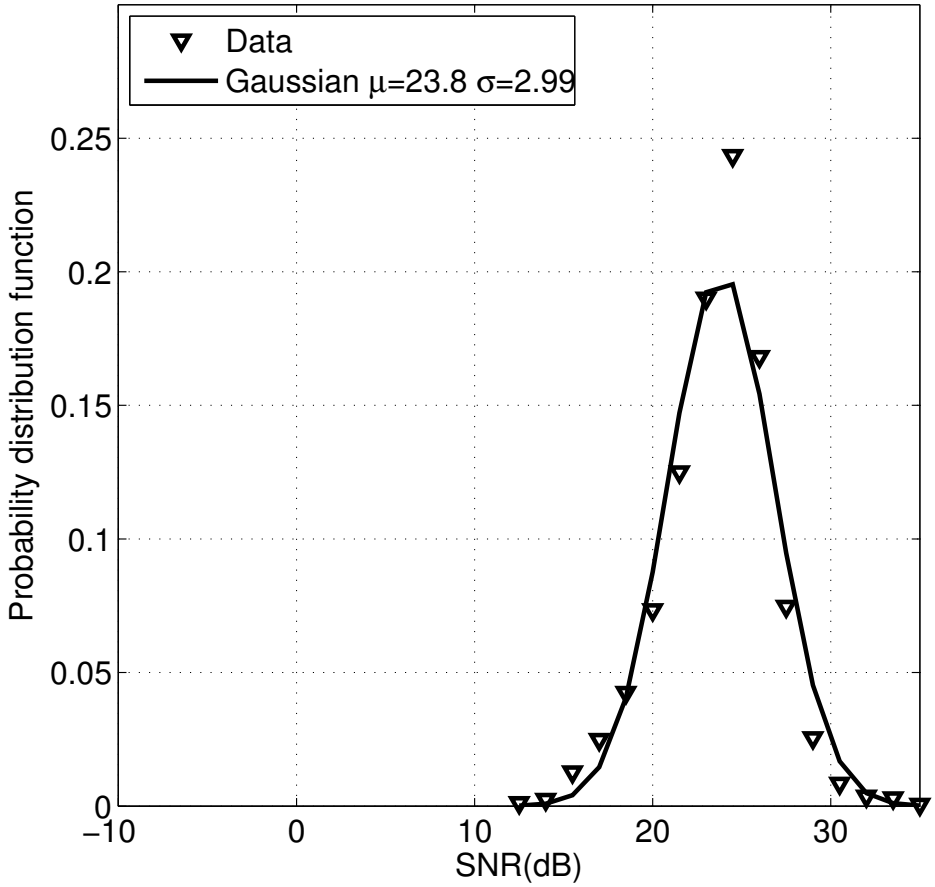

Figure 4.21. *Empirical PDF of the SNR and Gaussian fit over the T3–H1 link.*

delimiting SNR intervals (or, equivalently, SNR probability intervals). We will employ only two thresholds, resulting in a total of three channel states. This choice results in a very simple channel model, but still provides sufficient quantization accuracy, as shown by the numerical results.

4.5.3 Models for HARQ Schemes

The previous section focused on describing how a FSMC model of the channel can be derived from experimental data. We now focus on how to employ this FSMC to model an HARQ error control process based on the good LDPC code ensembles the FSMC has been matched to. Recall that $\mathbf{T}$ denotes the transition probability matrix of the FSMC. The FSMC has in general $N+1$ states $0, 1, \ldots, N$, if N thresholds are chosen to quantize the channel behavior. With no loss of generality, assume that 0 is the best state, i.e., the one associated

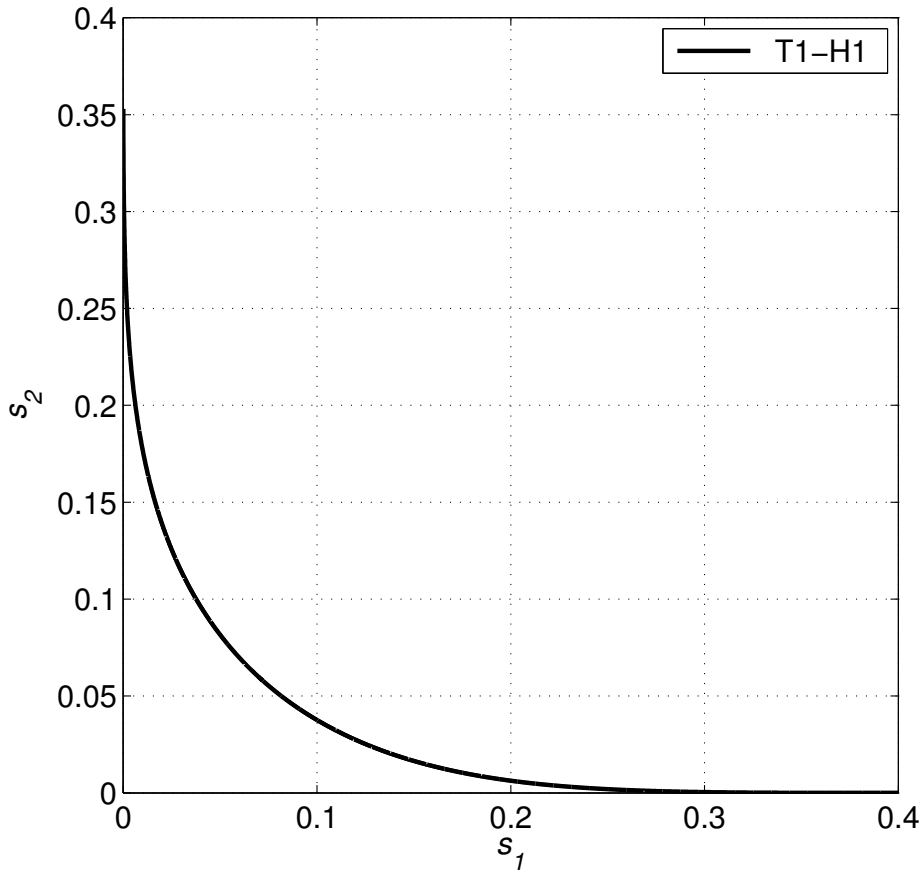

Figure 4.22. *Reliable regions for the T1–H1 link.*

to the highest values of the SNR, whereas N is the worst state. Let us define a map $g(j)$ which associates each state index j, $j = 0, \ldots, N$, to an "error level" a packet would incur if transmitted while the channel is in state j. The error level is a non-decreasing function of the state index, and is employed to describe the usefulness of the packet being transmitted for the decoding of the LDPC codeword at the receiver as follows. Recall from the beginning of Section 4.5.1 that every information frame is encoded and divided in HARQ fragments, to be transmitted sequentially, and that a single correct HARQ fragment is always sufficient to successfully decode the whole information frame. However, corrupted fragments may still be used at the receiver, according to the type of HARQ scheme, as will be explained in detail later. To model this HARQ feature, we assume that a successful decoding takes place after reception of HARQ fragment k only if the overall error level (which is defined as the error level of fragment k for Type I HARQ, and as the sum of the error levels of all HARQ fragments received so far for IR-HARQ) is lower than or equal to a certain threshold θ_k [38].

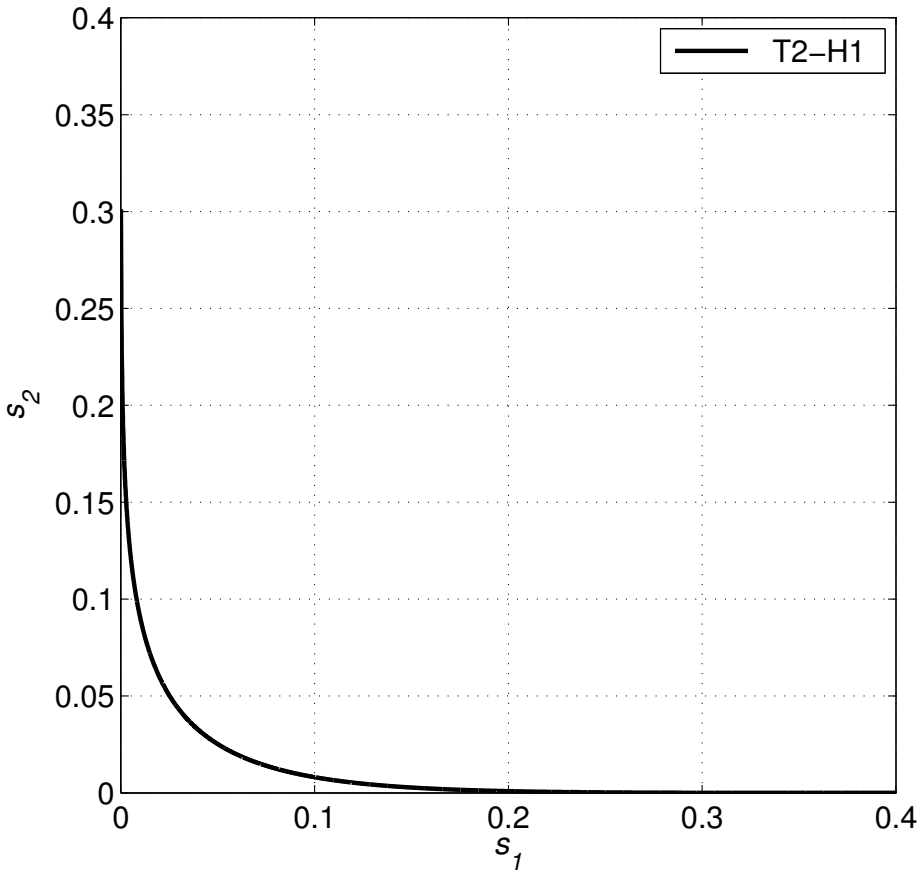

Figure 4.23. *Reliable regions for the T2–H1 link.*

With the above in mind, and for a fixed SNR statistics over the link, the performance of the HARQ scheme only depends on the round-trip time of the channel, m, and on the maximum number of retransmissions allowed before an information frame is discarded, denoted by F [38]. Recall that our data set contains transmissions performed once every $15\,\mathrm{s}$, which is much larger than the average propagation delay, given the distances between the transmit and receive hardware. Hence, we have to fix $m = 1$ for our data set, which corresponds to assuming that a slotted approach is taken, whereby each slot is long enough to accommodate the maximum round-trip time (that between T2 and the VA) and the time required for acoustic reverberation to fade out. Taking higher values for m would correspond to assuming that the links span a distance of more than $22.5\,\mathrm{km}$, which would make the measured SNR statistics meaningless. Finally, note that setting $m = 1$ means that transmitted frames are actually sent only after receiving the ACK/NACK feedback related to the previous message, so that at every time instant there is at most one message in flight over the channel (i.e.,

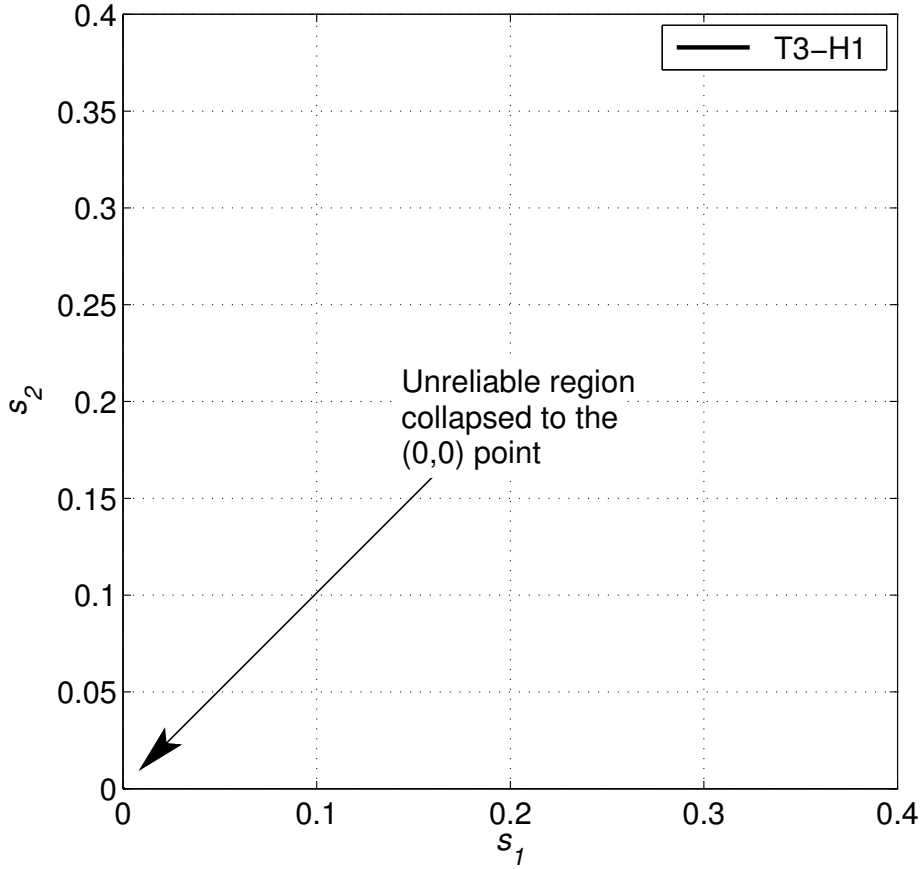

Figure 4.24. *Reliable regions for the T3–H1 link.*

the ARQ scheme is Stop-and-Wait). Due to the long propagation delay, we also assume that each corrupted packet can be retransmitted only once, i.e., $F = 1$, and if the retransmission also fails the packet is discarded.

In general, at each time we need to keep track of the number of retransmissions already made and of the correspondingly accumulated error level, as well as of the channel state. The resulting model can be derived in general form following the approach described in [38]. In the following subsections we will instead focus on a simpler model for the Type I and Type II HARQ schemes in the specific case $F = 1, m = 1, N = 2$.

4.5.4 Type II (Incremental Redundancy) HARQ

We start with the description of the Type II HARQ (IR-HARQ) scheme. We employ two thresholds to describe the channel behavior, resulting in three channel states, namely 0 (error-free state), 1 (some recoverable errors), 2 (worst state with unrecoverable errors). In

general, each state j is associated to a different error level incurred by a fragment transmitted when the channel is in that state through the map $g(j)$ (see Section 4.5.3). According to the above description, we simply set $g(j) = j$.

If the transmission of the first fragment occurs when the channel is in state 0 (error-free state), the frame is correctly received and no retransmission is needed. If instead the first fragment is in error, a new fragment is transmitted, and the frame can still be recovered if the pair of states for the two attempts is $(1, 0)$, $(1, 1)$ or $(2, 0)$, whereas we assume that the situations $(2, 1), (1, 2)$, and $(2, 2)$ correspond to too many errors, and do not lead to successful frame recovery. This corresponds to the set of thresholds $\theta_0 = 0$ and $\theta_1 = 2$.

Hence, we represent the system state with a pair (S, r), where S represents the previous channel state (required to track the evolution of the Markov channel) and r denotes the number of transmissions already made for the current frame, i.e., $r = 0$ for the first fragment and $r = 1$ for a retransmission. In this simplified model, there is no need for an explicit variable tracking the error level of the packet, as it is identical to S. Note also that there are only *five* possible states (S, r), although S and r can take three and two values, respectively. Indeed, the combination $S = 0, r = 1$ is invalid as it would correspond to the retransmission of a correctly received frame.

Define now σ_{Sr} as the steady-state probability of being in state (S, r). If t_{ij} denotes the probability of making a transition from channel state i to state j, the balance equations between such steady-state probabilities can be found as follows

$$\sigma_{00} = \sum_{i=0}^{2} \sigma_{i0} t_{i0} + \sum_{i=1}^{2} \sigma_{i1} t_{i0} \tag{4.12}$$

$$\sigma_{S0} = \sum_{i=1}^{2} \sigma_{i1} t_{iS} \quad \text{for } S = 1, 2 \tag{4.13}$$

$$\sigma_{S1} = \sum_{i=0}^{2} \sigma_{i0} t_{iS} \quad \text{for } S = 1, 2 \tag{4.14}$$

These equations can be put into a system which can be solved by imposing the additional condition that the sum of all σ_{Sr} equals 1. After solving the system, one can directly compute the throughput, Θ (average number of successful frames per slot), the average number of retransmissions per correctly decoded information frame, N_{fr}, and the probability that a

frame is discarded, P_{fd} (i.e., the fraction of frames that are not correctly received), as

$$\Theta = \sum_{i=0}^{2} \sigma_{i0} t_{i0} + \sum_{i=1}^{2} \sigma_{i1} t_{i0} + \sigma_{11} t_{11} = \sigma_{00} + \sigma_{11} t_{11} \ , \tag{4.15}$$

$$N_{fr} = \frac{\sigma_{11} t_{10} + \sigma_{11} t_{11} + \sigma_{21} t_{20}}{\sum_{i=0}^{2} \sigma_{i0} t_{i0} + \sum_{i=1}^{2} \sigma_{i1} t_{i0} + \sigma_{11} t_{11}} \ , \tag{4.16}$$

$$P_{fd} = \frac{\sum_{i=0}^{2} \sigma_{i0} (t_{i1} t_{12} + t_{i2}(1 - t_{20}))}{\sum_{i=0}^{2} \sigma_{i0}} \ . \tag{4.17}$$

Eq. (4.15) is derived by summing the probabilities of all transitions that correspond to a successful frame in a slot, which include all cases in which a transmission occurs in channel state 0, plus the case in which a retransmission in state 1 follows an erroneous transmission that was itself in state 1. (Note the simplification allowed by the balance equation (4.12).) Eq. (4.16) is again obtained by enumerating all events that correspond to the successful delivery of a frame in a slot: the sum of the probabilities of these events is the denominator of (4.16), whereas the numerator is the sum of the probabilities of only those that correspond to a success after retransmission. (Note that the denominator in this case is the throughput Θ.) Finally, Eq. (4.17) is derived as follows. When the first fragment of a frame is transmitted, we must have $r = 0$, so that the only three possible states are $(S, 0), S = 0, 1, 2$. Given that the channel state is S, the probability that the frame is discarded is the probability that the two transmission attempts have an error level that is not sufficient for decoding, which is equal to $t_{S1} t_{12} + t_{S2}(1 - t_{20})$. The final result is obtained by averaging this probability over the *normalized* distribution of the channel state, $\sigma_{S0} / \sum_{i=0}^{2} \sigma_{i0}$.

4.5.5 Type I HARQ

As a term of comparison, we also consider a Type I hybrid HARQ where only one HARQ fragment is actually transmitted per information frame, so that encoding provides only some protection against channel errors over a single packet transmission. However, no more than one HARQ fragment is considered at every decoding attempt: therefore, further retransmissions can help the decoding process only by providing more chances to incur a sufficiently high SNR value. This entails the definition of a single threshold which is equal to the noise threshold of the LDPC code ensemble, and leads therefore to two cases: if the SNR is above the threshold, the frame is correctly decoded; otherwise, it is retransmitted

once, and if again the SNR threshold is not met, it is discarded. For a fair comparison, we keep the maximum number of retransmissions as $F = 1$ in this case as well.

This situation can be modeled using the same set of balance equations as before. However, in Eqs. (4.15)–(4.17) the effect of incremental redundancy must be removed, i.e., two subsequent transmissions of the same frame that both experience channel state 1 no longer yield a correct decoding, and therefore any term that relates to this event is to be counted as a failure rather than a success. In this case we have

$$\Theta = \sigma_{00} \ , \tag{4.18}$$

$$N_{fr} = \frac{\sigma_{11} t_{10} + \sigma_{21} t_{20}}{\Theta} \ , \tag{4.19}$$

$$P_{fd} = \frac{\sum_{i=0}^{2} \sigma_{i0} (t_{i1}(1 - t_{10}) + t_{i2}(1 - t_{20}))}{\sum_{i=0}^{2} \sigma_{i0}} \ . \tag{4.20}$$

4.5.6 Results

We now show a comparison of throughput, probability of frame discarding and average number of HARQ fragments per correctly decoded frame as derived by the analysis discussed above. The analysis is compared to simulation results obtained by reproducing the evolution of the Type I and II HARQ over the SNR traces employed to derive the Markov models.

All results are plotted as a function of the average transmit power: for each point on the curve, SNR traces are offset in order to simulate a different transmit power; in turn, this changes the average value of the distribution of the SNR, affecting the size of the reliable code region, and the performance of the decoding process. All other parameters are set as discussed above.

4.5.7 Training over a complete SNR trace

Figs. 4.25, 4.26 and 4.27 show the throughput Θ, average number of retransmissions N_{fr} and probability of frame discarding P_{fd}, respectively. The T1–H1 and T3–H1 links are considered. For this evaluation, the Markov models have been trained over the whole SNR traces of the experiment: this is meant as a general sanity check for the use of such models in the context of underwater networks. Later in this section we will also validate the results by

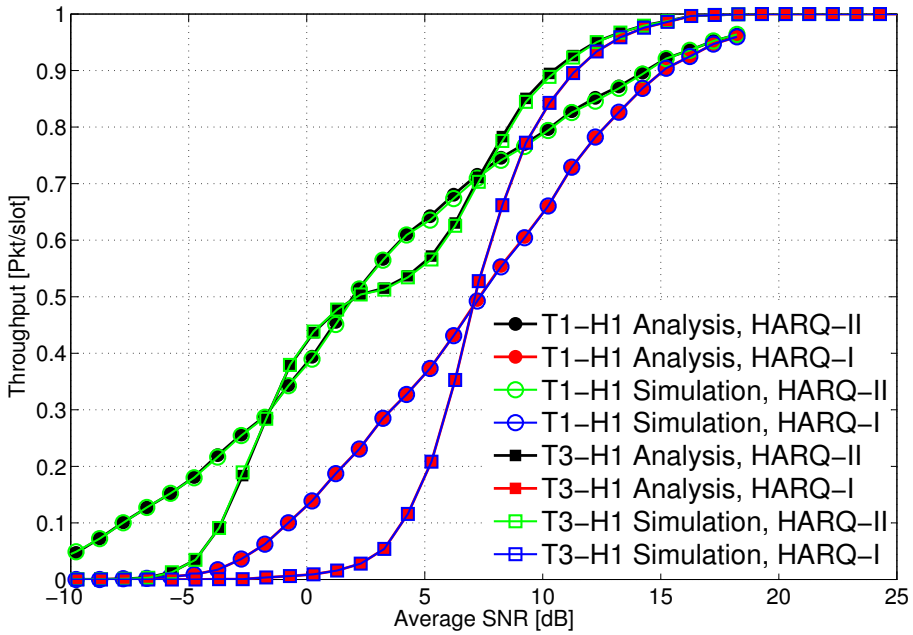

Figure 4.25. *Throughput Θ as a function of the average SNR for links T1–H1 and T3–H1.*

training the model over a portion of the dataset in order to obtain analytical results, while performing simulations over a different portion of the traces of the same experiment.

We start by considering throughput in Fig. 4.25. The curves show two expected behaviors, namely i) that the performance of error control schemes improves with higher average SNR (which increases the length of sojourns in favorable states of the Markov model); ii) that Type I HARQ is consistently outperformed by Type II HARQ which is in line with common wisdom (e.g., see [42]).

In addition, we observe that the analysis fits simulation results quite accurately; this suggests that Markov models are in fact a good choice to achieve a high-level representation of the channel behavior as they can correctly reproduce the statistics of the SNR process.

The SNR distribution significantly impacts the behavior of the curves: in fact, the slope of the transitional portion of the curve (when throughput increases from 0 to 1) is steeper for more stable links, and milder for links exhibiting greater variance. For example, compare HARQ performance with the behavior of SNR over time as seen in Fig. 4.17: note that while T3 experiences high, fairly stable SNR, T1 is subject to an initially lower SNR that however increases after roughly 4 hours since the beginning of the experiment. Nevertheless, due to the greater dispersion of data over a larger interval of SNR values throughout the ex-

periment, T1's SNR distribution has higher variance than T3's. Therefore, the throughput increase over the T3–H1 link is steeper, and T3's throughput eventually tops T1's. While not shown here due to lack of space, other links (e.g., from T1 and T3 to H4) show generally similar trends. In particular, links from closer transmitters consistently exhibit better performance, and in addition more stable links show steeper transitions in the throughput curves.

Consider now Figs. 4.26 and 4.27 showing the number of retransmissions and the probability of frame discarding, respectively, for the T1–H1 and T3–H1 links. The general trends, in terms of the relative performance of the two links, reflect that observed for throughput. However, Fig. 4.26 shows a further difference between the Type I and Type II HARQ policies: as long as the average SNR is low, the number of retransmissions incurred by Type I HARQ is 0.5, whereas that of Type II HARQ is 1. In fact, N_{fr} is conditioned on having correctly decoded an information frame: in unfavorable channel conditions this event is so rare that Type I HARQ experiences a success during the first fragment transmission or during the first retransmission with equal probability. With Type II HARQ, instead, the transmission of a second fragment always improves the decoding performance, making it more likely to successfully decode after the first retransmission, thereby shifting N_{fr} to 1. Fig. 4.27 supports this interpretation by showing that Type II HARQ indeed yields a lower probability of frame discarding.

4.5.8 Model Validation

In all figures discussed above, the simulation results match the analysis quite accurately. This is a consequence of having trained the Markov models over the full SNR traces, and of having performed simulation runs over the same traces. In this subsection, we validate the accuracy of the models by training over a different portion of data set than used in the simulation. In any event, all portions belong to the same experiment. We consider first a mildly non-stationary case, whereby the model is trained over the portion from one half to three quarters of the SNR time series obtained at H1, whereas simulations are run on the last quarter of the same time series. We observe from Fig. 4.17 that, e.g., the T3–H1 link is very stationary during this portion of the experiment, while T1 undergoes broader changes as the average SNR oscillates and tends to decrease toward the end of the experiment. This

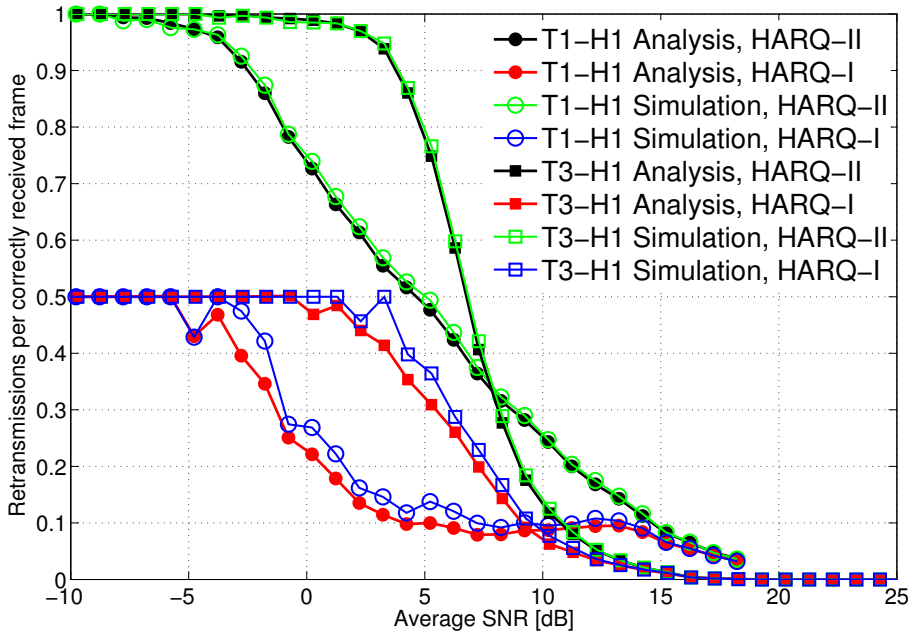

Figure 4.26. *Number of retransmissions per correctly received frame, N_{fr}, as a function of the average SNR for the links T1–H1 and T3–H1.*

case is covered by Figs. 4.28, 4.29 and 4.30 showing throughput, number of retransmissions and probability of frame discarding, respectively. The limited amount of variations in the SNR traces from the portion used in the analysis and that used in simulations reflects into a very good agreement between simulation and analysis for both the T3–H1 link and the T1–H1 link. The only slight disagreement comes from T1–H1's N_{fr} metric (Fig. 4.29) for an average SNR of 1 to $4\,\mathrm{dB}$, and is due to an insufficient number of correctly received packets, leading to lower statistical significance of the expectations performed to calculate the value of the metric.

For comparison, we also considered a non-stationary case, whereby the model is trained over the first half, whereas simulations are run on the second half of the SNR time series of H1. In this case, both the T3–H1 and the T1–H1 links experience variations, which are limited for T3–H1, but of greater entity for T1–H1, whose average SNR increases by about $10\,\mathrm{dB}$ in the second half of the experiment, with respect to the first half. This case is covered by Figs. 4.31, 4.32 and 4.33 where we observe that the model is acceptably accurate for the T3–H1 link, and less accurate for T1–H1. In any event, despite some disagreement, the accuracy is still acceptable for the model to work at least as an approximation of the link behavior. This may still make it suitable, e.g., to be implemented in a network simulator.

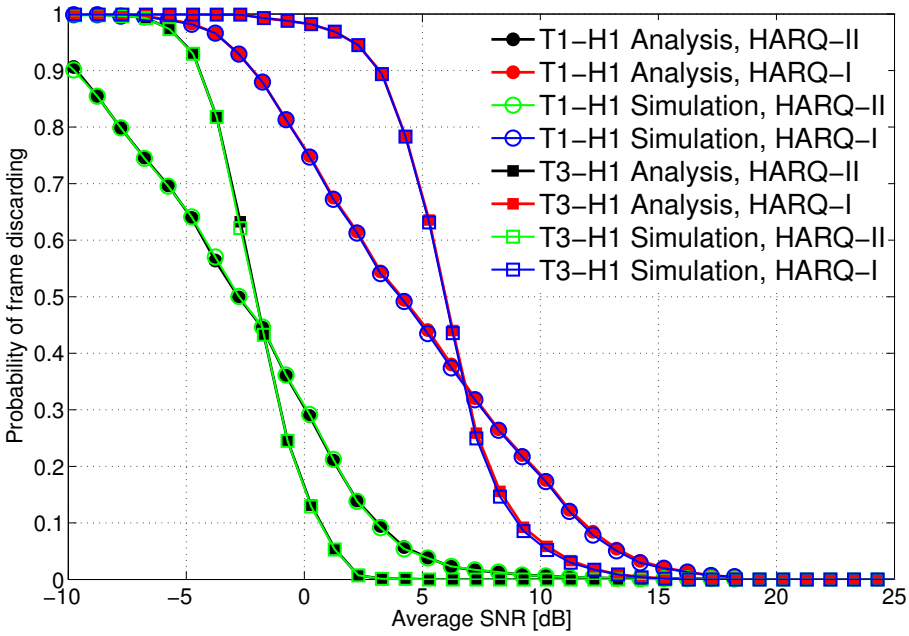

Figure 4.27. *Probability of discarding a data frame, P_{fd}, as a function of the average SNR for links T1–H1 and T3–H1.*

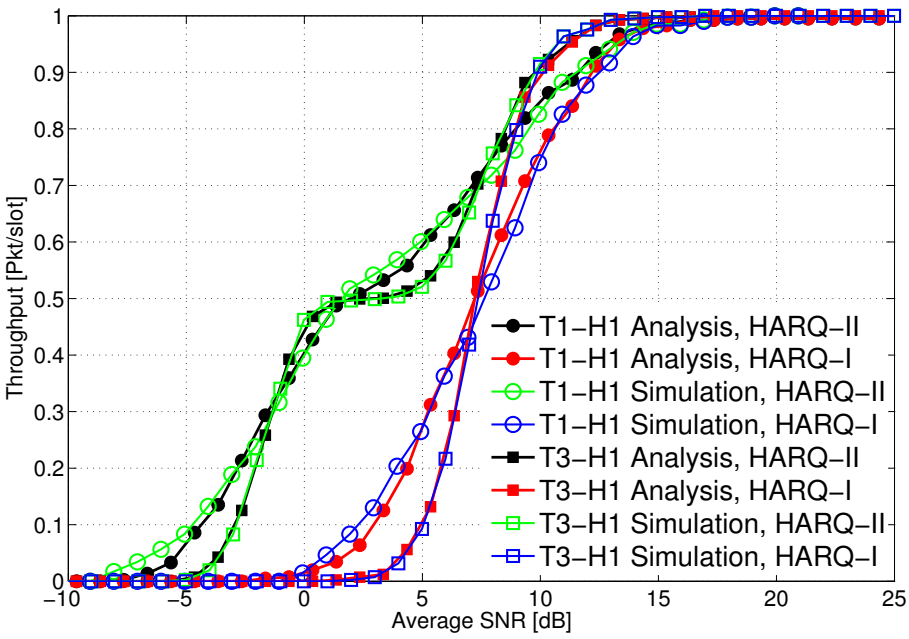

Figure 4.28. *Model validation, mildly non-stationary case: model trained over the* third quarter*, simulations run over the* fourth quarter *of the SNR time series. Throughput, Θ.*

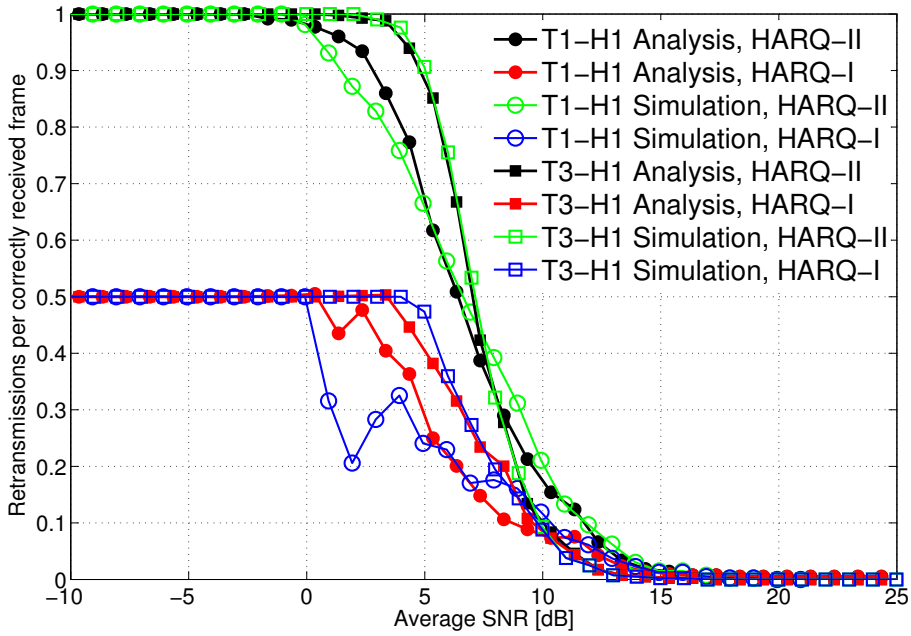

Figure 4.29. *Model validation, mildly non-stationary case: model trained over the* third quarter, *simulations run over the* fourth quarter *of the SNR time series. Average number of retransmissions,* N_{fr}.

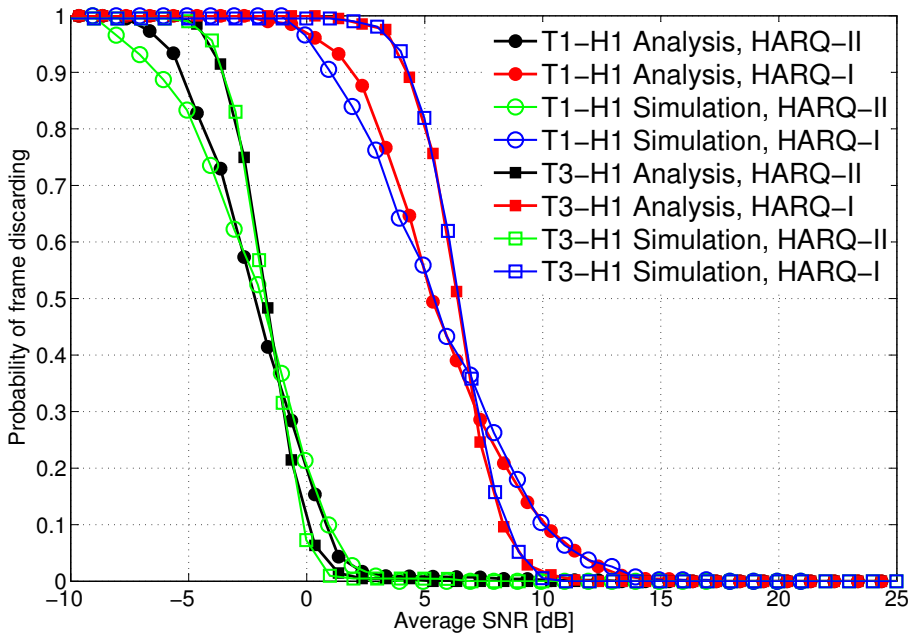

Figure 4.30. *Model validation, mildly non-stationary case: model trained over the* third quarter, *simulations run over the* fourth quarter *of the SNR time series. Probability of frame dropping,* P_{fd}.

4.6 Adaptive Modulation

4.6.1 System Model and Performance Analysis

We consider an adaptive modulation system using BPSK and M-ary Quadrature Amplitude Modulation (M-QAM) constellations signaling over Nakagami-m fading channels. In

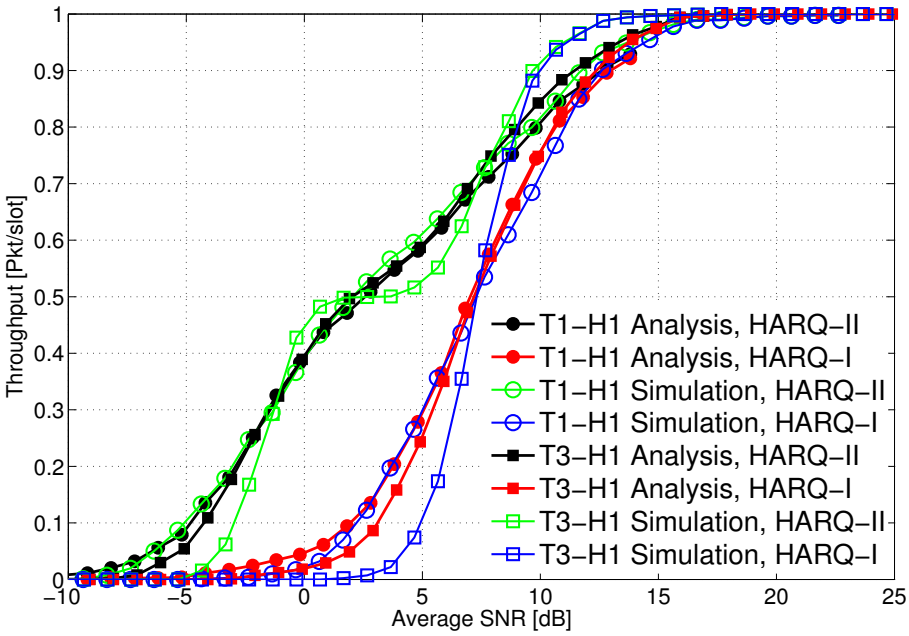

Figure 4.31. *Model validation, non-stationary case: model trained over the* first half*, simulations run over the* second half *of the SNR time series. Throughput,* Θ.

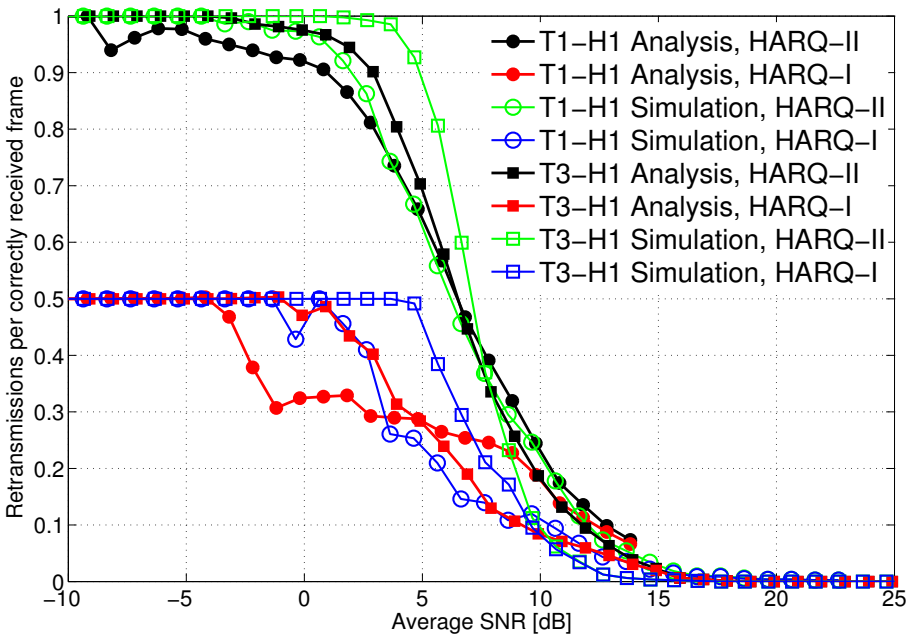

Figure 4.32. *Model validation, non-stationary case: model trained over the* first half*, simulations run over the* second half *of the SNR time series. Average number of retransmissions,* N_{fr}.

particular, we assume that a finite set of $J+1$ modulation schemes can be chosen, each having a different constellation size $\{M_0, M_1, \ldots, M_J\}$, and leading to a different probability of

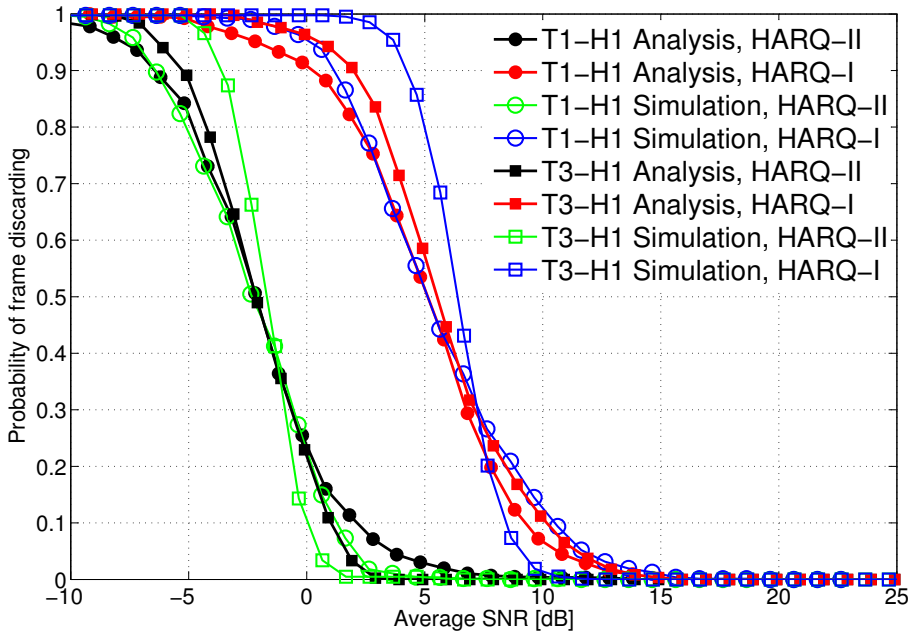

Figure 4.33. *Model validation, non-stationary case: model trained over the* first half*, simulations run over the* second half *of the SNR time series. Probability of frame dropping,* P_{fd}.

error as a function of the receive SNR and a different spectral efficiency, in terms of bits transmitted per channel use. For the purposes of the present study, let $M \in \{2, 4, 16, 64, 256\}$:[3] therefore $J = 4$. While we refer the reader to [43] for details on variable-rate adaptive M-QAM modulation under the ideal CSI assumption, we remark here that the rationale behind the adaptation of the modulation signaling is to exploit the changes in the channel propagation gain to the system's advantage, i.e., by pushing a larger number of bits per symbol through a constellation with a higher number of levels when the SNR is favorable, while backing off to more robust constellations (such as BPSK's or QPSK's) whenever the SNR drops below an acceptable value for higher-order modulations. To this end, a straightforward solution is to choose the modulation for the current transmission in an opportunistic fashion, i.e., by choosing the modulation j, with M_j levels, whenever the measured SNR γ falls within a prescribed interval of the form $[\gamma_j^*, \gamma_{j+1}^*)$. The thresholds γ_j^* and γ_{j+1}^* are chosen so that the SNR is at least as high as required to ensure a prescribed performance level with modulation j (e.g., a BER of no more than a desired level P_{b}^*), yet insufficient to

[3]We note that these modulations are standard in digital video transmission, e.g., 4- to 64-QAM are used in the European Telecommunications Standards Institute (ETSI)'s DVB-T standard, whereas the 16- to 256-QAM schemes are adopted in the DVB-C standard [59].

achieve the same performance using the higher spectral efficiency modulation $j+1$. Some hysteresis may be built into the switching scheme to prevent continual level changing [60], but this solution, though practical, does not yield additional insight to the analysis we carry out in the following, and is therefore not considered here. The spectral efficiency achieved by choosing modulation j is then $\log_2 M_j$ bits per channel use, $j = 0, \ldots, J$.

From a practical standpoint, given a transmitter-receiver pair, the receiver is assumed to provide a measure of the SNR γ to the transmitter, which will then take the highest j such that the modulation with M_j levels has a BER $P_{\mathrm{b}}(\gamma) < P_{\mathrm{b}}^*$, where P_b^* is some desirable value.[4] For BPSK, as well as for M-QAM the exact formula of the BER is given in

$$QAMper \tag{4.21}$$

[61], where $Q(x) \triangleq \int_x^\infty e^{-t^2/2}\,\mathrm{d}t/\sqrt{2\pi}$ is the Gaussian-Q function. Whenever the SNR falls below the value required to guarantee a BER of no more than P_{b}^* to the most robust modulation with $M_0 = 2$ levels, the system is said to be in outage. However, note that such definition of outage is only valid under an instantaneous channel knowledge assumption. We will relax this later by accounting for outdated knowledge, and therefore extend the concept of outage correspondingly.

For now, assume that the SNR, ideally estimated at the receiver, is sent back to the transmitter on an error-free delayed channel. Also, recall that the channel fading effects are modeled by a Nakagami-m process. Let E_{s} denote the symbol energy (averaged over the distribution of fading), $N_0/2$ the two-sided power spectral density of the additive white Gaussian noise process at the receiver, and h the fading gain, assumed to have a Nakagami-m distribution. Because the instantaneous SNR can be written as $\gamma = |h|^2 E_{\mathrm{s}}/N_0$ its PDF $f_\gamma(\gamma)$ and its CDF $F_\gamma(\gamma)$ are respectively given by [62, pp. 21–24]

$$f_\gamma(\gamma) = \frac{m^m \gamma^{m-1}}{\overline{\gamma}^m \Gamma(m)} \exp\left(-\frac{m\gamma}{\overline{\gamma}}\right), \tag{4.22}$$

$$F_\gamma(\gamma) = 1 - \frac{\Gamma\left(m, \frac{m\gamma}{\overline{\gamma}}\right)}{\Gamma(m)}, \tag{4.23}$$

for $\gamma \geq 0$, where $\Gamma(\,\cdot\,)$ is the Gamma function, $\overline{\gamma} = \mathbb{E}\left[|h|^2\right] E_{\mathrm{s}}/N_0$, is the mean SNR, and m is the Nakagami-m fading parameter, which ranges from $1/2$ to $+\infty$.

For a given maximum target BER, typical performance metrics for adaptive modulation systems are the average Spectral Efficiency (SE), defined as the average number of bits per

[4] In the following evaluation, P_b^* will be fixed to 10^{-2}.

channel use allowed by the adaptation scheme, and the Bit Error Outage (BEO), defined as the probability that the system cannot satisfy the prescribed performance in terms of bit error rate. We consider both metrics in the following, and provide their analytical expressions in the presence of both instantaneous and outdated channel knowledge at the transmitter.

4.6.2 Instantaneous CSI

Ideal adaptive modulation systems are said to be in outage whenever the SNR makes the most robust modulation M_0 achieve a BER worse than P_b^*. When ideal CSI (perfect channel estimation and instantaneous channel knowledge) is available at the transmitter, the BEO can be evaluated as the probability of experiencing an SNR level lower than the minimum threshold γ_0^*:

$$P_{\mathrm{o}}(P_{\mathrm{b}}^*) = \mathbb{P}\left\{P_{\mathrm{b}}^{(0)}(\gamma) > P_{\mathrm{b}}^*\right\} = F_\gamma\left(\gamma_0^*\right) . \tag{4.24}$$

The average SE can be expressed in terms of the number of bits per symbol in each modulation, averaged over the probability of choosing that modulation:

$$\begin{aligned}\eta &= \sum_{j=0}^{J-1} \tilde{M}_j \, \mathbb{P}\left\{\gamma_j^* < \gamma \leq \gamma_{j+1}^*\right\} + \tilde{M}_J \, \mathbb{P}\left\{\gamma_J^* < \gamma\right\} \\ &= \sum_{j=0}^{J-1} \tilde{M}_j \left[F_\gamma(\gamma_{j+1}^*) - F_\gamma(\gamma_j^*)\right] + \tilde{M}_J \left[1 - F_\gamma(\gamma_J^*)\right] ,\end{aligned} \tag{4.25}$$

where $\tilde{M}_j = \log_2 M_j$. We also define the throughput of the system, denoted as G in the following, by taking the product of the spectral efficiency of either modulation and the related probability of correct bit reception, averaged over the values of the SNR for which that modulation is chosen. We have

$$G = \sum_{j=0}^{J} \tilde{M}_j \int_{\gamma_j^*}^{\gamma_{j+1}^*} \left[1 - P_{\mathrm{b}}^{(j)}(\gamma)\right] f_\gamma(\gamma) \, \mathrm{d}\gamma , \tag{4.26}$$

where we let $\gamma_{J+1}^* = +\infty$.[5]

4.6.3 Outdated CSI

We now evaluate the effect of delayed channel knowledge on the system performance. To this end, we assume that the information about the value of the SNR γ, estimated by

[5]We note that the analysis is conceptually equivalent if we consider the packet error probability instead of the bit error probability.

the receiver at a given time t, will be available at the transmitter only after a delay τ, i.e., at time $t+\tau$. Therefore, the opportunistic choice of the constellation size will still be based on the value of γ, but when such a constellation will be used, i.e., at time $t+\tau$, the SNR will have evolved to a different value $\gamma_\tau = |h_\tau|^2 E_s/N_0$ [6]. At this point, if $\gamma < \gamma_\tau$, the SNR is underestimated and, compared to the instantaneous knowledge case, a too conservative constellation size might be chosen for transmission. On the contrary, when $\gamma > \gamma_\tau$, the SNR is overestimated, and the chosen modulation level might not meet the prescribed BER requirements. In other words, although $\gamma \in [\gamma_j^*, \gamma_{j+1}^*)$, leading to the choice of modulation j, γ_τ might be such that $P_{\mathrm{b}}^{(j)}(\gamma_\tau) > P_{\mathrm{b}}^*$. In the latter case, the system is also in outage. In particular, an outage event occurs if $\gamma < \gamma_0^*$ or $\gamma \geq \gamma_0^*$, $\gamma \in [\gamma_j^*, \gamma_{j+1}^*)$ (hence, modulation j is chosen), but $\gamma_\tau < \gamma_j^*$. Then, the BEO can be written as

$$P_{\mathrm{o}} = F_\gamma\left(\gamma_0^*\right) + \sum_{j=0}^{J} P_{\mathrm{o}|j}\,, \tag{4.27}$$

where $P_{\mathrm{o}|j}$ denotes the joint probability that the current SNR is not sufficient to withstand the requirements of modulation j, and is found by integrating the distribution of γ_τ over $[0, \gamma_j^*)$ (i.e., where modulation j is in outage) and that γ was sufficient to enable the use of modulation j:

$$P_{\mathrm{o}|j} = \int_{\gamma_i^*}^{\gamma_{i+1}^*} \int_0^{\gamma_j^*} f_{\gamma_\tau|\gamma}\left(\gamma_\tau\right) f_\gamma(\gamma)\, \mathrm{d}\gamma_\tau\, \mathrm{d}\gamma\,, \tag{4.28}$$

where we let $\gamma_{J+1}^* = +\infty$, and $f_{\gamma_\tau|\gamma}(\gamma_\tau)$ is the PDF of γ_τ conditioned on γ. This distribution can be found as [63]

$$\begin{aligned} f_{\gamma_\tau|\gamma}\left(\gamma_\tau\right) = {} & \frac{m}{(1-\rho_\tau)\overline{\gamma}} \left(\frac{\gamma_\tau}{\rho_\tau \gamma}\right)^{(m-1)/2} \\ & \times I_{m-1}\left(\frac{2m\sqrt{\rho_\tau \gamma \gamma_\tau}}{(1-\rho_\tau)\overline{\gamma}}\right) \exp\left(\frac{m(\rho_\tau \gamma + \gamma_\tau)}{(1-\rho_\tau)\overline{\gamma}}\right)\,, \end{aligned} \tag{4.29}$$

where $I_{m-1}(\cdot)$ is the modified Bessel function of the first kind and order $m-1$ [64], and ρ_τ is the correlation factor between the SNR process and its τ-lagged version, which is estimated as

$$\rho_\tau = \frac{\sum_{t=0}^{N-1}(\gamma_t - \overline{\gamma})(\gamma_{t+\tau} - \overline{\gamma})}{\sqrt{\sum_{t=0}^{N-1}(\gamma_t - \overline{\gamma})^2 \sum_{t=0}^{N-1}(\gamma_{t+\tau} - \overline{\gamma})^2}}\,, \tag{4.30}$$

[6] In the following we assume that the channel is stationary and thus assume $t = 0$ with no loss of generality. From a practical standpoint, this translates into considering a portion of the experiment within a limited time window, during which the channel exhibits an approximately stationary behavior.

where N is the length of the dataset over which the estimation is performed, and depends on the time coherence of the SNR process. We note that in (4.30) we are estimating the correlation of the power envelope of the fading process, and therefore remove the average value from the SNR time series [65]. The Nakagami m-parameter can finally be estimated as

$$m = \frac{\overline{\gamma}^2}{\mathbb{E}[(\gamma - \overline{\gamma})^2]}. \tag{4.31}$$

The spectral efficiency η must be computed by considering the joint distribution of γ and γ_τ. In particular, in the present analysis, we define η as the spectral efficiency of the chosen modulation whenever the SNR γ_τ (which affects the actual transmission) is sufficient to support the modulation, and 0 otherwise. Therefore, we have

$$\eta = \sum_{j=0}^{J} \tilde{M}_j \int_{\gamma_j^*}^{\gamma_{j+1}^*} \int_{\gamma_j^*}^{+\infty} f_{\gamma_\tau|\gamma}(\gamma_\tau)\, f_\gamma(\gamma)\, \mathrm{d}\gamma_\tau\, \mathrm{d}\gamma \tag{4.32}$$

and, similarly to the instantaneous knowledge case, the throughput is found as

$$G = \sum_{j=0}^{J} \tilde{M}_j \int_{\gamma_j^*}^{\gamma_{j+1}^*} \int_{\gamma_j^*}^{+\infty} \left[1 - P_b^{(j)}(\gamma_\tau)\right] f_{\gamma_\tau|\gamma}(\gamma_\tau)\, f_\gamma(\gamma)\, \mathrm{d}\gamma_\tau\, \mathrm{d}\gamma\,. \tag{4.33}$$

4.6.4 Analysis and Simulation Results

We start the description of our results by considering spectral efficiency, for the experiment and the links already presented in Figure 3.12. We focus on this specific subset of results because it shows a highly time-varying channel set.

Figures 4.34, 4.35 and 4.36 detail the spectral efficiency against average SNR for links from T1 to H1, H2 and H4, respectively. The average SNR is computed by taking the expectation of the SNR time series over the experiment (or a portion thereof), and is varied by adding a constant value: note that this corresponds to simulating a different transmit power than actually employed in the experiments. We consider only instantaneous channel knowledge for the moment. The figures contain both theoretical and simulated curves. In particular, theoretical performance is obtained by estimating the parameters of the correlated Nakagami-m model (in terms of the coefficient m and the correlation ρ) and then using the statistics of the model to obtain performance figures as per the analysis in Section 4.6.1. On the contrary, simulations take the SNR time series (offset by the same constant value used in the analysis to simulate different transmit power) and reproduce the behavior

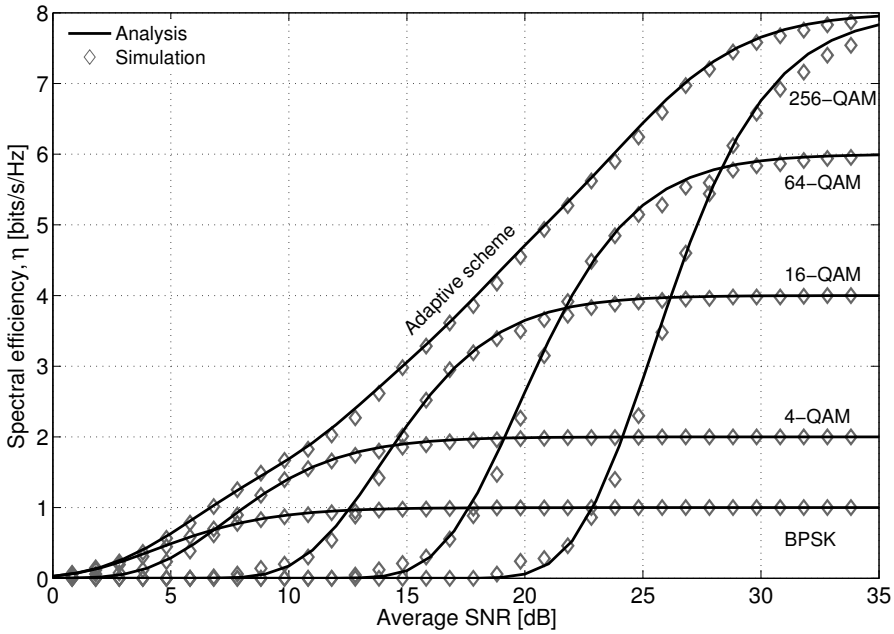

Figure 4.34. *Comparison between theoretic and simulated spectral efficiency vs. SNR over link T1–H1 in the instantaneous knowledge case.*

of the system over that time series. Analytical curves are provided in the figures as solid black lines, whereas simulation results are depicted using grey markers. In order to show that moderate time variations of the SNR statistics do not impact substantially on the results of the estimation, we have chosen a window of 100 minutes in Figure 3.12, from 2:30 to 4:10 from the beginning of the experiment. In this window, T1–H1's and T1–H2's SNRs are almost constant, whereas T1–H4's experiences more abrupt ups and downs spanning $10\,\mathrm{dB}$ (see Fig. 3.12). Nevertheless, simulations adhere quite accurately to analysis, in particular for the adaptive scheme. Non-adaptive schemes also show a very good accordance of analysis and simulations. Note that the adaptive scheme does not closely follow the envelope of the non-adaptive ones: this is expected because the SNR is not fixed, but rather follows a Nakagami-m pdf whose mean is reported in the abscissa of the graphs. In the presence of instantaneous channel knowledge, this may allow the use of modulations of larger constellation size, yielding a higher average spectral efficiency than achieved by the best non-adaptive scheme for the same average SNR.

The next metric of interest for our comparison is bit error outage (BEO), which suggests whether the adaptive scheme is successful enough at compensating for changes in the channel by adapting the modulation rate. We remark that, when affected by delayed channel

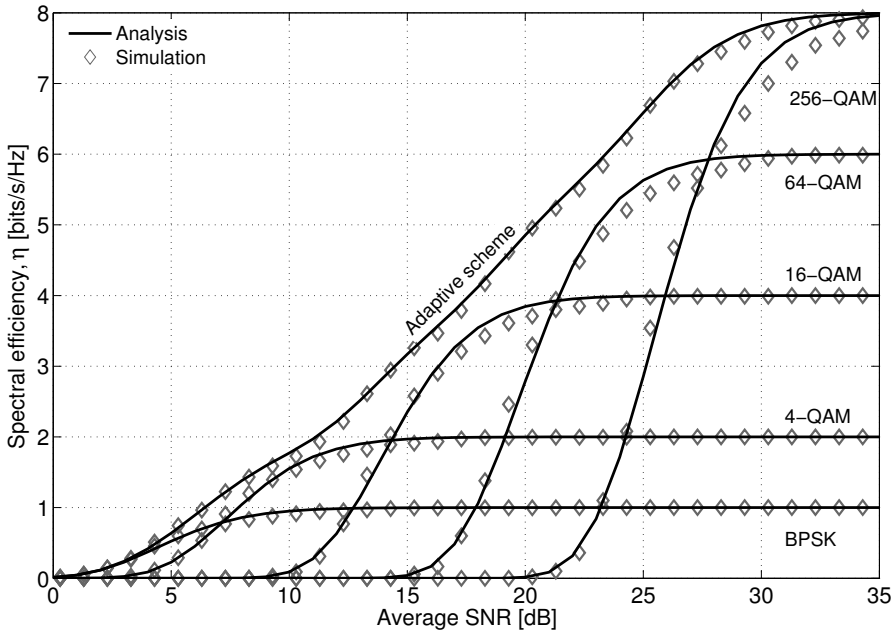

Figure 4.35. *Comparison between theoretic and simulated spectral efficiency vs. SNR over link T1–H2 in the instantaneous knowledge case.*

knowledge, adaptation is expected to be less effective, as while channel knowledge is acquired, not only the absolute value, but also the statistics of the channel fading phenomena will have changed. Figures from 4.37 to 4.39 show the BEO metric for the links from T1 to H1, H2 and H4, respectively. The different behaviors observed in Figure 3.12 for the channel SNR traces reflect in different outage probability in the figures. We provide both simulated curves and analytical predictions, for both the instantaneous and the delayed channel knowledge cases; for the latter, different delays are provided. The first result is that while the BEO of instantaneous knowledge steadily decreases for increasing SNR, delayed knowledge causes outage events to be likely even for high SNR, creating a sort of floor effect whereby the BEO does not decrease below 0.1 in all figures, until the average SNR is higher than roughly $30\,\mathrm{dB}$. In addition, we observe that more stationary SNR trace chunks (i.e., where the statistics of the SNR do not change much within the interval where the estimation of the model parameters is performed), do not show substantial difference between the model and simulation results. However, m and ρ are key to a correct prediction, which is by itself inaccurate for two reasons: short windows contain few samples and thus do not allow to correctly estimate the statistics of the signal; longer windows contain enough samples, but may incur state changes in the channel behavior, which would also deviate the estimated

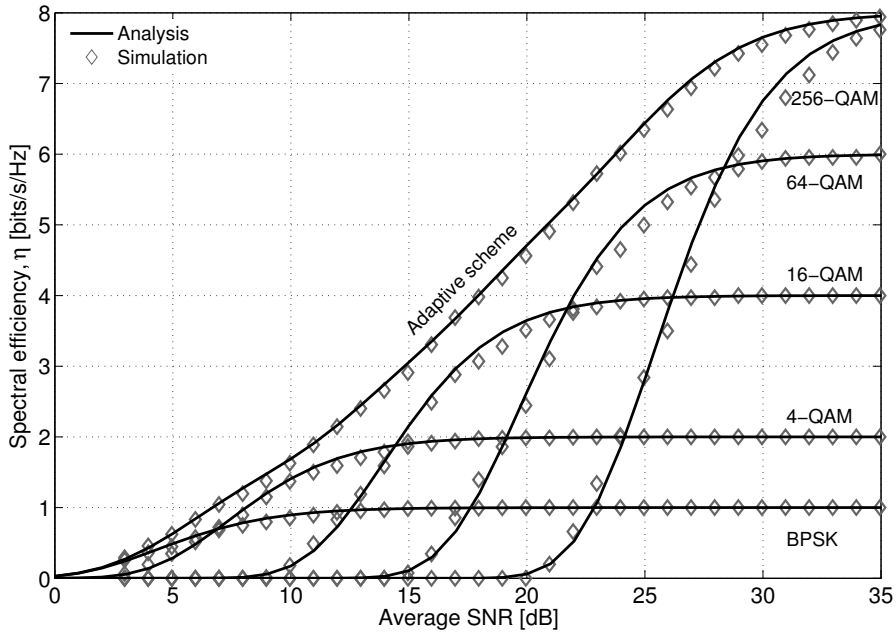

Figure 4.36. *Comparison between theoretic and simulated spectral efficiency vs. SNR over link T1–H4 in the instantaneous knowledge case.*

channel parameters. For these reasons, the predicted performance in the presence of delayed knowledge correctly estimates the level of the BEO floors, but shows some offset in the oscillations around such floors.

Figures 4.40–4.42 show the average BEO evolution over time for the T1–H1 link. In terms of hours and minutes from the beginning of the experiment, Figure 4.40 refers to the time interval from 0:00 to 1:40, Figure 4.41 to the interval from 3:20 to 5:00 and Figure 4.42 to the interval from 5:00 to 6:40. We observe that the behavior of the channel changes considerably, both in terms of the parameter m of the Nakagami model (impacting BEO oscillations when the SNR ranges from 10 to $30\,\mathrm{dB}$) and in terms of the correlation among samples when delayed channel knowledge versions are considered (impacting the level of the BEO floor before high SNR is reached, as low correlation leads to a higher chance of choosing the wrong modulation.

The last metric we evaluate is the link throughput for the adaptive modulation scheme, G, defined as the spectral efficiency multiplied by the probability of success, averaged over the probability of selecting a specific modulation. Figures 4.43, 4.44, and 4.45 detail the behavior of the throughput for links from T1 to H1, H2, and H4, respectively. The figures report both the instantaneous and the delayed channel knowledge cases. We observe that the lack

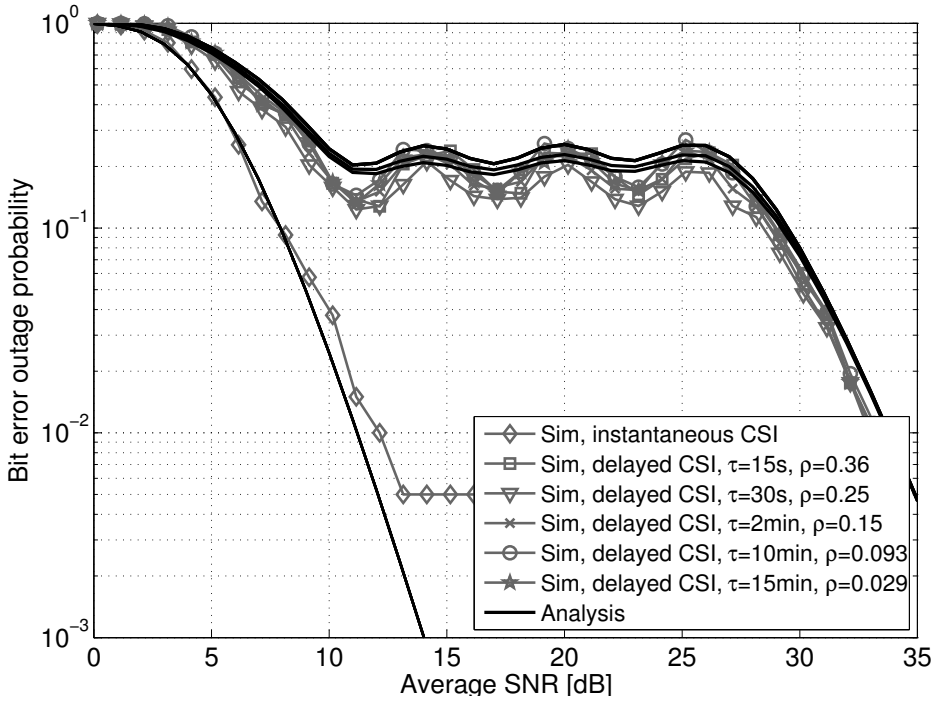

Figure 4.37. *Bit error outage probability as a function of the average SNR for link T1–H1 ,* $m = 3$.

of timely knowledge impairs the throughput performance, as a consequence of higher bit error rates (bit error outage is a more likely event). This effect is amplified by greater delays, though as expected the loss of correlation makes high delays equally inconvenient. However, this decrease is still acceptable, especially in stationary scenarios where the correlation is sufficiently high, as is the case for links T1–H1 and T1–H2. We note in fact that all figures refer to the time window in the middle of the experiment, from 4:10 to 5:50 after the beginning. In this phase, we observe a quite stationary behavior over the T1–H1 and T1–H2 links, which results in very good match between analysis and simulation. On the other hand, the T1–H4 link experiences long-term variations of larger amplitude over the considered time window (see Figure 3.12), which result in a poorer match between analytical and simulated results, especially in case of delayed channel knowledge. However, even in this case, analytical curves are still sufficient to achieve a coarse estimate of the throughput behavior.

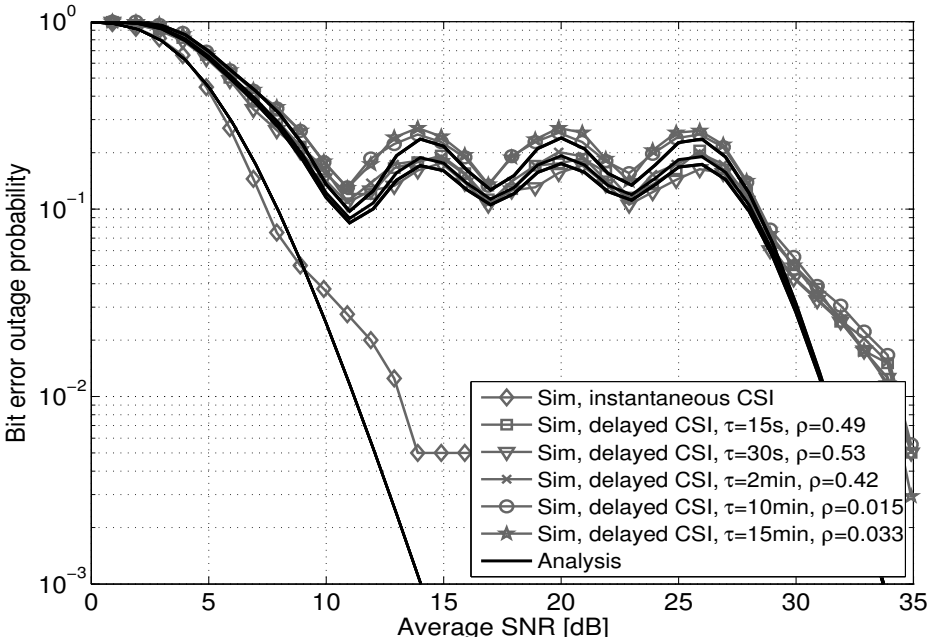

Figure 4.38. *Bit error outage probability as a function of the average SNR for link T1–H2,* $m = 5$.

Table 4.2. *Comparison of average correct packet reception probabilities*

Receiver	**IID / Data**	**MM1**	**MM2**	**HMM**
Experiment A				
H1	0.578	0.580	0.579	0.580
H2	0.569	0.568	0.567	0.568
H4	0.924	0.923	0.922	0.910
Experiment B				
H1	0.370	0.369	0.369	0.369
H2	0.690	0.692	0.691	0.695
H4	0.924	0.9231	0.922	0.910

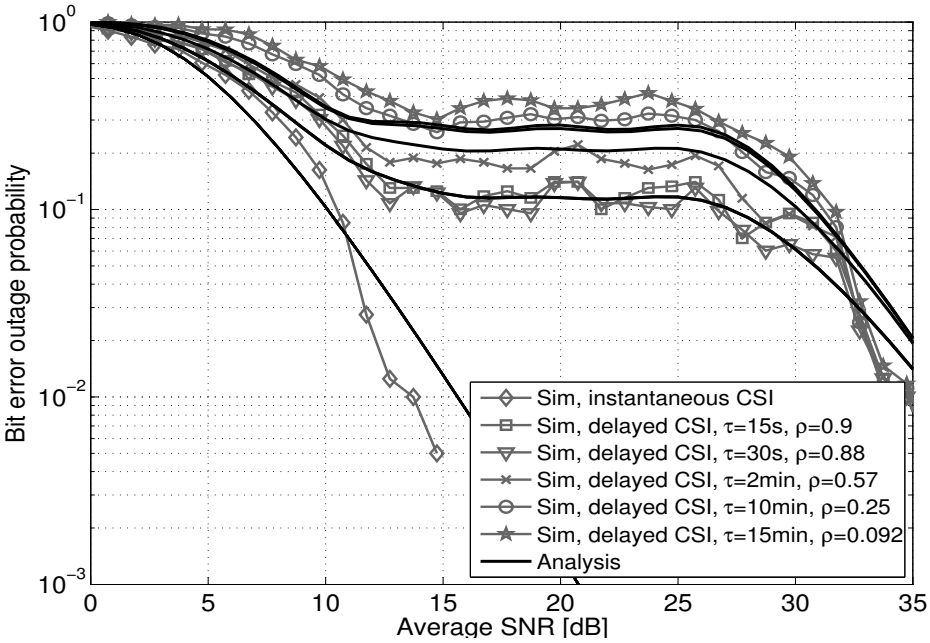

Figure 4.39. *Bit error outage probability as a function of the average SNR for link T1–H4, $m = 2$.*

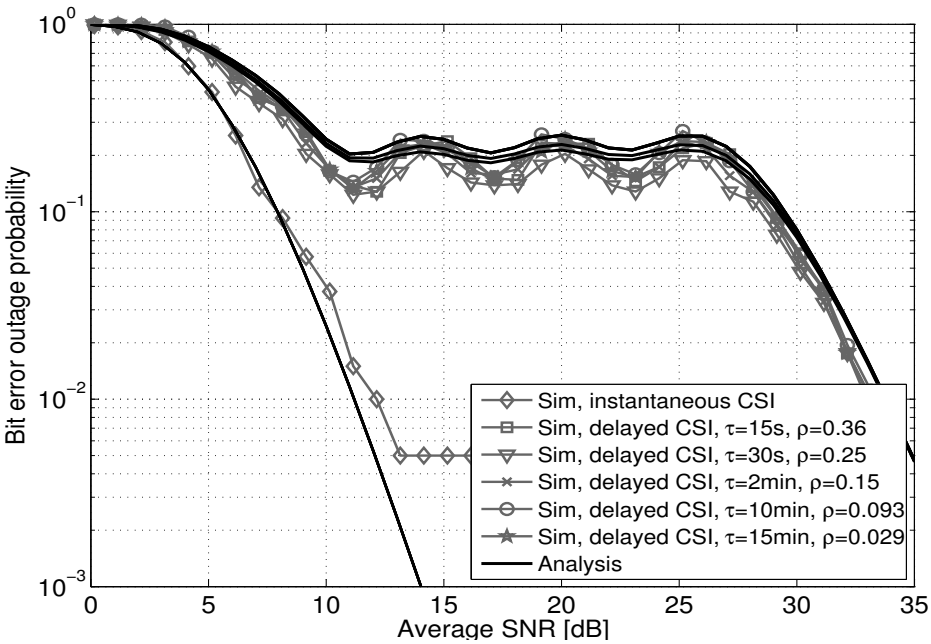

Figure 4.40. *Bit error outage probability as a function of the average SNR for link T1–H1. Analysis and simulation shown for both the instantaneous and the delayed channel knowledge case. Time window from 0:00 to 1:40. Estimated $m = 3$.*

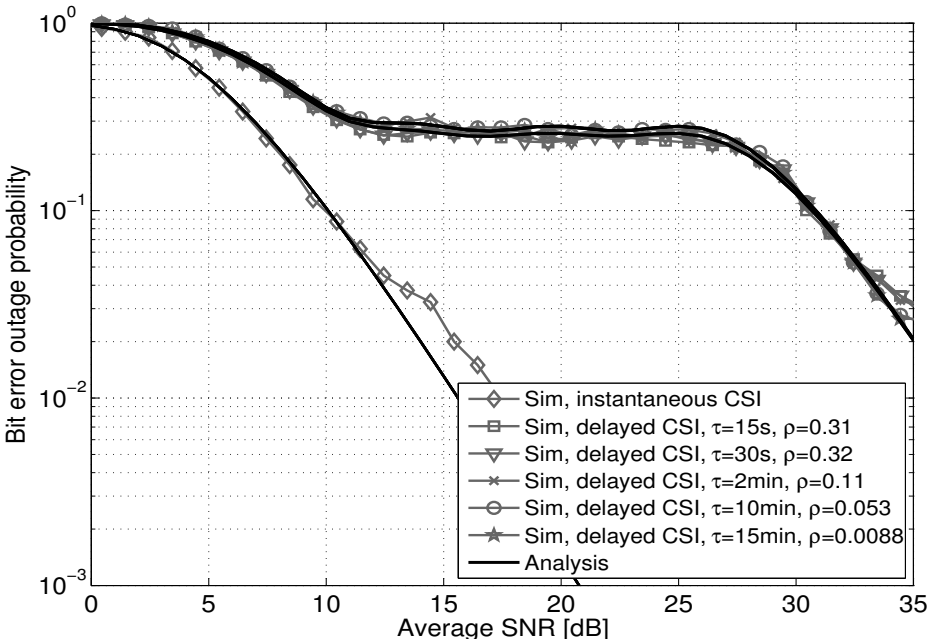

Figure 4.41. *Bit error outage probability as a function of the average SNR for link T1–H1. Analysis and simulation shown for both the instantaneous and the delayed channel knowledge case. Time window from 3:20 to 5:00. Estimated* $m = 2$.

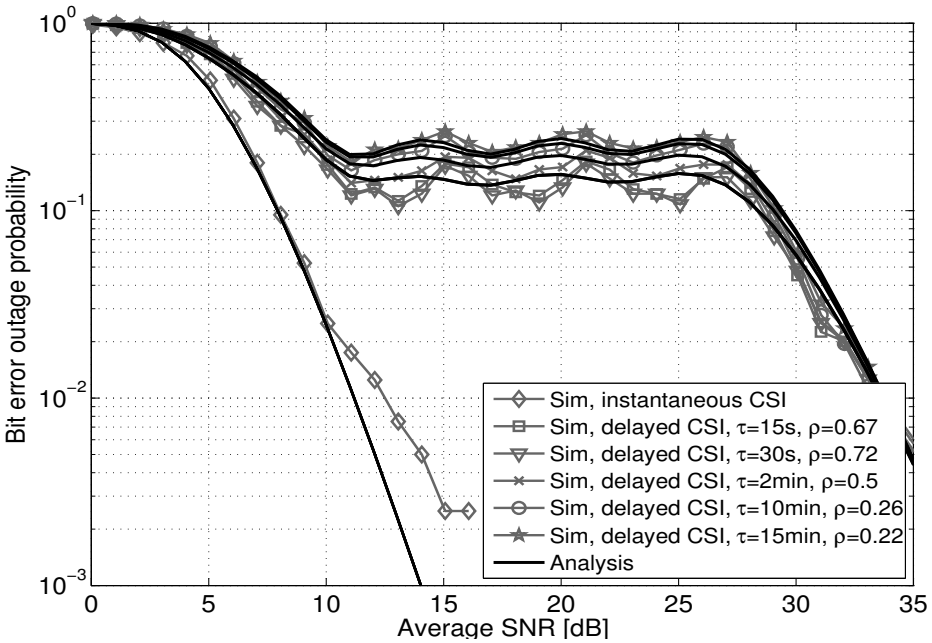

Figure 4.42. *Bit error outage probability as a function of the average SNR for link T1–H1. Analysis and simulation shown for both the instantaneous and the delayed channel knowledge case. Time window from 5:00 to 6:40. Estimated* $m = 3$.

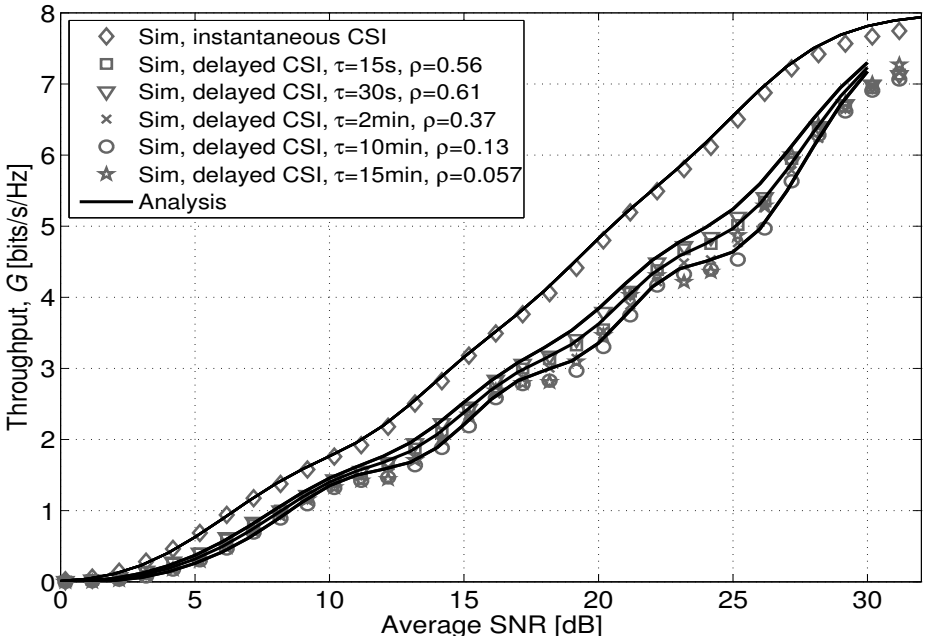

Figure 4.43. *Throughput as a function of the average SNR for both the instantaneous and the delayed channel knowledge case. For link T1–H1, estimated* $m = 3$.

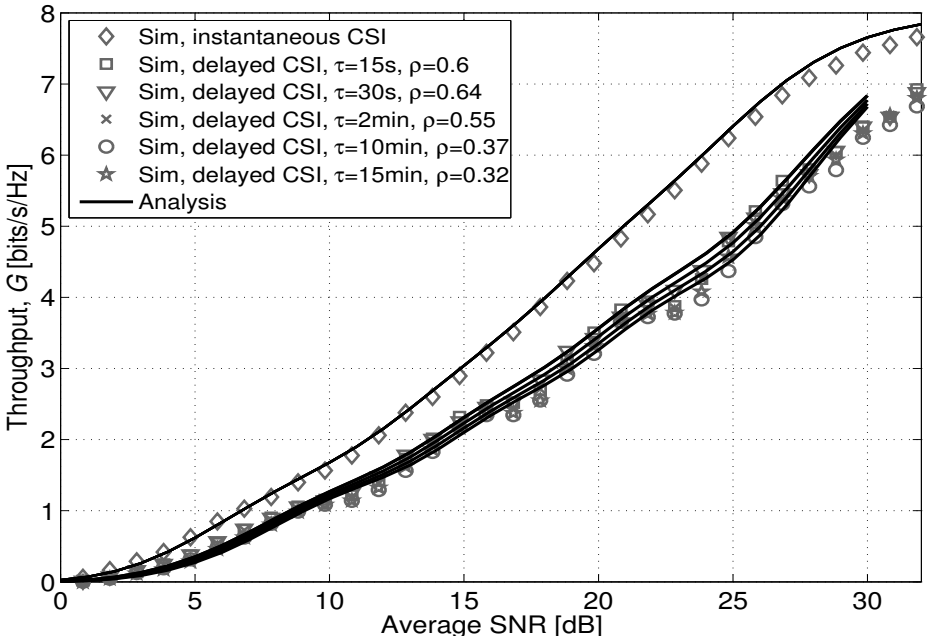

Figure 4.44. *Throughput as a function of the average SNR for both the instantaneous and the delayed channel knowledge case. For link T1–H2, estimated* $m = 2$.

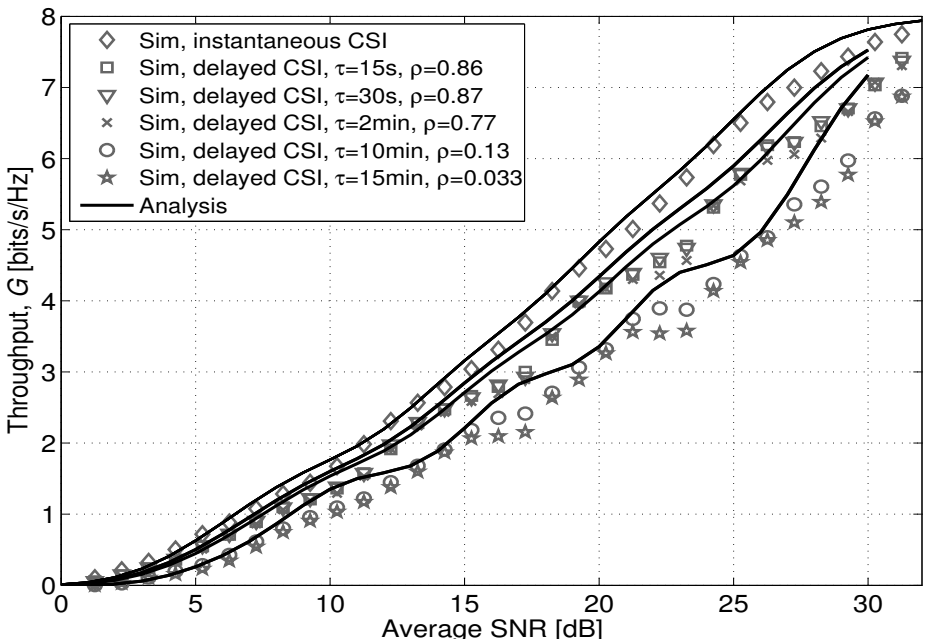

Figure 4.45. *Throughput as a function of the average SNR for both the instantaneous and the delayed channel knowledge case. For link T1–H4, estimated* $m = 2$.

Chapter 5

Predictability of the channel quality

5.1 Chapter Overview

In this chapter, we study the predictability of the underwater acoustic communications performance. In fact, the adaptive communications schemes that have been analyzed in the previous chapter require control message exchanges, which result in increased latency and energy consumption, thus leading to inefficiency. For this reason, we analyze both KAM11 and SPACE08 data sets, in order to evaluate the predictability of the communications performance over time interval of tens and hundreds of seconds and to determine whether the amount of signaling can be reduced.

5.2 Motivations and Related Work

We assess the predictability of the communication channel quality, so as to determine the classes of feedback and adaptive communications techniques that are most suitable for the underwater environment. The time scales of interest (several seconds to a few minutes) are very relevant to the performance of adaptive communications schemes and network protocols requiring control signaling.

Assessing the most appropriate techniques for providing and exploiting feedback is particularly important for the many half-duplex underwater acoustic communications systems such as those in [2] and [5]. In such systems, the use of feedback reduces the capacity of the link and increases energy consumption. Nevertheless feedback (or control messages)

is necessary to many communication techniques, such as AM, power control, Automatic Repeat reQuest (ARQ), and to networking protocols. Therefore, unlike for the wireless terrestrial counterpart, not affected by the same restrictive constraints, it is important to assess the trade-off between the benefits of adaptive techniques and the drawback of using more resources, such as energy, time and bandwidth.

In contrast to the study in [66], we focus on the predictability of the communications performance (output SNR), rather than of the channel impulse response. Measures of communications performance such as output SNR are more practical to send over an acoustic feedback channel and are more important when determining the next transmission parameters in an Adaptive Modulation and Coding (AMC) context. In addition, we focus on performance averaged over the length of transmission packets because techniques like AMC are driven by conditions that change over inter-packet intervals. In [67], the authors provide a study on the predictability of the SNR computed on the received signal, which will be called input SNR later on, for the closed loop power control technique. As we will show in the following, for single carrier wide-band modulation schemes, such as that considered in [67], closed loop power control may not be as effective as it is commonly thought. Moreover, our work differs from the work in [67], in the considered environment and in the observed metric: in fact, even if assessing the predictability of the input SNR or of the output SNR is qualitatively equivalent, quantitatively it is not. The authors of [68] performed the first study taking into account outdated CSI, but they did not study the possibility of decreasing the feedback rate. Moreover, none of the studies on underwater network protocols, such as [69], [70], [71], [72] and [73] deals with or takes advantage of time correlated channel conditions. Indeed, differently from the terrestrial radio communications, where the transmission rates and propagation delays are negligible with respect to the time-varying channel conditions in a stationary scenario, the underwater case is more heavily affected by environmental changes of the order of several seconds, so that these effects should be considered when optimizing or designing new networking protocols. This approach appears, for the first time, in [74], where the authors observe via simulation that changes in the sound speed profile conditions affect the performance of MAC and routing protocols. Nevertheless, they do not study the predictability of such varying conditions, but they rather suggest to use more control messages.

5.3 Predictability over Intervals a few Seconds Long

In this section, we show the time evolution of PSDs, estimated over intervals three minutes long, by using SPACE08 data. The main contributions here are to provide evidence of the non-stationarity of the communications performance over long time intervals as well as to give evidence of the periodical behavior of the channel quality during specific time intervals. We recall that for this study we exploit the time series of the channel energy, which however is a metric proportional to the SNR.

5.3.1 The PSD of the Channel Energy

Here, we show the PSD estimated over a time interval three minutes long, during which we have tested the stationarity. Specifically, we consider systems in the middle range S3 and S4, at which the intensity of the fluctuations over periods of a few seconds is more evident than at systems S5 and S6, where the acoustic waves are more attenuated. We represent the PSD only for positive frequencies, because the spectrum is a symmetric function, given that the energy time series is a sequence of positive real numbers. Specifically, we want to focus on the intensity of variations of the order of few seconds, therefore we will show the PSD in the range $[0, 1]$ Hz. The PSD is estimated as

$$S(m, f) = \frac{T_s}{N} \Big| \sum_{t=1}^{N} E_g(t) w(t) \exp(-i2\pi f t) \Big|^2 \tag{5.1}$$

where $w(t)$ is the Hamming window, $E_g(t)$ is the channel energy process, and m is the index of the epoch of the measurement.

Figures 5.1 and 5.2 show the pseudocolor plot of the estimated PSD: frequencies are shown in the x-axis, while Julian dates, at which data were collected, are indicated in the y-axis. We observe that the PSD for system S4 reveals a peak at 0.3 Hz, which corresponds to a three seconds period of the intensity fluctuations of the channel. This is observed at dates 292, 295 and 298. Similar considerations apply also for system S3, although the peaks are less evident.

Figure 5.3 shows the pseudocolor plot of the magnitude of the impulsive channel response during Julian date 298 at 4 AM for system S4. It can be noticed that the second arrival has almost three peaks every ten seconds, which corresponds to a peak at frequency

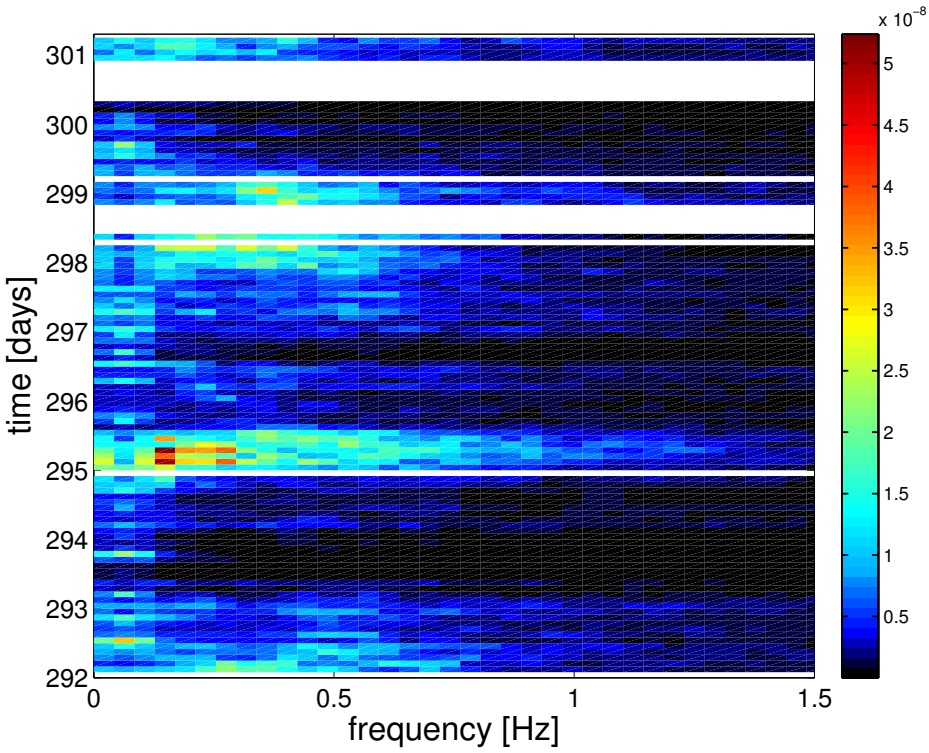

Figure 5.1. *Pseudocolor plot of the estimated PSD (linear scale) of the channel energy at system S3, from October 18 to 27. The white periods correspond to a lack of measured data.*

0.3 Hz in the PSD. This behavior can be explained by considering the environmental conditions, and in particular the wind driven wave energy in the surface wave spectra between 0.2 Hz and 0.6 Hz, which is shown in Figure 5.4.

During the periods of low wind driven waves, as those at dates 292, 295 and 298, the surface wave is coherent over a large spatial region. This results in a greater area of coherent reflection, which is modulated by the regular periodicity of the surface roughness. This area of coherent reflection gives rise to large and periodic fluctuations of the overall energy, such as those observed in Figure 5.3. On the other hand, when there are higher wind waves, such as those during dates 293, 296 and 300, the coherence of the scattering off the surface is broken, decreasing the area of coherent reflection. This causes many individually fluctuating but smaller intensity arrivals, whose overall energy fluctuations are slower and less intense. From Figures 5.1 and 5.2 we can see how variable the spectrum is over long periods of time, which shows that the problem of understanding the stationarity time scale was well-founded even for static underwater channels. This study shows the importance of the

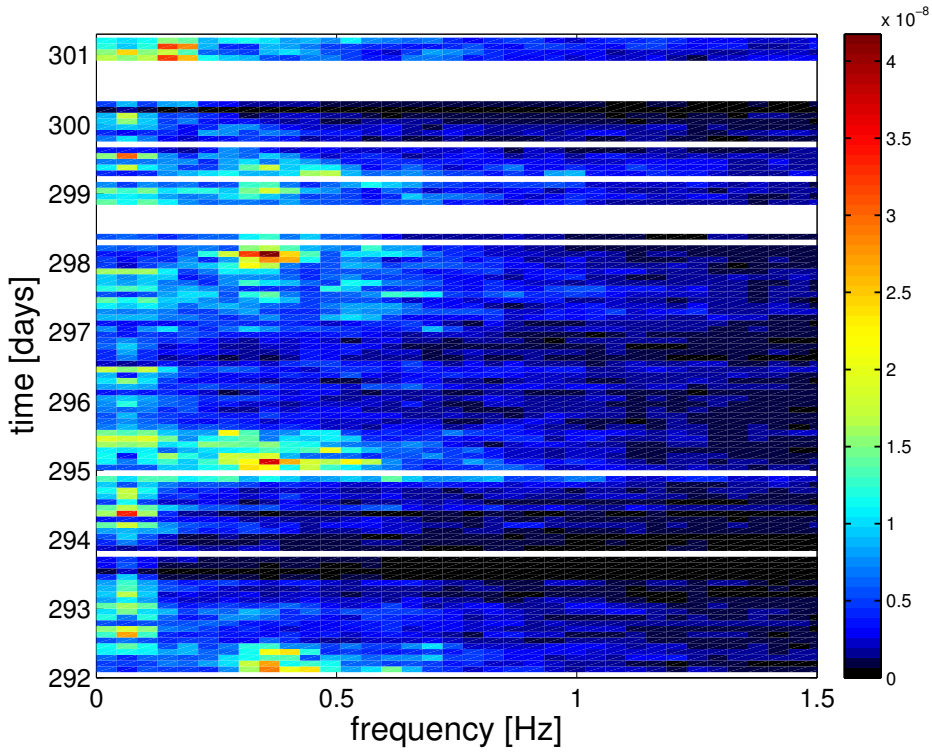

Figure 5.2. *Pseudocolor plot of the estimated PSD (linear scale) of the channel energy at system S4, from October 18 to 27. The white periods correspond to a lack of measured data.*

hypothesis evaluation, in order to both construct predictors and develop better models for shallow water propagation.

5.4 Predictability over Intervals a few Minutes Long

5.4.1 System Model

Figure 5.5 represents the considered Single Input Multiple Output (SIMO) system model. Modulation symbols, $a(n)$, are transmitted over the channel, $c(t, \tau)$, which introduces distortion, and they are received with additive noise $w(t)$ at the receiver side at different depths. At the receiver side, after synchronization, the received signals are re-sampled, combined, and processed by a DFE. Then, the output symbol SNR, γ, is estimated from the software decision at the output of the equalizer, $\tilde{s}(n)$, and is then fed back. The transmitter, based on a predefined Quality of Service (QoS) requirement, decides for the largest constellation size which assures such QoS. In our case, we consider constant modulus constellations, such as

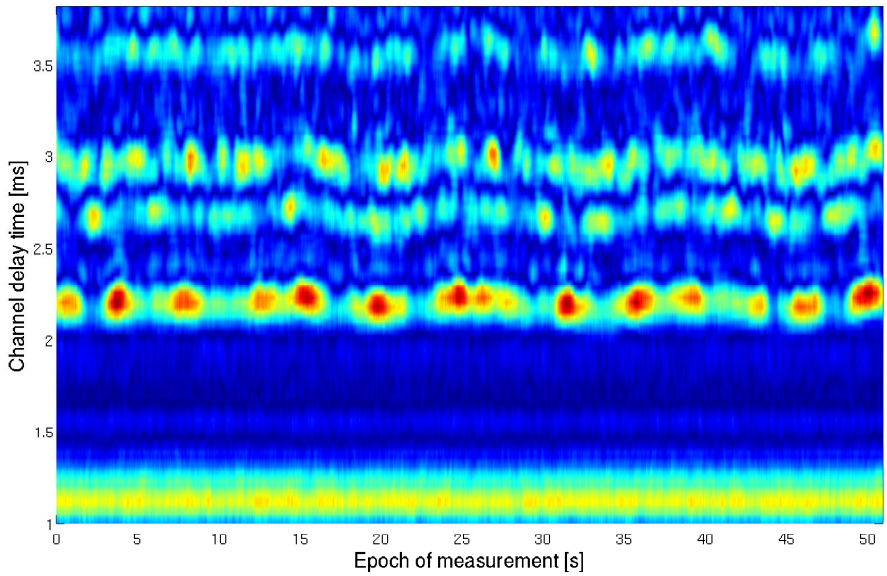

Figure 5.3. *Pseudocolor plot of the channel impulse response at S4, during Julian date* 298.

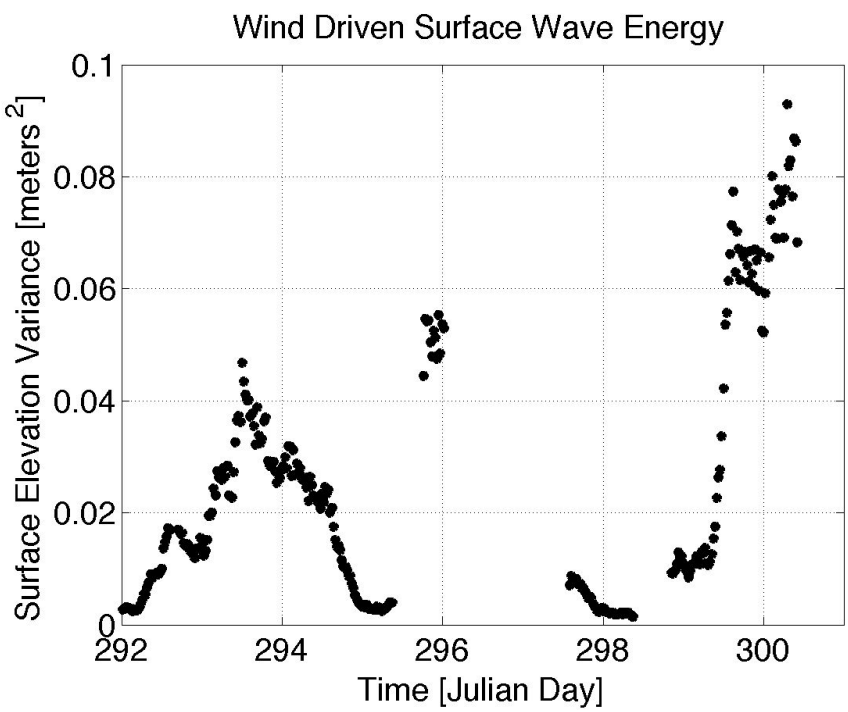

Figure 5.4. *Time series of the wind driven surface wave energy.*

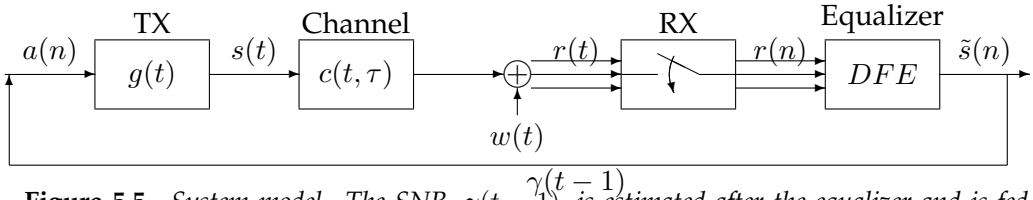

Figure 5.5. *System model. The SNR, $\gamma(t-1)$, is estimated after the equalizer and is fed back to the receiver. The symbol $r(t)$ represents the vector of the received symbols at different receiver elements.*

M-ary Phase-Shift Keying (M-PSK), with $M \in \{2, 4, 8\}$, and we choose as QoS the maximum BER, here 10^{-3}, for the transmitted bit stream. We compute the BER as a function of the average symbol SNR γ, by assuming that the received $\tilde{s}(n)$, inside a packet, is affected by only Additive White Gaussian Noise (AWGN), so that we can use the following equations [75]:

$$P_b(M;\gamma) = \begin{cases} Q\left(\sqrt{2\gamma}\right), & M = 2 \\ Q\left(\sqrt{\gamma}\right), & M = 4 \\ \frac{2}{3}Q\left(\sqrt{2\gamma}\sin\left(\pi/8\right)\right), & M = 8. \end{cases} \tag{5.2}$$

Given a maximum BER, we compute the set of threshold SNRs, which are associated to each constellation size M.

We express the software decision as

$$\tilde{s}(n) = \tilde{c}(0)a(n) + \tilde{w}(n), \tag{5.3}$$

where $\tilde{c}(0)$ is the residual channel coefficient after equalization and $\tilde{w}$ is the residual additive noise, which includes noise and residual ISI. We assume that $\tilde{c}(0)$ is constant over a packet but varies slowly across different packets.

From Equation (5.3) we define the average output SNR as

$$\gamma = \frac{|\tilde{c}(0)|^2 E_s}{\sigma^2}, \tag{5.4}$$

where E_s is the energy of the modulation symbol and σ^2 is the variance of the residual noise $\tilde{w}$. Given that we consider constant modulus constellations, E_s is one for every symbol. We estimate the residual channel coefficient for each packet as the average of the software decision divided by the corresponding transmitted signal, so that it does not depend on the specific transmitted symbol. Then, we can write the residual coefficient as:

$$\tilde{c}(0) = \mathbb{E}\Big[\frac{\tilde{s}(n)}{a(n)}\Big]. \tag{5.5}$$

Given that w is a zero-mean process, this estimator is unbiased. Finally, we estimate σ^2 as:

$$\sigma^2 = \mathbb{E}[|\tilde{s}(n) - \tilde{c}(0)a(n)|^2]. \tag{5.6}$$

We can interpret $\tilde{c}(0)$ as the average residual channel coefficient over a packet, and σ^2 as the corresponding mean square error.

In the adaptive modulation context, we are interested in evaluating the changes of channel conditions over consecutive packets, in order to assess whether or not the fed back information is sufficient, if not outdated, to get the expected performance improvement. Specifically, we focus on the fluctuations of the output SNR in Equation (5.4), which is proportional to the squared amplitude of the average residual channel coefficient and is a measure of the received signal quality seen by the upper layers in the protocol stack. Given that we are observing an average output SNR, and given that the transmitter and receiver are stationary, we do not expect rapid fluctuations, but given that both the feedback delay and the processing time at the receiver are of the order of seconds, we do expect changes in the channel state over this time scale.

We characterize the amplitude of the residual channel coefficient as a Nakagami random variable fully described by its second order statistics. Therefore, the probability density function for the output SNR,γ, is given by Eq. (4.22). We choose this model because, thanks to the parameter m, it makes it possible to consider different fading shapes (from Rayleigh to Rice), and given that the distribution is completely defined by its second order statistics, it can be easily estimated from the time series. We then assume that two consecutive SNR samples, separated by a time interval τ, γ and γ_τ, are Nakagami correlated random variables, described by the following conditioned probability density function:

$$\begin{aligned} f\left(\gamma_\tau|\gamma\right) = & \frac{m}{(1-\rho\left(\tau\right))\overline{\gamma}}\left(\frac{\gamma_\tau}{\rho\left(\tau\right)\gamma}\right)^{(m-1)/2} \\ & \times I_{m-1}\left(\frac{2m\sqrt{\rho\left(\tau\right)\gamma\gamma_\tau}}{(1-\rho\left(\tau\right))\overline{\gamma}}\right)\exp\left(\frac{m(\rho\left(\tau\right)\gamma+\gamma_\tau)}{(1-\rho\left(\tau\right))\overline{\gamma}}\right), \end{aligned} \tag{5.7}$$

where $\rho\left(\tau\right)$ is the correlation coefficient between γ_τ and γ, and $I_{m-1}\left(\cdot\right)$ is the modified Bessel function of the first kind and of order $m-1$.

5.4.2 Communications Performance: Outage Probability and Throughput

Here, we present a derivation of the communications performance for the AM system. In particular, we focus on outage probability and average throughput as functions of feedback delay. The outage probability is a measure of how likely the event of not satisfying the QoS is, when using the constellation size associated to the fed back SNR value, γ. The average throughput is the mean amount of information per unit of time that is correctly received, and represents the tradeoff between high spectral efficiency and unreliable transmission.

We compute the outage probability, given a fed back γ, as the probability that γ_τ is less than the SNR threshold $T(\gamma)$, i.e., the inferior extreme of the SNR region associated to γ, which in symbol is

$$P(\gamma_\tau|\gamma) = \int_0^{T(\gamma)} f(\gamma_\tau|\gamma) d\gamma_\tau \,. \tag{5.8}$$

This conditional probability can be averaged over all the possible values for γ, including the case in which γ is less than the minimum average symbol SNR assuring the QoS, which will be indicated as T_1. This outage probability is

$$P(\tau) = \int_{T_1}^{+\infty} f(\gamma) \int_0^{T(\gamma)} f(\gamma_\tau|\gamma) d\gamma_\tau d\gamma \; + \int_0^{T(1)} f(\gamma) d\gamma \,. \tag{5.9}$$

We compute the throughput as the average amount of information per second per Hertz, that is transmitted based on the fed back SNR γ and is correctly received. Given γ, the transmitter chooses the constellation size $M(\gamma)$, for which the number of bits per symbol is $b(\gamma) = \log_2(M(\gamma))$. By assuming the usage of an interleaver over the bit stream, we can compute the average throughput, given γ, as

$$\Theta(\tau|\gamma) = \int_{T(\gamma)}^{\infty} b(\gamma)(1 - BER(\gamma_\tau)) f(\gamma_\tau|\gamma) d\gamma_\tau \,, \tag{5.10}$$

which, by considering all possible values for γ, becomes:

$$\Theta(\tau) = \int_{T_1}^{+\infty} f(\gamma) b(\gamma) \int_{T(\gamma)}^{\infty} (1 - BER(\gamma_\tau)) f(\gamma_\tau|\gamma) d\gamma_\tau d\gamma \,. \tag{5.11}$$

It is worth noticing that when γ_τ is less than the inferior extreme of the region associated to γ, i.e., if $\gamma_\tau < T(\gamma)$, the throughput is zero, because the QoS is not met.

5.4.3 Predictability of the communications performance

A process is said to be predictable in time, when it is possible to know its value some time τ ahead. The process that we want to be able to predict is the average AM system

performance in terms of throughput and outage probability. The analytical model, proposed in Section 4.6.1, depends only on the second order statistics of two correlated Nakagami variables, i.e., we only need to study the correlation coefficient between γ and γ_τ. Moreover, linear predictors are based on the second order statistics of the process that they track, so that from this study we can also conclude whether or not they can be a valuable class of predictors, and if so over which time scales. In the following we assume that the output SNR is a stationary random process, so that we can estimate the correlation coefficient. The stationarity of the SNR process was verified in [16], for the non-coherent case.

We indicate the correlation coefficient between two consecutive SNRs, γ and γ_τ, separated in time by τ, as $\rho(\tau)$ and compute it as:

$$\rho(\tau) = \frac{Cov(\gamma, \gamma_\tau)}{\sqrt{Cov(\gamma)C(\gamma_\tau)}}, \tag{5.12}$$

where $Cov(\cdot)$ is the covariance function defined as $Cov(x, y) = \mathbb{E}[(x - m_x)(y - m_y)]$ and, if the function has only one variable, it is equivalent to computing the variance of the variable. Figure 5.6 shows the correlation coefficient $\rho(\tau)$ as a function of time within the six minute observation interval. Here we present $\rho(\tau)$ at three different hours: 2 am and 4 am on Julian date 187 and 00 am on 188. Given that for each minute we have the data for 31 packets, and given that each packet lasts 1 s, we interpolate the data in order to fill the gaps on the time series. For this reason we can observe a step-like behavior in Figure 5.6 between each minute and the next one. It is worth noticing that the shapes of the correlation functions at hours 2 and 4 am are quite alike, i.e., there is a second local maximum on the correlation function around the fourth minute, and then it decreases. This observation suggests that there are slowly changing environmental conditions which determine the shape of such correlation functions. The third curve, referring to date 188, is measured almost one day after the other two curves, and we can see how the shape of the correlation function has changed. In fact for this curve we note two other local maxima around the third minute and the fifth minute. The cause of such behavior has not been studied yet, but as a next step we will analyze the environmental data and propagation models, trying to explain these trends.

We now evaluate the average AM communications system performance, by applying Equations (5.10) and (5.11) and using the correlation coefficients $\rho(\tau)$ evaluated from the data. In particular, we estimate the parameter m for the Nakagami probability distribution, as $m = \frac{\overline{\gamma}^2}{\mathbb{E}[(\gamma-\overline{\gamma})^2]}$, whereas we do not compute the average SNR $\overline{\gamma}$ from the data, but we

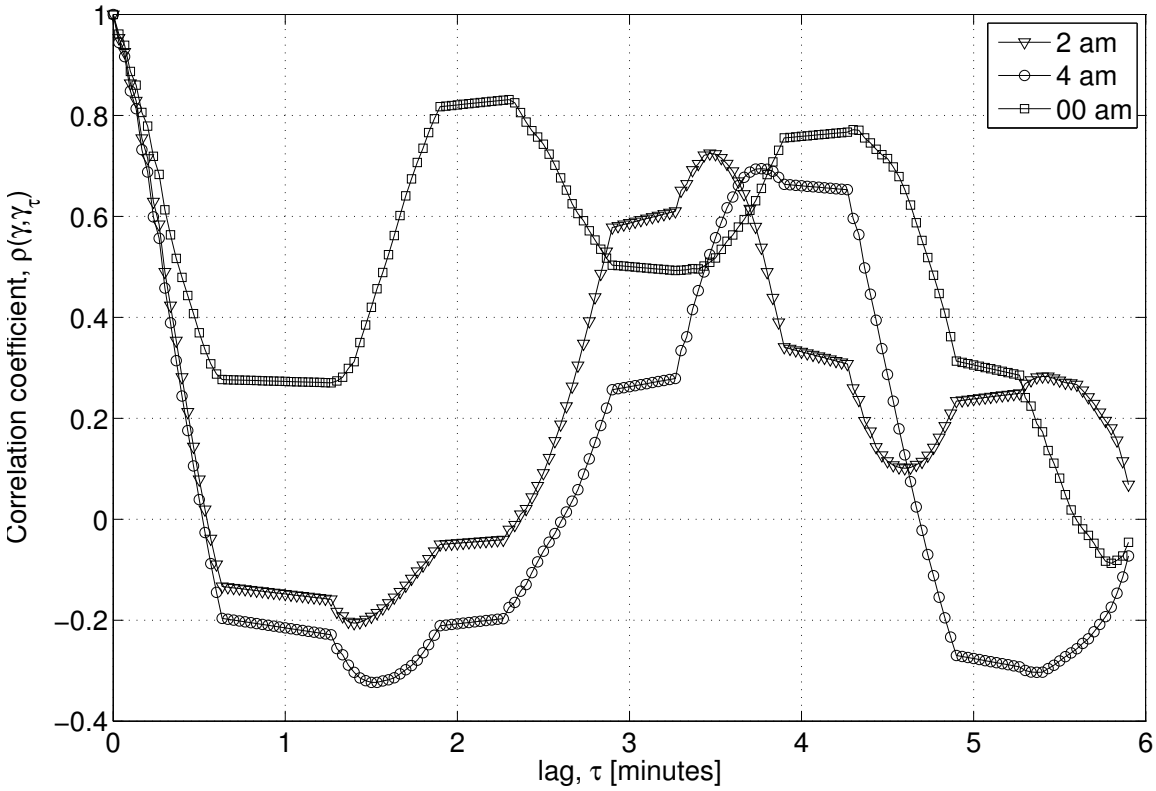

Figure 5.6. *Correlation coefficient between two consecutive SNRs, τ minutes apart in time.*

assume the same one (10 dB) for all the considered hours, in order to get comparable results, and in order to highlight the effects on the performance of the time fluctuations.

Figures 5.7 and 5.8 show the system performance as functions of the feedback delay τ. Doubtless, a feedback delay of the order of minutes is not of great practical interest, but we aim at understanding over which time interval the process can be predictable, in order to prove that the feedback rate can be decreased. As expected, corresponding to the local maxima of the correlation function, we find local minima for the outage probability and local maxima for the throughput. This means that if we knew the system performance at the present time, we could expect similar performance in four minutes as shown by the curve representing hour 2 am, and in three and five minutes as shown by the curve representing time 00 am. We prove here that the time behavior of an adaptive system performance permits predictability, and we show how far ahead this holds.

These results give rise to several considerations on how to take advantage of such predictability when designing communications and networking algorithms. For what concerns

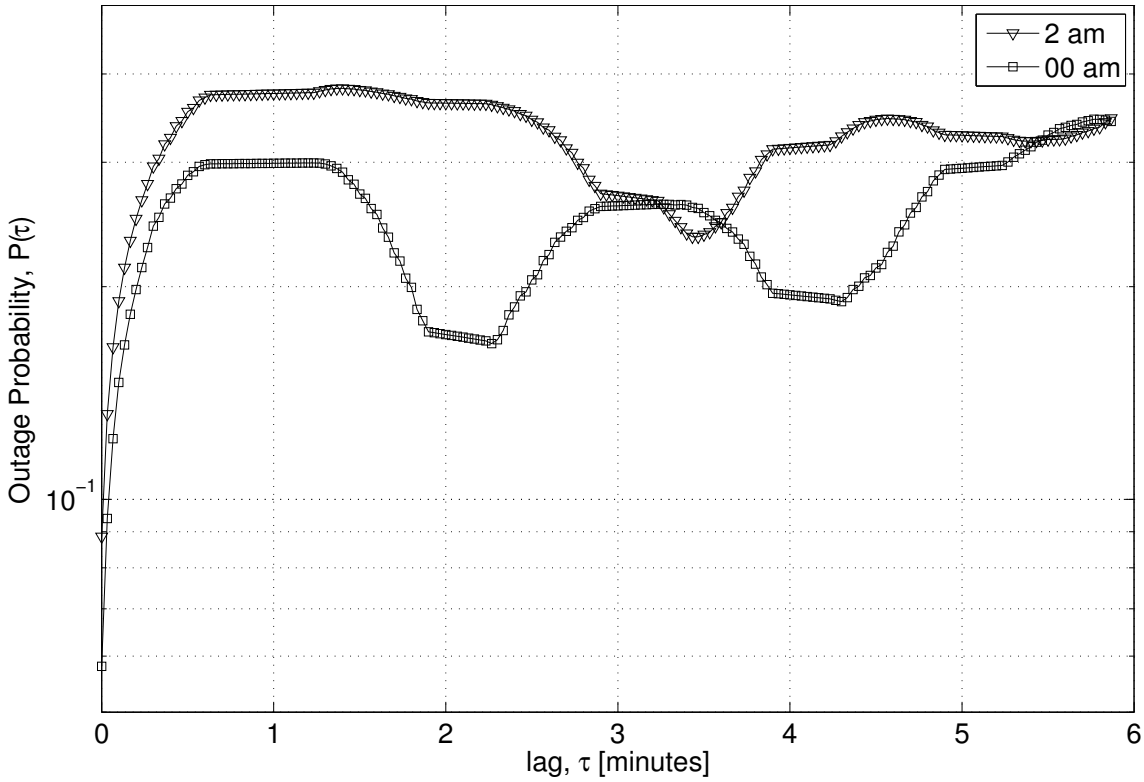

Figure 5.7. *Outage probability as a function of τ.*

adaptive modulation schemes, we should be able to answer the following open questions: which feedback information about the channel state is most effective in enhancing the performance? Is the feedback rate adjustable without any performance loss? Which predictors are more suitable to indicate the next transmission parameters? For example, so far we assumed that the previous average output SNR γ provides sufficient information to choose the best next transmission parameters, but if we want to decrease the feedback rate, this may no longer be the case. Indeed, as shown in Figures 5.7 and 5.8, the information about the next time when a local maximum occurs in the correlation coefficient can be more useful to adjust accordingly the system parameters and it would not require the same amount of feedback, thus saving energy and channel occupancy.

Moreover, we can also say that knowing the time between two highly correlated instants can be very useful for networking protocols. For example, a routing protocol could take advantage of such information by updating the routing tables accordingly or a medium access control protocol could assign the best slot of time to different nodes according to

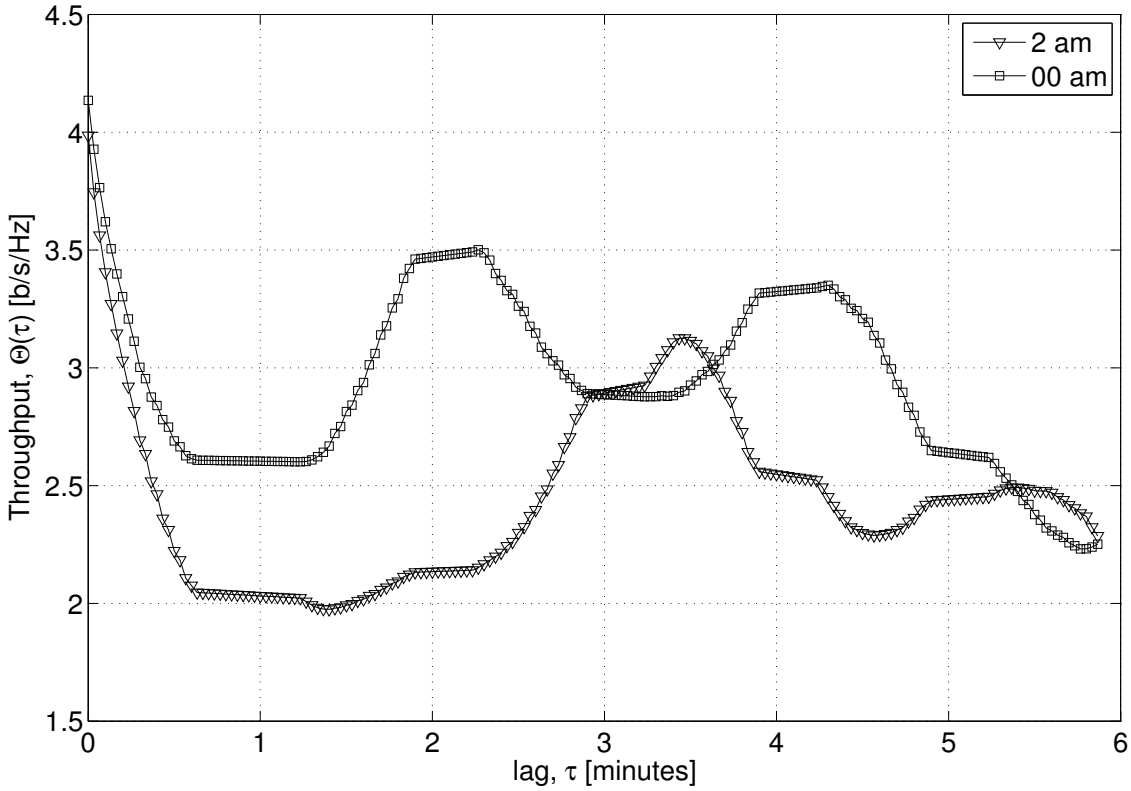

Figure 5.8. *Throughput as a function of τ.*

different local fluctuations that they observe.

Chapter 6

Conclusions

In this thesis, we first presented an extensive analysis of channel properties in terms of both time spread and time correlation coefficients, over three different data sets, collected in shallow water scenarios during different times and at different locations. In this study, we also qualitatively evaluated the effects of environmental conditions on the observed channel properties.

Second, we studied the stationarity and evaluated the interval of stationarity of the energy of the underwater acoustic channel, for the SPACE08 data set. More specifically, we observed that, on average, different links are characterized by intervals of stationarity of the order of a few minutes. We provided a qualitative explanation of the results by considering the relationship between the environmental fluctuations and the stationarity of the acoustic channel.

Then, we evaluated the suitability of Markov models to represent the channel in a shallow water scenario. We considered Markov models with memory of both one and two past events, as well as a HMM, and compared them to data traces and to a simpler IID error model. Our comparison showed that the HMM is better at tracking long term channel behavior, especially if substantial shifts between low quality and high quality channel states are observed; in addition, an HMM yields a much better representation of long-term error correlation, while providing a very good approximation of the distribution of the length of error bursts. For this study, we focused on the SubNet09 dataset, since it contained long experimental runs, thus making it possible to assess the model accuracy in channels experiencing limited non-stationarity due to changing environmental conditions.

Moreover, we proposed and validated a model for HARQ performance based on Markov chains. The study was based on the processing of SNR traces extracted from transmissions performed during SubNet09. Starting from these traces, we extracted channel statistics and used them to derive reliable SNR regions for good code ensembles. We then estimated a Markov model that tracks the evolution of the channel state in time, and finally employed the model to estimate the performance of incremental redundancy (Type II) HARQ, as compared to Type I HARQ. The model was shown to significantly simplify channel representation, yet to satisfactorily adhere to the actual channel behavior, thereby allowing to characterize the performance of HARQ policies with low complexity, even in the presence of variations of moderate entity in the channel statistics with respect to those used to train the model.

Furthermore, we evaluated the effectiveness of AM techniques. Specifically, we validated a correlated Nakagami-m fading model to track the evolution of SNR traces in underwater acoustic channels. This model was found to correctly represent the channel behavior, provided that periods of adequate length are chosen to train the model. We considered adaptive variable-rate modulation schemes for underwater acoustic networks, and applied the channel model to estimate the performance of such schemes in the presence of both instantaneous and delayed information about the channel model. Results showed that whenever the parameter estimation is accurate enough (i.e., when performed over a time window where the fading process is approximately stationary), the model could reproduce the performance of the adaptive modulation scheme as simulated on the channel traces in terms of average spectral efficiency, bit error outage probability and throughput. On the contrary, when the channel experienced fast variations within a given time window, the estimation of such metrics may be less accurate, yet the general behavior of the channel could still be captured, as was the case for bit error outage, whose average value in the delayed channel knowledge case was correctly estimated, although the model may fail to capture minor oscillations around this value.

Finally, we studied the predictability of the communications performance for an underwater acoustic scenario, based on KAM11 and on SPACE08. Both data sets provided evidence that under specific environmental conditions, the communications performance could be predicted over different time intervals. These results paved the way to new stud-

ies and techniques that could further improve underwater acoustic communications and networks.

6.1 Future Directions

Even though a lot of effort has been put on this research, there are still many problems to be solved, in order to further develop effective underwater acoustic communications and networks. Open problems, such as how this technology could robustly support mobility, and how network protocols can take advantage or deal with the time and space varying performance, need to be addressed. In our opinion, all these problems can be tackled from different perspectives, e.g., simulation, measurements and analysis: all are equally important to contribute to achieving the purpose.

The community should try hard to identify some basic shared assumptions that have to be taken into account for each layer of the protocol stack in a communication system. In fact, the development of underwater communications and networks could leverage more on the expertise acquired in the terrestrial wireless counterpart, if the general assumptions made for terrestrial wireless communications were validated, as we did in this thesis. On the other hand, we need to investigate better which conditions are no longer verified and which new problems should be addressed, such as for example the feedback problem that we pointed out in Chapter 5.

In order to do so, data availability plays a key role in the development of this technology. Even though many experimental campaigns have been carried out in the last decades, the collected acoustic and environmental data are not always easy to access. Moreover the post-processing needed to make these signals usable is sometimes time consuming. Therefore, the community should aim at making the data available and usable.

Future experimental campaigns should also collect communication performance statistics, besides acoustic signals, from as many transmitter-receiver links as possible, so as to improve the awareness of the dynamics that network protocols have to deal with, both in time and space.

List of Publications

The work presented in this thesis has in part appeared in the articles reported below.

Journal papers

[J1] **B. Tomasi**, P. Casari, L. Badia, M. Zorzi, "A Study of Incremental Redundancy Hybrid ARQ over Markov Models for Underwater Acoustic Communications", submitted to *IEEE Transactions on Wireless Communications*.

Conference papers

[C1] **B. Tomasi**, J. C. Presig, M. Zorzi, "On the Predictability of Underwater Acoustic Communications Performance: the KAM11 Data Set as a Case Study", in *Proc. of ACM WUWNet* Seattle, Washington, Dec. 2011.

[C2] **B. Tomasi**, L. Toni, P. Casari, J. C. Presig, M. Zorzi, "A Study on the SPIHT Image Coding Technique for Underwater Acoustic Communications", in *Proc. of ACM WUWNet* Seattle, Washington, Dec. 2011.

[C3] N. Michelusi, **B. Tomasi**, U. Mitra, J. Preisig, M. Zorzi, "An Evaluation of the Hybrid Sparse-Diffuse Algorithm for Underwater Acoustic Channel Estimation", in *Proc. of MTS/IEE OCEANS* Kona, Hawaii, Sept. 2011.

[C4] P. Casari, **B. Tomasi**, K. Pelekanakis, M. Chitre, M. Zorzi, "Performance Evaluation of SNR Prediction Schemes in Acoustic Communication Systems using Variable-Rate Modulation", in *Proc. of Underwater Acoustic Measurement (UAM)* Kos, Greece, Jun. 2011.

[C5] **B. Tomasi**, J. Presig, M. Zorzi, "A Study on the Wide-Sense Stationarity of the Underwater Acoustic Channel for Coherent Communication Systems", in *Proc. of Underwater Acoustic Measurement (UAM)* Kos, Greece, Jun. 2011.

[C6] **B. Tomasi**, J. Presig, G. B. Deane, M. Zorzi, "A Study on the Wide-Sense Stationarity of the Underwater Acoustic Channel for Non-coherent Communication Systems", in *Proc. of IEEE European Wireless Communication* Vienna, Austria, Apr. 2011.

[C7] **B. Tomasi**, P. Casari, L. Badia, M. Zorzi, "A Study of Incremental Redundancy Hybrid ARQ over Markov Channel Models Derived from Experimental Data", in *Proc. of ACM WUWNet* Woods Hole, Massachusetts, Oct. 2010.

[C8] **B. Tomasi**, L. Toni, P. Casari, L. Rossi, M. Zorzi, "Performance Study of Variable-Rate Modulation for Underwater Communications based on Experimental Data", in *Proc. of MTS/IEE OCEANS* Seattle, Washington, Sept. 2010

[C9] **B. Tomasi**, P. Casari, L. Finesso, G. Zappa, K. McCoy, M. Zorzi, "Underwater Acoustic Channel Modeling using Markov and Hidden Markov Models", in *Proc. of IEEE MILCOM* San Jose, California, Oct. 2010.

[C10] K. McCoy, **B. Tomasi**, G. Zappa, "JANUS: the genesis, propagation and use of an underwater standard", in *Proc. of ECUA*, Istanbul, Turkey, Jul. 2010.

[C11] **B. Tomasi**, G. Zappa, K. McCoy, P. Casari, M. Zorzi, "Experimental Study of the Acoustic Channel Time-Correlation for Underwater Communications", in *Proc. of IEEE Oceans* Sydney, Australia, May 2010.

Bibliography

[1] N. Michelusi, U. Mitra, A. Molisch, and M. Zorzi, "UWB Sparse/Diffuse Channels, Part I: Channel Models and Bayesian Estimators," 2011, submitted to IEEE Transactions on Signal Processing.

[2] "Teledyne benthos undersea systems and equipment," www.benthos.com.

[3] Woods Hole Oceanographic Institution, "Ocean Toolbox." [Online]. Available: ftp://acoustics.whoi.edu/pub/Matlab/oceans/

[4] K. McCoy, "JANUS: from primitive signal to orthodox networks," in *Proc. of IACM UAM*, Nafplion, Greece, Jun. 2009.

[5] L. Freitag, M. Grund, S. Singh, J. Partan, P. Koski, and K. Ball, "The WHOI Micro-Modem: An Acoustic Communications and Navigation System for Multiple Platforms," http://www.whoi.edu, 2005.

[6] P. L. Nielsen and M. Siderius and F. B. Jensen, "Acoustic time-variability measurements in the Straits of Sicily," in *Proc. of the European Conf. on Underwater Acoustics*, Lyon, France, Jul. 2000.

[7] T. C. Yang, "Measurements of temporal coherence of sound transmissions thorugh shallow water," *Journal of the Acoustic Society of America*, vol. 120, no. 5, pp. 2595–2614, Nov. 2006.

[8] ——, "Temporal coherence of sound transmissions in deep water revisited," *Journal of the Acoustic Society of America*, vol. 124, no. 1, pp. 113–127, Jul. 2008.

[9] A. G. Zajic, "Statistical space-time-frequency characterization of MIMO shallow water acoustic channels," in *Proc. of IEEE OCEANS*, Biloxi, Oct. 2009.

[10] B. Tomasi, G. Zappa, K. McCoy, P. Casari, and M. Zorzi, "Experimental study of the space-time properties of acoustic channels for underwater communications," in *Proc. IEEE/OES Oceans*, Sydney, Australia, May 2010.

[11] P. Qarabaqi and M. Stojanovic, "Statistical modeling of a shallow water acoustic communication channel," in *Proc. of IACM UAM*, Nafplion, Greece, Jun. 2009.

[12] J. Zhang, J. Cross, and Y. Zheng, "Statistical channel modeling of wireless shallow water acoustic communications from experiment data," in *Military Communications Conference (MILCOM)*, Nov. 2010.

[13] T. J. Willink, "Wide-sense stationarity of mobile MIMO radio channels," *IEEE Transactions on Vehicular Technology*, vol. 57, no. 2, pp. 704–714, Mar. 2008.

[14] D. Umansky and M. Patzold, "Stationarity test for wireless communication channels," in *Proc. of IEEE GLOBECOM*, Dec. 2009, pp. 1–6.

[15] O. Renaudin, V.-M. Kolmonen, P. Vainikainen, and C. Oestges, "About the multipath stationarity of car-to-car channels in the 5 GHz band," in *Proc. of URSI International Symposium on Electromagnetic Theory (EMTS)*, Aug. 2010, pp. 872 –875.

[16] B. Tomasi, J. Presig, G. Deane, and M. Zorzi, "A Study on the Wide-Sense Stationarity of the Underwater Acoustic Channel for Non-coherent Communication Systems," in *European Wireless Conference*, Apr. 2011.

[17] N. Michelusi, U. Mitra, and M. Zorzi, "Hybrid Sparse/Diffuse UWB Channel Estimation," in *2011 IEEE 12th International Workshop on Signal Processing Advances in Wireless Communications (SPAWC 2011)*, San Francisco, USA, June 2011.

[18] C. Berger, S. Zhou, J. Preisig, and P. Willett, "Sparse channel estimation for multicarrier underwater acoustic communication: From subspace methods to compressed sensing," *IEEE Transactions on Signal Processing*, vol. 58, no. 3, pp. 1708–1721, Mar. 2010.

[19] C. Carbonelli, S. Vedantam, and U. Mitra, "Sparse channel estimation with zero tap detection," *IEEE Transactions on Wireless Communications*, vol. 6, no. 5, pp. 1743–1763, May 2007.

[20] A. S. Gupta and J. Preisig, "An adaptive sparse sensing approach to shallow water acoustic channel estimation and tracking," *The Journal of the Acoustical Society of America*, vol. 128, no. 4, pp. 2354–2354, 2010.

[21] C. Pelekanakis and M. Chitre, "Comparison of sparse adaptive filters for underwater acoustic channel equalization/estimation," in *International Conference on Communication Systems (ICCS)*, Nov. 2010, pp. 395–399.

[22] N. Michelusi, B. Tomasi, U. Mitra, J. Preisig, and Z. M., "An evaluation of the hybrid sparse-diffuse algorithm for underwater acoustic channel estimation," in *MTS/IEEE OCEANS, Kona, Hawaii*, 2011.

[23] L. Berkhovskikh and Y. Lysanov, *Fundamentals of Ocean Acoustics*. Springer, 1982.

[24] M. Stojanovic and J. Preisig, "Underwater acoustic communication channels: Propagation models and statistical characterization," *IEEE Communications Magazine*, vol. 47, no. 1, pp. 84–89, Jan. 2009.

[25] K. Tu, D. Fertonani, T. Duman, M. Stojanovic, J. Proakis, and P. Hursky, "Mitigation of intercarrier interference for ofdm over time-varying underwater acoustic channels," *IEEE Journal of Oceanic Engineering*, vol. 36, no. 2, pp. 156 –171, Apr. 2011.

[26] M. Stojanovic, "On the relationship between capacity and distance in an underwater acoustic communication channel," in *Proceedings of the 1st ACM international workshop on Underwater networks*, ser. WUWNet '06, 2006, pp. 41–47.

[27] M. Porter *et al.*, "Bellhop code." [Online]. Available: http://oalib.hlsresearch.com/Rays/index.html

[28] F. Guerra, P. Casari, and M. Zorzi, "World ocean simulation system (woss): a simulation tool for underwater networks with realistic propagation modeling," in *Proceedings of the Fourth ACM International Workshop on UnderWater Networks*, ser. WUWNet '09, 2009.

[29] N. Baldo, M. Miozzo, F. Guerra, M. Rossi, and M. Zorzi, "Miracle: The Multi-Interface Cross-Layer Extension of ns2," *EURASIP Journal on Wireless Communications and Networking*, 2010.

[30] P. Casari and M. Rossi and M. Zorzi, "Towards Optimal Broadcasting Policies for HARQ based on Fountain Codes in Underwater Networks," in *Proc. IEEE/IFIP WONS*, Garmisch-Partenkirchen, Germany, Jan. 2008.

[31] A. Radosevic and J. G. Proakis and M. Stojanovic, "Statistical Characterization and Capacity of Shallow Water Acoustic Channels," in *Proc. of IEEE OCEANS*, Bremen, May 2009.

[32] P. Borgnat, P. Flandrin, P. Honeine, C. Richard, and J. Xiao, "Testing stationarity with surrogates: A time-frequency approach," *IEEE Transactions on Signal Processing*, vol. 58, no. 7, pp. 3459 –3470, Jul. 2010.

[33] M. Basseville, "Distance measures for signal processing and pattern recognition," *IEEE Transactions on Signal Processing*, vol. 18, pp. 349–369, Dec. 1989.

[34] P. Borgnat and P. Flandrin and P. Honeine and C. Richard and J. Xiao, http://perso.ens-lyon.fr/pierre.borgnat/codes.html#Stationarity_Tests.

[35] N. Michelusi, U. Mitra, A. Molisch, and M. Zorzi, "UWB Sparse/Diffuse Channels, Part II: Estimator Analysis and Practical Channels," 2011, submitted to IEEE Transactions on Signal Processing.

[36] E. L. Lehmann and G. Casella, *Theory of Point Estimation*, 2nd ed. Springer, Aug. 1998.

[37] A. P. Dempster, N. M. Laird, and D. B. Rubin, "Maximum likelihood from incomplete data via the EM algorithm," *Journal of the Royal Statistical Society, B*, vol. 39, 1977.

[38] L. Badia, M. Levorato, and M. Zorzi, "Markov analysis of selective repeat type ii hybrid arq using block codes," *IEEE Transactions on Communications,*, vol. 56, no. 9, pp. 1434 – 1441, 2008.

[39] Q. Zhang and S. Kassam, "Finite-state markov model for rayleigh fading channels," *IEEE Transactions on Communications,*, vol. 47, no. 11, pp. 1688 –1692, 1999.

[40] M. Rossi, L. Badia, and M. Zorzi, "Sr arq delay statistics on n-state markov channels with non-instantaneous feedback," *IEEE Transactions on Wireless Communications,*, vol. 5, no. 6, pp. 1526 –1536, 2006.

[41] Q. Zhang and S. Kassam, "Hybrid arq with selective combining for fading channels," *IEEE Journal on Selected Areas in Communications,*, vol. 17, no. 5, pp. 867 –880, May 1999.

[42] J.-B. Seo, Y.-S. Choi, S.-Q. Lee, N.-H. Park, and H.-W. Lee, "Performance analysis of a type-ii hybrid-arq in a tdma system with correlated arrival over a non-stationary channel," in *2nd International Symposium on Wireless Communication Systems, 2005.*, 2005, pp. 59 –63.

[43] A. J. Goldsmith and S.-G. Chua, "Variable-rate variable-power MQAM for fading channel," *Wirel. Pers. Commun.*, vol. 45, no. 10, pp. 1218–1230, Oct. 1997.

[44] S. Zhou and G. B. Giannakis, "How accurate channel prediction needs to be for transmit-beamforming with adaptive modulation over Rayleigh MIMO channels?" *IEEE Trans. on Wireless Commun.*, vol. 3, no. 4, pp. 1285–1294, Jul. 2004.

[45] T. Keller and L. Hanzo, "Adaptive modulation techniques for duplex OFDM transmission," *IEEE Trans. on Veh. Technol.*, vol. 49, no. 5, pp. 1893–1906, Sep. 2000.

[46] N. Baldo, F. Maguolo, S. Merlin, A. Zanella, M. Zorzi, D. Melpignano, and D. Siorpaes, "APOS: Adaptive Parameters Optimization Scheme for voice over IEEE 802.11g," in *Proc. of IEEE ICC*, Beijing, China, May 2008, pp. 2466–2472.

[47] J. A. Rice, V. K. McDonald, M. D. Green, and D. Porta, "Adaptive modulation for undersea acoustic telemetry," *Sea Technology*, vol. 40, no. 5, pp. 29–36, May 1999.

[48] S. Mani, T. M. Duman, and P. Hursky, "Wireline quality underwater wireless communication using high speed acoustic modems," in *Proc. of Acoustics'08*, Paris, France, Jun. 2008, pp. 4255–4260.

[49] K. V. Mackenzie, "Nine-term equation for the sound speed in the oceans," *J. Acoust. Soc. Am.*, vol. 70, no. 3, pp. 807–812, 1981.

[50] F. Pignieri, F. De Rango, F. Veltri, S. Marano, "Markovian approach to model underwater acoustic channel: techniques comparison," in *Proc. of IEEE MILCOM*, San Diego, Nov. 2008.

[51] W. Turin and R. van Nobelen, "Hidden Markov Modeling of Flat Fading Channels," *IEEE J. Select. Areas Commun.*, vol. 16, no. 9, pp. 1809–1817, Dec. 1998.

[52] L. R. Rabiner, "A tutorial on hidden Markov models and selected applications in speech recognition," in *Proc. of the IEEE*, 1989, pp. 257–286.

[53] E. N. Gilbert, "Capacity of a Burst-noise Channel," *Bell Systems Tech. Journal*, vol. 39, pp. 1253–1266, Sep. 1960.

[54] E. O. Elliot, "Estimates of Error Rates for Codes on Burst-error channels," *Bell Systems Tech. Journal*, vol. 42, pp. 1977–1997, Sep. 1963.

[55] S. Lin and D. J. Costello, *Error Control Coding: Fundamentals and Applications*. Prentice-Hall, 1983.

[56] P. S. R. Liu and E. Soljanin, "Reliable channel regions for good binary codes transmitted over parallel channels," *IEEE Trans. Inf. Theory*, vol. 52, pp. 1405–1424, Apr. 2006.

[57] L. Badia, M. Levorato, and M. Zorzi, "A channel representation method for the study of hybrid retransmission-based error control," *IEEE Trans. Comm.*, vol. 57, pp. 1959–1971, Jul. 2009.

[58] N. V. E. Soijanin and P. Whiting, "Punctured vs. rateless codes for hybrid ARQ," in *Proc. of IEEE Information Theory Workshop*, 2006, pp. 155–159.

[59] European Telecommunications Standards Institute, "Digital Video Broadcasting standards." [Online]. Available: http://www.etsi.org/website/technologies/dvb.aspx

[60] W. Webb and R. Steele, "Variable rate QAM for mobile radio," *IEEE Trans. Commun.*, vol. 43, no. 7, pp. 2223–2230, Jul. 1995.

[61] K. Cho and D. Yoon, "On the general BER expression of one- and two-dimensional amplitude modulations," *IEEE Trans. Commun.*, vol. 50, no. 7, pp. 1074–1080, Jul. 2002.

[62] M. K. Simon and M.-S. Alouini, *Digital Communication over Fading Channels: A Unified Approach to Performance Analysis*, 1st ed. New York, NY, 10158: John Wiley & Sons, Inc., 2000.

[63] M.-S. Alouini and A. J. Goldsmith, "Adaptive modulation over Nakagami fading channels," *Wirel. Pers. Commun.*, vol. 13, no. 1-2, pp. 119–143, May 2000.

[64] I. Gradshteyn and I. M. Ryzhik, *Table of Integrals, Series and Products*. Academic Press, 1980.

[65] J. Wallace, H. Ozcelik, M. Herdin, E. Bonek, and M. Jensen, "Power and complex envelope correlation for modeling measured indoor MIMO channels: a beamforming evaluation," in *Proc. of IEEE VTC-Fall*, vol. 1, Orlando, FL, Oct. 2003, pp. 363–367.

[66] A. Radosevic, T. Duman, J. Proakis, and M. Stojanovic, "Channel prediction for adaptive modulation in underwater acoustic communications," in *IEEE OCEANS, 2011 - Spain*, 2011, pp. 1 –5.

[67] P. Qarabaqi and M. Stojanovic, "Adaptive power control for underwater acoustic communications," in *IEEE OCEANS, 2011 - Spain*, 2011, pp. 1 –7.

[68] B. Tomasi, L. Toni, P. Casari, L. Rossi, and M. Zorzi, "Performance study of variable-rate modulation for underwater communications based on experimental data," in *OCEANS 2010*, sept. 2010, pp. 1 –8.

[69] M. Molins and M. Stojanovic, "Slotted FAMA: a MAC Protocol for underwater acoustic networks," in *Proc. MTS/IEEE Oceans*, Singapore, Sep. 2006.

[70] A. Syed, W. Ye, and J. Heidemann, "Comparison and Evaluation of the T-Lohi MAC for Underwater Acoustic Sensor Networks," *IEEE J. Select. Areas Commun.*, vol. 26, pp. 1731–1743, Dec. 2008.

[71] B. Peleato and M. Stojanovic, "Distance aware collision avoidance protocol for ad-hoc underwater acoustic sensor networks," *IEEE Communications Letters*, vol. 11, no. 12, pp. 1025 –1027, 2007.

[72] K. Kredo, P. Djukic, and P. Mohapatra, "Stump: Exploiting position diversity in the staggered tdma underwater mac protocol," in *IEEE INFOCOM 2009*, 2009, pp. 2961 –2965.

[73] K. Kredo and P. Mohapatra, "Distributed scheduling and routing in underwater wireless networks," in *Global Telecommunications Conference (GLOBECOM 2010), 2010 IEEE*, dec. 2010, pp. 1 –6.

[74] S. Azad, P. Casari, C. Petrioli, R. Petroccia, and M. Zorzi, "On the impact of the environment on mac and routing in shallow water scenarios," in *IEEE OCEANS, Spain*, 2011, pp. 1 –8.

[75] A. Goldsmith, *Wireless Communications*. Cambridge University Press, 2005.

Ringraziamenti

Ringrazio tutti coloro con cui ho avuto la fortuna e il piacere di collaborare durante questi tre anni, tra cui: Prof. Michele Zorzi, Prof. James Preisig, Dr. Paolo Casari, Dr. Laura Toni, Giovanni Zappa, Dr. Kim McCoy e Prof. Leonardo Badia. Senza la lora collaborazione, questa tesi non sarebbe stata possibile. Tra questi, vorrei esprimere particolare riconoscenza a Prof. Michele Zorzi, fonte di ispirazione, supervisore attento e capace di insegnarmi a lavorare autonomamente, e a Prof. James Preisig per il suo tempo prezioso e i suoi insegnamenti e consigli. Inoltre sono grata a Dr. Paolo Casari, punto di riferimento e collega instancabile e a Dr.ssa Laura Toni per l'entusiasmo riposto in ogni lavoro. Infine, esprimo un particolare ringraziamento a tutte le persone, che in qualsiasi modo hanno fatto parte del mio quotidiano, rivelandosi insostituibile fonte di sostegno e autentica amizia.

I would like to thank anyone, with whom I had the pleasure and fortune to work during the last three years, among these: Prof. Michele Zorzi, Prof. James Preisig, Dr. Paolo Casari, Dr. Laura Toni, Giovanni Zappa, Dr. Kim McCoy, Prof. Leonardo Badia, Prof. Urbashi Mitra, Prof. Lorenzo Finesso and Nicoló Michelusi. Without their collaboration, this thesis would have not been possible. In particular, among these people I want to show my gratitude to Prof. Michele Zorzi, for being a source of inspiration, careful supervisor, able to teach me the importance of autonomy, and to Prof. James Preisig for his precious time, advice and lessons. Moreover, I thank Dr. Paolo Casari, point of reference and untiring colleague and Dr. Laura Toni for her enthusiasm in our activity. Finally, I am particularly grateful to anyone, who has been part of my daily life, thus becoming irreplaceable source of moral support and authentic friendship.